

Evaluation of Finite Element Analysis on topology optimized direct metal laser sintered Ti6Al4V structures

JA van Rooyen

 **Orcid.org/0000-0001-5364-5628**

Dissertation accepted in fulfilment of the requirements for the degree *Master of Engineering in Mechanical Engineering* at the North-West University

Supervisor: Mr. C.P. Kloppers

Co-Supervisor: Dr. J.J. Janse van Rensburg

Graduation: May 2020

Student number: 24138614

ACKNOWLEDGEMENTS

I would like to thank to following people for their continuous support and encouragements:

- My wife Juandri van Rooyen
- My parents Salmon and Tharia van Rooyen
- My mother and father in-law Corne and Willie Prinsloo

I would like to thank Nic Minnaar from Altair for his technical support on the topology optimization process in solidThinking Inspire™.

I would like to thank Cobus Aucamp and Jan Wiid from Xnovestafrica for the opportunities they gave me as well as the support provided.

I would like to thank my supervisor Mr. CP Kloppers and Dr. Jan Janse van Rensburg for giving me this opportunity to do my masters and being there in the difficult times. I would like to thank CPAM for the funds to be able to complete my masters.

John1: 3-5

³All things were made through him, and without him was not anything made that was made. ⁴In him was life, and the life was the light of men. ⁵The light shines in the darkness, and the darkness has not overcome it.”

Abstract

The problem under investigation in this dissertation is the validity of Finite Element Analysis (FEA) when applied to topology optimized Direct Metal Laser Sintering (DMLS) structures manufactured from Ti6Al4V with the assumption that the weakest material properties are homogeneous. In order to address the problem under investigation a verifiable topology optimized test specimen is generated.

DMLS is an additive or layered manufacturing process used to melt metal powder with a high powered laser to produce customised components. Finite element strength analysis is the practical application of FEM (Finite Element Modelling) and entails the virtual modelling of products and systems for the purpose of finding and solving potential structural issues. Topology optimization is a type of structural optimization that uses a mathematical method to optimize a defined problem within a design domain with fixed boundary conditions, and the optimization is done for appropriate objective conditions that satisfy the defined constraints.

The mechanical properties of DMLS Ti6Al4V are investigated, and the weakest material properties are identified. These material properties are assigned to the design space identified, and the topology optimized model is generated in solidThinking Inspire™. The topology optimized model is validated by comparing the stress induced by the complex loads on the initial model and topology optimized model as well as weight reduction of the topology optimized model.

An FEA is performed on the validated topology optimized model. This FEA strives to mimic the conditions of the practical test performed on the topology optimized model. The FEA is performed in more than one software package in order to compare the simulations for verification.

Two practical tests were performed on the topology optimized model. The von Mises stress for different loads is determined from the virtual strain rosette and obtained from the FEA. These simulated von Mises stress and practically obtained von Mises stresses are compared in an attempt to validate the simulation. An excellent linear correlation between the practical results and simulated results were found, with the practically obtained results being consistently lower than the simulated results. The reason given for this phenomenon is the use of the weakest material properties as though they are homogeneous. A verifiable conclusion is drawn, and the problem under investigation is addressed.

Keywords: Topology Optimization, Direct Metal Laser Sintering, Ti6Al4V, Finite Element Analysis, Finite Element Modelling, Digital Image Correlation, solidThinking Inspire™.

Contents

ACKNOWLEDGEMENTS	II
ABSTRACT	III
LIST OF TABLES	IX
LIST OF FIGURES.....	XI
LIST OF ABBREVIATIONS.....	XVII
CHAPTER 1	1
1. Introduction	1
1.1 Background	1
1.2 Problem statement	2
1.3 Research objectives	2
1.4 Research methodology.....	2
1.4.1 Literature overview	3
1.4.2 Model development	3
1.4.3 Finite Element Analysis	3
1.4.4 Validating Topology Optimized model.....	3
1.4.5 Obtain experimental results	4
1.4.6 Validating finite element analysis.....	4
1.5 Dissertation layout.....	4

CHAPTER 2	6
2 Literature overview.....	6
2.1 Introduction.....	6
2.2 Additive Manufacturing	6
2.3 Direct metal laser sintering (DMLS)	8
2.3.1 Laser process.....	10
2.3.1.1 Single-track formation.....	12
2.3.1.2 Single-layer formation.....	13
2.3.2 Mechanical properties of DMLS Ti6Al4V.....	15
2.3.2.1 Microstructure.....	15
2.3.2.2 Geometry.....	24
2.3.2.3 Surface finish.....	25
2.3.2.4 Build orientation.....	25
2.3.2.5 Residual stresses	27
2.3.2.6 Porosity	29
2.3.2.7 Summary of mechanical properties out of the literature	29
2.3.3 Mechanical testing.....	34
2.3.3.1 Standard metal tensile test	34
2.4 Topology Optimization	36
2.4.1 Topology Optimization software.....	42
2.5 Finite element analysis	42
2.5.1 FEA and metal AM	43
2.5.2 Validation of FEA.....	44

2.6	Conclusion.....	44
CHAPTER 3		46
3	Theory	46
3.1	Introduction.....	46
3.2	Tensile test	46
3.3	Basic principles of FEM	50
3.4	Von Mises stress	53
3.5	Strain rosette	54
3.6	Conclusion.....	54
CHAPTER 4		56
4	Model development	56
4.1	Introduction.....	56
4.2	Mechanical properties of DMLS Ti6Al4V.....	56
4.3	Design space.....	64
4.4	Loads	65
4.4.1	Axial load.....	65
4.4.2	Bending load	69
4.4.3	Torsional load.....	72
4.4.4	Concluding the loads	73
4.5	Geometry optimization.....	74
4.6	Conclusion.....	77

CHAPTER 5 78

5 FEM investigation..... 78

5.1 Introduction..... 78

5.2 FEM setup..... 78

5.3 FEA of practical test conditions..... 79

5.4 Verifying finite element analysis..... 80

5.5 Selecting the virtual strain rosette positions 82

5.6 Validating the Topology optimized model..... 83

5.7 Conclusion..... 84

CHAPTER 6 86

6 Experimental procedure..... 86

6.1 Introduction..... 86

6.2 Topology optimized model preparations. 86

6.3 DIC system setup 87

6.4 Practical testing 88

6.5 Applying virtual strain gauges 89

6.6 Conclusion..... 89

CHAPTER 7 90

7 Compare simulated and experimental results..... 90

7.1 Introduction..... 90

7.2 Simulated results 90

7.3 Experimental results 91

7.4	Results discussion.....	92
7.5	Conclusion.....	95
CHAPTER 8		96
8	Conclusion and recommendations	96
8.1	Introduction.....	96
8.2	Conclusions.....	96
8.3	Recommendations.....	97
8.4	Closure	97
CHAPTER 9		98
APPENDIX A		109
APPENDIX B		112
APPENDIX C		115
APPENDIX D		116
APPENDIX E		117

List of Tables

Table 1: Tensile properties of SLM 304 stainless steel samples with varying hatch angles [30]	14
Table 2: Properties of fully lamellar Ti-6Al-4V obtained with altered processing conditions [36–38].....	17
Table 3: Properties of Ti-6Al-4V with bimodal microstructure [46, 47].....	20
Table 4: Tensile properties of DMLS samples indicating the effect of surface finish [67]	25
Table 5: Tensile properties of as-built SLM bars [68].....	26
Table 6: A summary of the literature regarding the mechanical properties of DMLS Ti6Al4V	30
Table 7: Brief conclusions of various authors	32
Table 8: Chemical composition of Ti6Al4V powder (in weight %)	56
Table 9: MTS Landmark 370.10 specifications [137]	58
Table 10: Average UTS, 0.2% offset yield and modulus of elasticity for each orientation	63
Table 11: Material properties of DMLS Ti6Al4V	64
Table 12: Resultant stress for each chosen position.....	91
Table 13: Resultant strain from practical test 1	91
Table 14: Resultant strain from practical test 2.....	91
Table 15: Resultant von Mises stress obtained from virtual strain rosette.....	92
Table 16: Comparison of the resultant von Mises stresses for position 1 as obtained from the two practical test	117
Table 17: Comparison of the resultant von Mises stresses for position 2 as obtained from the two practical test	117
Table 18: Comparison of von Mises stress as obtained from FEA and practical test 1 at position 1	117

Table 19: Comparison of von Mises stress as obtained from FEA and practical test 1 at position 2	118
Table 20: Comparison of von Mises stress as obtained from FEA and practical test 2 at position 1	118
Table 21: Comparison of von Mises stress as obtained from FEA and practical test 2 at position 2	118

List of Figures

Figure 1: Research methodology.....	3
Figure 2: Seven types of AM processes [12]	6
Figure 3: Classification of metal AM processes [4]	6
Figure 4: DMLS process [17].....	8
Figure 5: Parameters influencing DMLS [19]	9
Figure 6: Schematic representation of electrons emitting photons [20].....	10
Figure 7: Schematic representations of continuous laser process [20]	10
Figure 8: Schematic representations of a fibre laser [21].....	11
Figure 9: Optical absorption depths for several materials over a range of wavelengths [23]	12
Figure 10: Single tracks at the substrate [25].....	13
Figure 11: Surfaces of the first layer from SS-grade 904L powder obtained at different hatch distances [27].	14
Figure 12: Rotations in scan strategy in neighbouring planes [29].....	14
Figure 13: Equiaxed microstructure of a titanium alloy showing globular α grains (light).....	16
Figure 14: Light micrographs showing a typical lamellar microstructure [34].....	16
Figure 15: Optical micrograph showing examples of fully lamellar microstructures derived from	16
Figure 16: Effect of cooling rate from the β -phase field on yield stress	19
Figure 17: Tensile fracture surfaces of fully lamellar structures, (a) $100^{\circ}\text{C min}^{-1}$; (b) $8000^{\circ}\text{C min}^{-1}$ [40].....	19
Figure 18: a) Microstructure of bi-modal) Bi-modal microstructure showing equiaxed α grains and decomposed β grains which form a lamellar matrix [40].....	20
Figure 19: Optical image of wrought Ti6Al4V microstructure [48]	21

Figure 20: Optical image of DMLS as-built Ti6Al4V microstructure [48].....	21
Figure 21: Microstructure of Ti6Al4V produced by SLM [51].....	22
Figure 22: A 50 μm optical image of DMLS Ti6Al4V microstructure heat- treated below 700°C, soaked for 1h with the furnace-cooled [58].....	23
Figure 23: A 250 μm optical image of DMLS Ti6Al4V microstructure heat-treated below 700°C, soaked for 1 hour then air-cooled [58]	23
Figure 24: A 50 μm optical image of DMLS Ti6Al4V microstructure heat-treated below 700°C, soaked for 1 hour then water-quenched [58]	23
Figure 25: Comparison of Young's modules of DMLS samples [16]	24
Figure 26: Locations where the tensile samples were obtained [62]	24
Figure 27: Tensile bars tested in research by Simoneli et al. [68].....	26
Figure 28: Optical micrographs showing the microstructure of as-built SLM Ti6Al4V; the arrows indicate in (a) the frontal plane, the pores in the microstructure, (b) the lateral plane, the dominant prior- β grain growth direction and (c) the horizontal plane. [68].....	26
Figure 29: Classification of residual stresses [70].....	27
Figure 30: Thermal cycling at different depths during laser melting of AISI 420 steel [71].....	28
Figure 31: Schematic showing heating and cooling phenomena of laser passes.....	28
Figure 32: Example of LOF porosity [28]	29
Figure 33: Optical micrographs of (gas-atomised powders showing pores within the powders on the left and cross-section of a laser deposit showing high level of gas porosity on the right [72].....	29
Figure 34: Recommended tensile test sample for DMLS according to ISO 6892 using Lt=80mm, Lc=40mm, L0=25mm, d0=5mm, d1=6mm, h=20mm [16]	35
Figure 35: Typical dimensions of standard 12.5-mm round tension test specimen and examples of small-sized specimens proportional to the standard specimen [79].....	36

Figure 36: Continuous and topological transformations of a simple object [81].....	37
Figure 37: Structural optimization problem [82]	37
Figure 38: Examples of (a) size optimization, (b) shape optimization and (c) Topology Optimization [2].....	38
Figure 39: SIMP procedure [92].....	40
Figure 40: Definition of the problem [99].....	40
Figure 41: Finite element analysis [99]	41
Figure 42: Sensitivity analysis [99]	41
Figure 43: Changed density [99].....	41
Figure 44: Typical example of the SIMP approach [2]	42
Figure 45: Elongation of a cylindrical metal rod subjected to a uniaxial tensile force F. a) The rod with no force applied on it; b) the rod subjected to the force F, which elongates the rod from length l_0 to l	47
Figure 46: Cubic body subjected to tensile stress.....	48
Figure 47: Typical stress-strain diagram [131].....	48
Figure 48: Linear part of an engineering stress-strain curve [31]	49
Figure 49: An illustration of necking [31].....	50
Figure 50: Single element [134].....	50
Figure 51: Single degree of freedom [134].....	51
Figure 52: Defining the nodes [134].....	51
Figure 53: Second element added to equation [134]	52
Figure 54: Applied boundary conditions [134].....	52
Figure 55: a) 45° strain rosette, b) 60° strain rosette [135].....	54
Figure 56: Geometry of DMLS tensile samples [16].....	57

Figure 57: MTS Landmark 370.10 description	58
Figure 58: Mechanical testing of samples.....	58
Figure 59: Sample orientation.....	59
Figure 60: ASTM E606 test specimen [138]	59
Figure 61: Determining the linear elastic region of a stress-strain graph.....	60
Figure 62: Linear elastic region	60
Figure 63: Determining 0.2% Offset Yield.....	61
Figure 64: Tensile test result for a 75° sample.....	62
Figure 65: Average UTS vs. printed orientation	63
Figure 66: Initial model	64
Figure 67: Design space.....	65
Figure 68: Axial load [135].....	65
Figure 69: Stress distribution [135]	66
Figure 70: Axially loaded shoulder fillet in stepped circular shaft [135]	67
Figure 71: Simulating tensile load in NX™ Pre/Post-application	68
Figure 72: Bending load shoulder fillet in stepped circular shaft [135].....	70
Figure 73: Simulation of bending moment in NX™ Pre/Post-application.....	71
Figure 74: A circular member a) before deformation and b) after deformation [135]	72
Figure 75: Axially loaded bar	72
Figure 76: Simulation of torsional load in NX™ Pre/Post-application.....	73
Figure 77: Simulation of combined loads in NX™ Pre/Post-application	74
Figure 78: Assigning imported material properties to initial model	74
Figure 79: Assign loads to model in Altair Inspire™	75

Figure 80: Optimization setup.....	75
Figure 81: Obtained Topology optimized geometry	76
Figure 82: Polynurb geometry	76
Figure 83: Exported geometry	76
Figure 84: CTETRA (10) with a 1-mm global element size	78
Figure 85: Mesh controls applied to stress concentrated areas	78
Figure 86: Assigning material properties to FEM model.....	79
Figure 87: FEA setup of Topology optimized model subjected to practical test conditions.	80
Figure 88: FEA results of FEA 7 as obtained from NX™12-Pre/Post-application.....	81
Figure 89: Position of maximum stress as obtained from NX™12-Pre/Post-application.....	81
Figure 90: FEA results for FEA 7 as performed in SOLIDWORKS® SIMULATION	82
Figure 91: Position of maximum stress as obtained from SOLIDWORKS® SIMULATION.....	82
Figure 92: Strain rosette positions	83
Figure 93:FEA setup of Topology optimized model subjected to initial conditions.....	83
Figure 94: Simulation results of Topology optimized model subjected to initial conditions	84
Figure 95: DMLS Topology optimized model.....	86
Figure 96: Applying black acrylic paint on DMLS Topology optimized model.....	87
Figure 97: Speckled pattern	87
Figure 98: Assembling the DIC system.....	88
Figure 99: Practical test of Topology optimized model.....	88
Figure 100: Applying virtual strain rosette.....	89
Figure 101: FEA 3: 29.36kN	90
Figure 102: Comparison of the resultant von Mises stresses for position 1 as obtained from the two practical test	93

Figure 103: Comparison of the resultant von Mises stresses for position 2 as obtained from the two practical test	93
Figure 104: Comparison of von Mises stress as obtained from FEA and practical test 1 at position 1	94
Figure 105: Comparison of von Mises stress as obtained from FEA and practical test 1 at position 2	94
Figure 106: Material extrusion	109
Figure 107: Vat polymerisation	109
Figure 108: Powder bed fusion.....	110
Figure 109: Material jetting	110
Figure 110: Binder jetting	110
Figure 111: Direct energy deposition.....	111
Figure 112: Sheet lamination.....	111
Figure 113:FEA 2: 25 kN.....	116
Figure 114:FEA 1: 20 kN.....	116
Figure 115: Comparison of von Mises stress as obtained from FEA and practical test 2 at position 1	119
Figure 116: Comparison of von Mises stress as obtained from FEA and practical test 2 at position 2	119

List of abbreviations

AM	Additive Manufacturing
ASTM	American Society for Testing and Materials
3D	Three-dimensional
CAD	Computer Aided Design
CAM	Computer Aided Manufacturing
DMLS	Direct Metal Laser Sintering
FEA	Finite Element Analysis
Ti6Al4V	Titanium with 6% aluminium and 4% vanadium
DIC	Digital Image Correlation
FEM	Finite Element Method
ISO	International Organization for Standardization
SLS	Selective Laser Sintering
FDM	Fused Deposition Modelling
UV	Ultraviolet
SLM	Selective Laser Melting
LMD	Laser Metal Deposition
EBM	Electron Beam Melting
LASER	Light Amplification by Stimulated Emission of Radiation
XRD	X-Ray Diffraction
E	Young's modulus of elasticity
UTS	Ultimate Tensile Strength
LOF	Lack of Fusion

SIMP

Solid Isotropic Material with Penalisation

CRPM

Centre for Rapid Prototyping and Manufacturing

1.1 Background

The long-term goal of this research is to design and develop a prosthetic arm to assist an amputee in being able to do on and off-road cycling as well as on and off-road motorbiking.

Since weight plays a significant role in cycling [1], topology optimization techniques is deployed with weight reduction as a significant constraint. According to Bendsøe et al. [2], the field of Topology Optimization is a mathematical approach that strives to optimize material structures in order to satisfy a given set of design requirements. The requirements include the geometry of the design domain, the amount of material to be used in the final design, boundary conditions and applied loads. In the design domain, the amount of available material is typically distributed into either dense or void regions, based on the results of the optimization. The process of topology optimization longs for many iterations in order to reach the optimum design in computer-aided software programs, however, these designs are quite frequently used as conceptual designs during the design process stage, and they are revised to meet performance and manufacturability standards further.

The iterative process of topology optimization generates complex structures [3]. These complex structures must be manufactured and evaluated. The chosen manufacturing technique would be Additive Manufacturing (AM) techniques since it enables the user to manufacture complex geometries [4–9]. According to ASTM standard F2792-10, AM is defined as the process of joining materials, layer upon layer, to form 3D models [10]. The general process of AM starts by forming a 3D model on Computer Aided Design (CAD) software. This CAD model is then virtually sliced by Computer Aided Manufacturing (CAM) software into thin horizontal layers and the selected AM process develops the physical 3D model by layer until the final component is completely built [11].

Evaluating Direct metal laser sintering (DMLS) complex geometries requires knowledge of the behaviour of such geometries under specified load conditions. Thus, a strength analysis of the DMLS complex geometry must be performed and evaluated in order to design and develop a lightweight prosthetic arm that assists an amputee in various cycling activities.

DMLS is a layered manufacturing process and, because of this, mechanical properties of the material depend on numerous factors [9]. To conduct a valid strength analysis, these factors must be taken into consideration and, therefore, a verifiable test specimen must be generated. The test

specimen's geometry should mimic the prosthetic arm, and therefore, it must be topology optimized with complex loads, torque, bending and axial.

1.2 Problem statement

The problem under investigation is therefore the validity of Finite Element Analysis (FEA) when applied to topology optimized DMLS structures manufactured from Ti6AL4V with the assumption that the weakest material's properties are homogeneous.

1.3 Research objectives

The major research objectives are set out:

Literature overview. The literature overview focusses on the broader spectrum of AM, structure optimising and the evaluation of DMLS structures. The focus is then narrowed down to identify current methods and assumptions for the validity of FEA on DMLS structures.

Develop a simulation model. After the detailed literature investigation, a topology optimized model is developed, thus incorporating the components identified.

Obtain simulation results. The developed simulation model is used to produce simulation results for comparison with the manufactured topology optimized model.

Experimental results. The mechanical test experimental results are obtained for validation of the simulated model.

Compare simulated and experimental data. The experimental and simulated results are compared in order to validate the simulation model.

Conclusion and recommendation. A conclusion is drawn and recommendations given for future studies.

1.4 Research methodology

To be able to address the listed research objectives, the methodology, as portrayed in the flowchart in Figure 1 is employed.

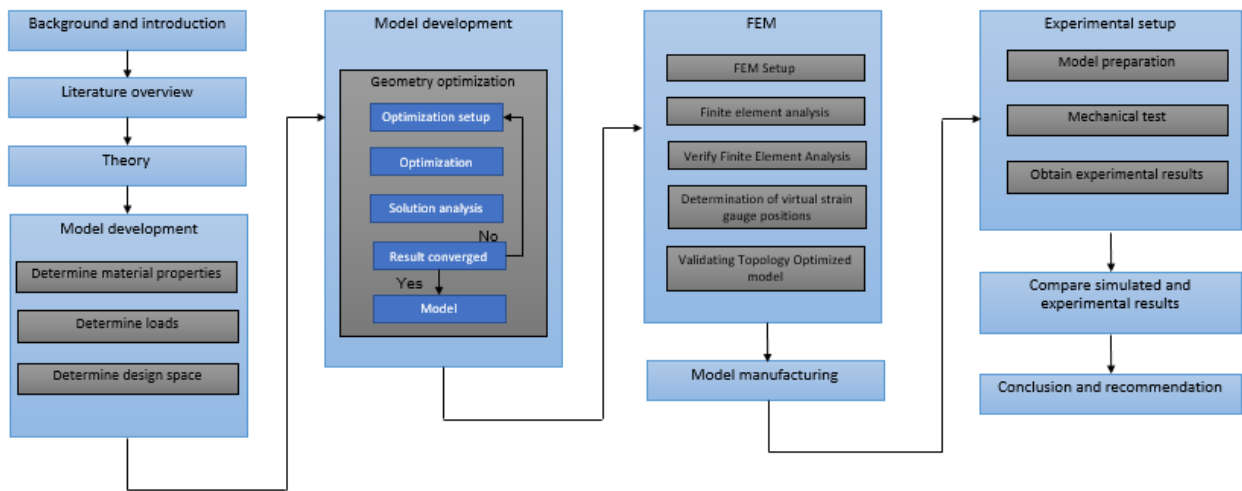


Figure 1: Research methodology

1.4.1 Literature overview

The literature overview strives to enlighten the reader of the theory on the relevant aspects and serves as a background for the development of a topology optimized model.

1.4.2 Model development

The material properties were obtained through tensile tests, and the weakest material properties are used for the model development. With the design space identified, the loads could be determined to induce the same maximum stress. This is done to ensure all the loads induces an equal effect on the geometry of the topology optimized model when the loads are combined. The iterative process of topology optimization of the model was done in solidThinking Inspire™. The topology optimized model is refined and exported for finite element analysis.

1.4.3 Finite Element Analysis

The FEA strives to mimic the conditions under which the topology optimized model is tested. The simulation results are obtained for the same load and boundary conditions, with the force being gradually applied in increments until the desired force is reached. The finite element analysis is performed in NX12 and verified by comparing with simulations done in SOLIDWORKS®.

1.4.4 Validating Topology Optimized model

In order to validate the topology optimized model, the maximum stress induced by the calculated loads on the initial model must be compared to the maximum stress induced by the same loads on the topology optimized model.

1.4.5 Obtain experimental results

A practical test is performed on the topology optimized model. A digital image correlations(DIC) system is used to virtually determine the strain at certain areas on the topology optimized model.

1.4.6 Validating finite element analysis

In order to validate the finite element analysis, the stresses obtained in the simulations must be compared to stresses detected during the experimental test. With the virtual strain gauges arranged in an orderly fashion, a strain rosette is formed. The strain rosette is used to determine the principal strains and, in turn, the principal stresses can be determined. The principal stresses are then used to determine the von Mises stress, which can be compared to the stresses obtained from the simulation. A conclusion can thus be drawn on the validity of FEA when applied to topology optimized DMLS structures manufactured from Ti6Al4V with the assumption that the weakest material properties are homogeneous.

1.5 Dissertation layout

Chapter 2 gives a literature overview on the relevant literature, namely DMLS, material properties of DMLS Ti6Al4V, FEM and topology optimization. The first section of the literature overview focusses on providing a broad background on AM, which is then narrowed down to literature applicable to DMLS. Factors influencing the quality of DMLS components and the material properties found in the literature are provided. The next section in this chapter deals with topology optimization and FEA of DMLS components as well as the validation process of FEA.

Chapter 3 focusses on providing the reader with a theoretical background on the basic principles of stress-strain curves, FEM, von Mises stresses and strain rosette. This theoretical background strives to create a basis from which the gap between theory and practically obtained results can be bridged.

Chapter 4 deals with the development of the topology optimized model. The background knowledge from the literature is used to obtain the material properties for DMLS components, identify the design space and calculate the loads. These factors are then incorporated into the topology optimization of the model. The topology optimization of the model aims to minimise the weight of the model and maintain structural integrity.

In Chapter 5, the FEM setup is done and an FEA is performed on the topology optimized model. The finite element analysis strives to resemble the conditions under which the model is tested practically. The FEA is performed in more than one software package in order to compare the

simulations and verify the FEA. Once the FEA is verified, the positions of the virtual strain gauge rosette are identified. The validation of the topology optimized model is also addressed in this chapter.

Chapter 6 explains the experimental procedure followed in this dissertation from model preparation to practical testing of the topology optimized model.

Chapter 7 discusses and compares the FEA results and the practically obtained results. Also, in this chapter is the verifiable conclusion on the validity of FEA when applied to topology optimized DMLS structures manufactured from Ti6AL4V with the assumption that the weakest material's properties are homogeneous.

Chapter 8 provides the conclusions made in the dissertation and makes recommendations on this research topic.

2.1 Introduction

In this chapter, an in-depth study of the literature applicable to DMLS, including the material properties, finite element analysis, topology optimization and evaluation process, is presented. The purpose of this chapter is to enlighten the reader on the theory of the applicable aspects and to serve as a background for developing the topology optimized model.

2.2 Additive Manufacturing

In 2015 the ISO/ASTM 52900 Standard was created to standardise all AM-related terminology and classify AM-related processes [10]. In this standard, a total of seven process categories was established, as represented in Figure 2. A short description of each process can be found in APPENDIX A.

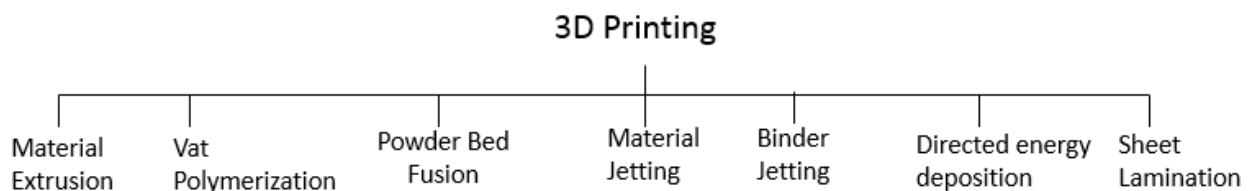


Figure 2: Seven types of AM processes [12]

Nannan et al states in [4] that metal products produced using AM processes can either be in an indirect or direct manner and is schematically represented in Figure 3. During the indirect processes, a binder is used to bond the metal particles together to form a green part which must be post-processed to obtain the desired density. The direct processes require a thermal heat source to melt the powder fully in order to create the final component.

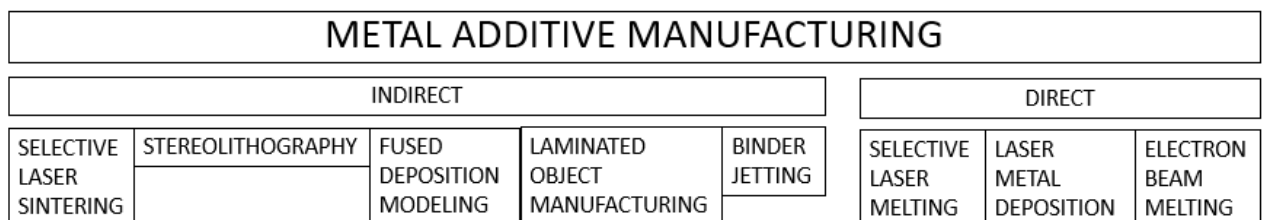


Figure 3: Classification of metal AM processes [4]

- Indirect metal AM methods

Metal components can be manufactured using a selective laser sintering (SLS) process by either melting the low-melting-point binder to bond metal particles together [4] or by partially melting the metal powder [13] to form a green part. Another method of forming a green metal component is by fused deposition modelling (FDM), where a metal powder bound in a type of plastic is extruded during this process. Stereolithography uses UV lights to cure the suspension made by mixing small metal particles into a liquid photo-curable resin, and with binder jetting a viscous liquid binder is used to bond metal particles and are sprayed onto the surface of a metal powder bed. To obtain the final desired properties, these green parts are sintered as a part of post-processing [14]. Laminated object manufacturing can be used to join sheets of metal in a layer-by-layer fashion.

- **Direct metal AM methods**

Methods like selective laser melting (SLM), laser metal deposition (LMD) and electron beam melting (EBM) are all examples of direct metal AM methods. DMLS completely melts fine metallic powders [15], and there is, in theory, no difference between DMLS and SLM [10], except that EOS uses the acronym DMLS [16]. These methods use a high-power heating source like a laser or electron beam. The heat source should have the capability to fully melt or sinter the powder and thus be able to heat the metal close to or higher than its melting temperature. The thermal energy delivery process can either be a laser scanning process, electron beam scanning process or welding based process [11]. Laser scanning processes like DMLS are widely used in the industry.

According to the American Society for Testing Materials [10], the DMLS AM process is a powder-bed fusion process in which thermal energy selectively fuses regions of a powder bed to form 3D parts out of metal powder without intermediate or green parts. As displayed in Figure 4, the DMLS process is a layered process where a thin layer of loose metal powder is laid down and a controlled laser-beam passes over the layer, fusing the powder together. Thereafter, a new thin layer of loose powder is laid down on top of the previous layer, and the controlled laser passes over and fuses the powder together with the other layers. This process repeats until the 3D part is formed.

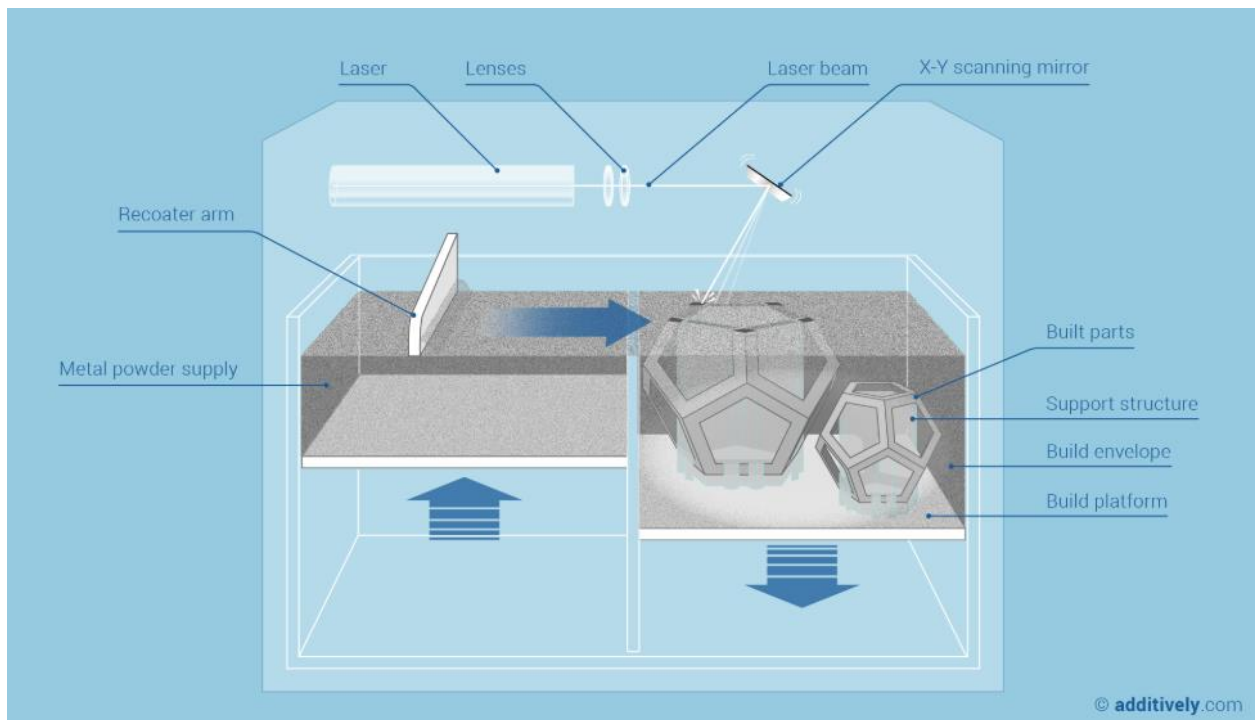


Figure 4: DMLS process [17]

2.3 Direct metal laser sintering (DMLS)

This AM process thrives in a wide variety of industries like biomedical, aerospace, automotive, chemical and high-tech. The fact the DMLS process makes it possible to obtain fully dense, near-net shape and custom once-off parts with minimum material wastage makes this technology both feasible and beneficial [18]. Another reason why this process thrives in these industries is its ability to help respond immediately to and bridge the gap between prototyping and production scenarios. Bridging this gap, however, requires knowing the parameters that influence DMLS.

Klocke et al. identified through their research that the microstructures and mechanical properties of as-built DMLS components do not merely depend on the material, and as such, they should rather be categorised into three major parameters [19], as schematically represented in Figure 5.

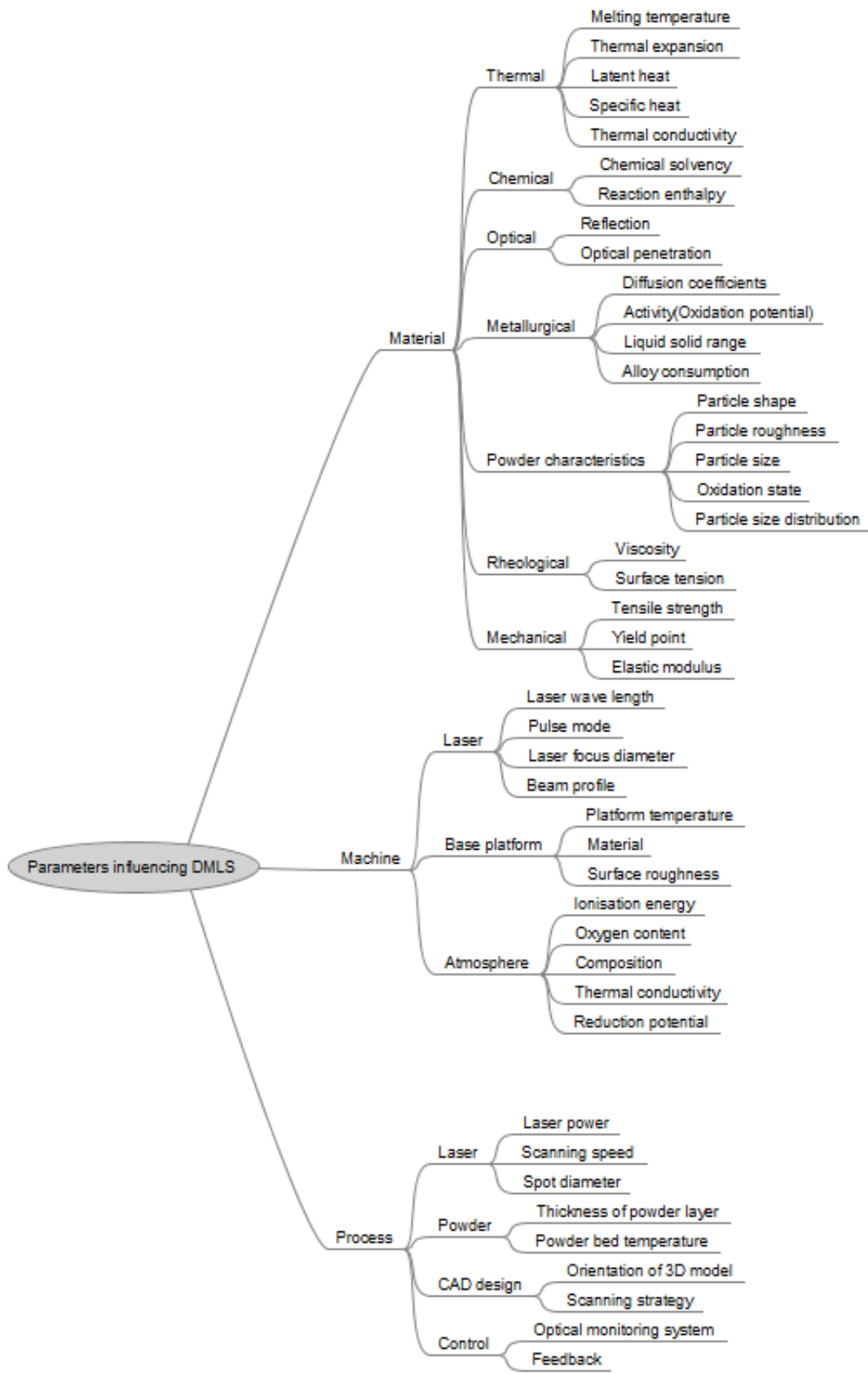


Figure 5: Parameters influencing DMLS [19]

2.3.1 Laser process

In modern DMLS systems, a fibre laser is used as the sintering or melting source. To understand how this laser affects the properties of DMLS components, a broad understanding of the process is necessary. Light amplification by stimulated emission of radiation, or, in short, LASER, emits highly collimated, coherent, single-frequency or single-colour light.

Figure 6 offers a schematic representation of a typical laser process. As observed, the process starts by pumping or pushing an electron into a higher orbit or excited state by exposing the atoms to large amounts of light. The majority of the electrons will quickly decay or move to a lower meta-stable phase where the electrons will linger around for a while before decaying back to ground state. An incoming photon emitted by an electron encourages the other electrons in the meta-stable state to emit their photons and decay back to ground state.

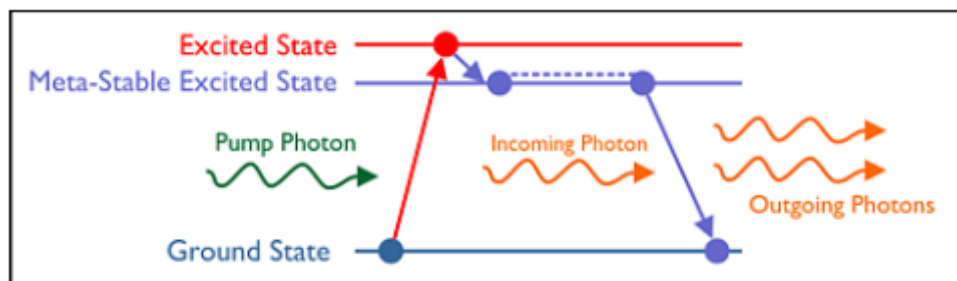


Figure 6: Schematic representation of electrons emitting photons [20]

To have a laser, this emitting process must be continuous, and this phenomenon is achieved by placing mirrors at either end of the laser medium as represented in Figure 7. The reflection of the mirrors causes more photons to be generated, which results in a laser cavity. By placing a partial mirror at the one end of the laser cavity, some of the generated light can be emitted from the laser.

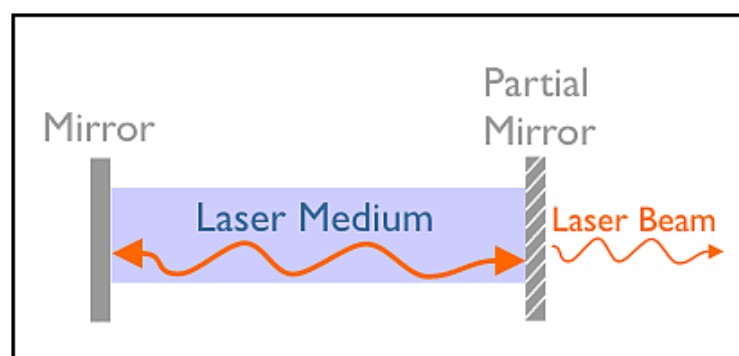


Figure 7: Schematic representations of continuous laser process [20]

A fibre laser uses a doped optical fibre as laser medium (Figure 8). The core of the fibre is doped with small amounts of rare earth materials such as erbium (Er^{3+}). This is done to obtain a meta-stable state with a wavelength of 1550 nm from photons with a wavelength of 980 nm. Thus, a pump light of 980 nm can be used to produce high-quality and high-power beams at 1550 nm. These fibre lasers can now produce up to 5 kW of laser power.

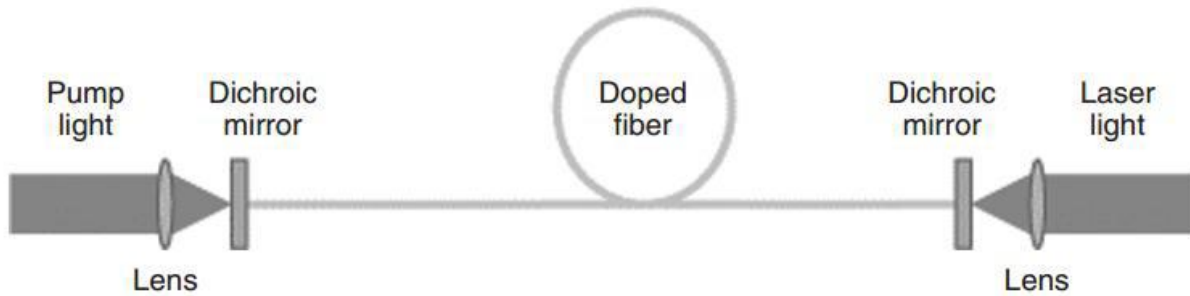


Figure 8: Schematic representations of a fibre laser [21]

The laser sintering and melting of metal powders is considered to be thermally induced rather than a chemical reaction. The metal powder when scanned by the laser will absorb some of the energy and some of the laser's energy will be transmitted into the workpiece without interaction and some energy will be reflected due to the discontinuity in the real index of refraction. This dispersion relation of a given material's index of refraction will determine the frequency of reflectivity. Thus, due to a metal's high opacities, only a small portion of the laser's energy will be transmitted into the material [22, 22].

According to Brown and Arnold [22, 22], a material's absorption coefficient α will cause the intensity of the radiation to decay with depth at a fixed material-dependent rate. This coefficient α is a function of temperature and wavelength, but with a constant α , the intensity decays exponentially with depth z according to the Beer-Lambert law:

$$I(z) = I_0 e^{-Az}, \quad (1)$$

where I_0 is the intensity just inside the surface after considering reflection loss. Figure 9 shows optical absorption depths as a function of wavelength for various metals and semiconductors.

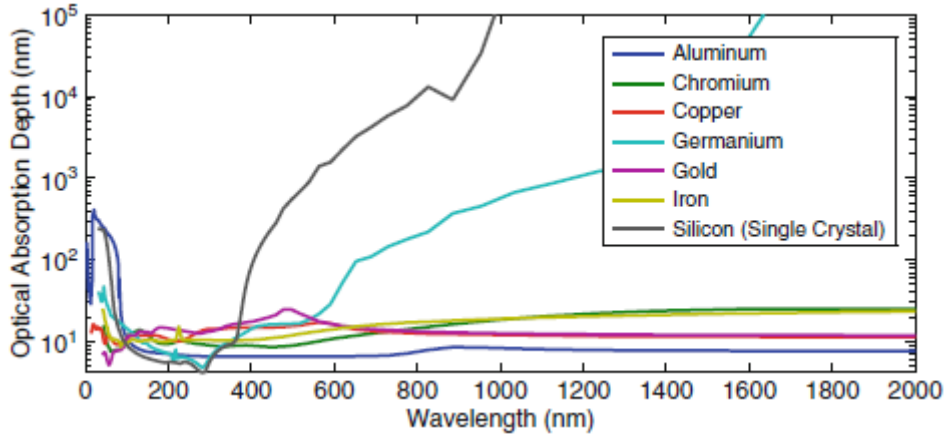


Figure 9: Optical absorption depths for several materials over a range of wavelengths [23]

In metals, optical absorption is dominated by the free electrons through such mechanisms as inverse bremsstrahlung. Energy is subsequently transferred to the crystal lattice by photon collisions. The kinetic energy of the atoms is raised, which leads to elevated temperatures of the material [24]. When the melting temperature of the material is reached, a liquid pool is formed. The scan speed of the laser determines the temporary existence of the liquid pool, and the temporal and spatial evolutions of the temperature field inside a material are governed by the heat equation. This equation is derived from Fourier's law of heat conduction and the conservation of energy. The heat equation states that the local heat flux is proportional to the negative of the temperature gradient, and in a coordinate system that is fixed with the laser-beam, the equation is as follows:

$$\rho c_p \frac{\partial T}{\partial t} - \nabla[k \nabla T] = Q, \quad (2)$$

where ρ is density, c_p is heat capacity, k is thermal conductivity, and Q is heat generated per unit volume.

The solidification of the molten pool results in the formation of DMLS tracks. The tracks adjacent to each other form a layer of processed material. Multiple layers of combined tracks then form a 3D object or part.

2.3.1.1 Single-track formation

The laser-beam melts the metal powder along a fixed path determined by a software interface to generate a molten track in the deposited layer. The molten track can be broken up into a row of spheres or drops. When the non-optimal process parameters are present, a well-known drawback of laser melting comes forth in the form of the balling effect, as displayed in Figure 10. To avoid

this balling effect, the optimum process parameters should be present to ensure a continuous single track with enough molten material. The amount of liquid phase present is determined by the melting temperature and the parameter that influences this is the amount of energy transferred to the powder. This energy is affected by two main parameters, namely laser power and scan speed.

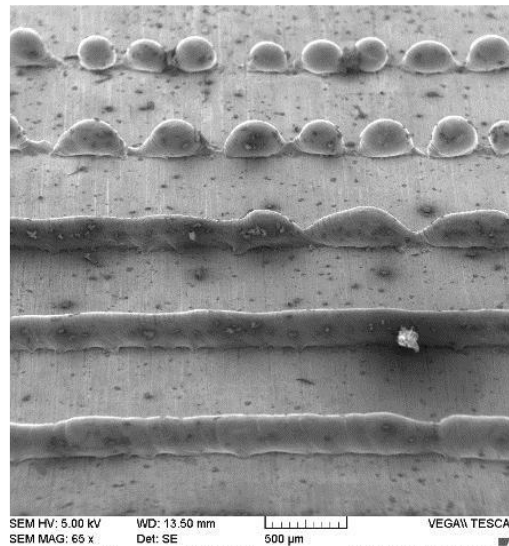


Figure 10: Single tracks at the substrate [25]

An article by Yadroitsev [26] concludes that the process parameters employed by DMLS directly influence the single-track formation of the material and, in turn, since the single-track formation is the first step in forming the final part, it affects the whole component. Furthermore, the author observes that when the optimum process parameters are deployed, the single tracks are continuous and its metallurgical bond with the substrate (whether physical substrate or previously melted layer) is consistent.

2.3.1.2 Single-layer formation

The single layers are just an extrapolation of the single track, and the surface morphology thus depends on geometrical characteristics of single tracks, hatch distance and scanning strategy [18, 27].

The geometric characteristics of single tracks are discussed under section 2.3.1.1. Figure 11 demonstrates the influence of the hatch distance with a hatch distance variation of 60, 120 μm and 240 μm . The hatch distance is the distance between adjacent tracks. From Figure 11 it can be concluded that the hatch distance affects the amount of powder being melted, and with a hatch distance of 120 μm and $\sim 70 \mu\text{m}$ laser-spot diameter, SS-grade 904L powder is melted in a sequence of tracks with the same geometric characteristics. This leads to homogenous layers

with constant thickness and bonding between tracks. The conclusion can further be made that reducing the hatch distance results in changes in the thermo-physical conditions of the synthesis. The laser-beam thus directly interacts with the powder, the substrate and the previously synthesised track, which will influence the morphology of the layer. Increasing the hatch distance leaves many powder particles un-synthesised, which results in porous components. Yadroitsev thus concludes that the hatch distance is a critical parameter that affects the surface morphology and in turn the morphology of the whole component [27].

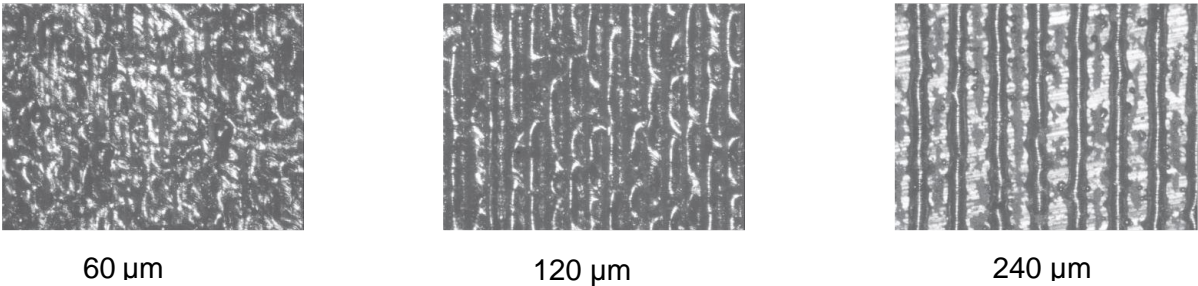


Figure 11: Surfaces of the first layer from SS-grade 904L powder obtained at different hatch distances [27].

The scanning strategy is patterns formed by tracks of each layer and single layers which are stacked upon each other to form a hatch angle as displayed in Figure 12. The scanning strategy also influences the microstructure of DMLS objects, and changing the scan direction at each layer can affect the prior-β grain growth direction, the origin of the relationship is empirical and, according to Thijs et al., not yet well-understood [28]. However, from Table 1 can be concluded that the hatch angle does indeed play a role with regards to mechanical properties.

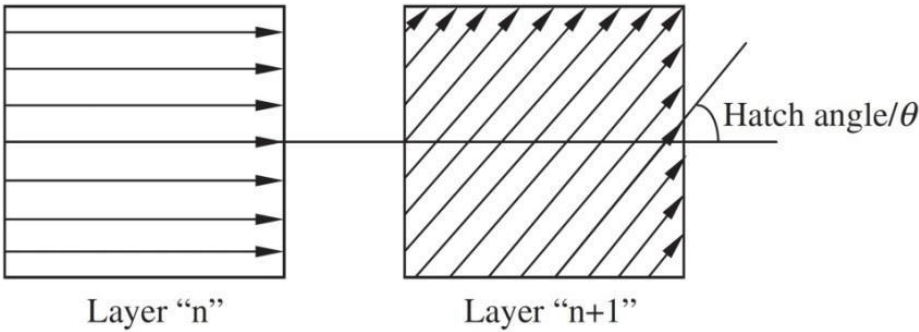


Figure 12: Rotations in scan strategy in neighbouring planes [29]

Table 1: Tensile properties of SLM 304 stainless steel samples with varying hatch angles [30]

Hatch angle (°)	YS (MPa)	UTS (MPa)	Elongation (%)
90	530-551	696-713	32.4-43.6

105	566-570	714-717	40.6-42.8
120	540-545	682-685	36.5-38.4
135	541-556	691-693	36.6-38.4
150	534-555	698-703	39.6-40.4

2.3.2 Mechanical properties of DMLS Ti6Al4V

According to EOS in their white paper on Mechanical testing of DMLS Parts, the mechanical properties of Ti6Al4V components when the process parameters are kept constant are drastically affected by the components' geometry, build orientation and surface finish [16].

2.3.2.1 Microstructure

The mechanical properties of DMLS Ti6Al4V have been investigated extensively over the past few years, and differences in wrought Ti6Al4V and DMLS Ti6Al4V come to light when examining the microstructures. Ti6Al4V is an α - β alloy with 4wt% vanadium stabilising the β phase and 6wt% aluminium stabilising the α phase [31]. The types of microstructure that can be found in commercial Ti6Al4V are lamellar, bi-modal and equiaxed [32–34].

In Figure 13, a micrograph of an **equiaxed** microstructure is presented. The term "equiaxed" refers to a polygonal structure in which individual grains have approximately equal dimensions in all directions. This microstructure primarily consists of α grains, but around eight percent of β grains are present on either the grain boundaries or at the triple points.

A study by Lütjering, Albrecht and Ivasishin [35] concluded that prior- β grain size has little or no influence on the yield stress but a strong influence on ductility. This phenomenon, due to the length of the β grain boundary, is what limits the maximum slip length in the grain boundary α layer; therefore, the stress concentration at grain boundary triple points is reduced for a small β grain size, which results in a higher ductility for a smaller β grain.

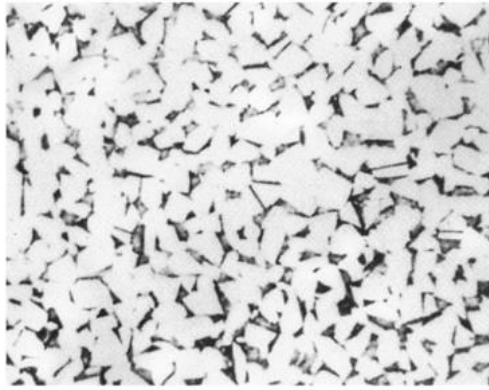


Figure 13: Equiaxed microstructure of a titanium alloy showing globular α grains (light) with β phase (dark) present at grain boundaries and triple points [34]

The **lamellar** microstructure would look similar to the microstructure in Figure 14, and Figure 15 displays the effects of different cooling rates.



Figure 14: Light micrographs showing a typical lamellar microstructure [34]

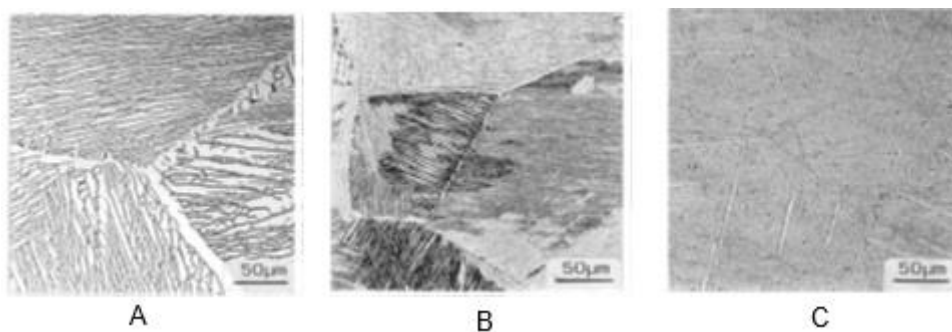


Figure 15: Optical micrograph showing examples of fully lamellar microstructures derived from different cooling rates; A) slow and B) intermediate cooling rate, C) quenching [35]

Lütjering found that the cooling rate has a significant effect on the production of fully lamellar microstructures. The temperature and time of the β phase field treatment determine the size of

the grains in the β phase field, also known as prior- β grain size. In Figure 15 A, furnace cooling is used to produce lamellar microstructure with packets of α laths arranged in a parallel manner (also known as α colonies) and generally contains a retained lamellar β phase around the α grain boundaries [35].

The basketweave microstructure (also known as Widmansätten microstructure) is created when Ti6Al4V is air-cooled. The basketweave microstructure (Figure 15 B) contains α laths that are arranged similarly to a weave pattern of a basket with a limited retained β phase, and if present, it is located at the α grain boundaries [36]. In Figure 15 C, a fine martensitic microstructure with no retained β phase can be observed due to the increased cooling rate by water or oil quenching.

Table 2: Properties of fully lamellar Ti-6Al-4V obtained with altered processing conditions [36–38]

Alloy	Yield strength [Mpa]	UTS [Mpa]	Elongation [%]
Ti6Al4V Water quenched	1035	1095	13
Ti6Al4V Air quench	970	1040	15
Ti6Al4V Furnace cooling	910	980	16
Ti6Al4V Cast	900-100	950-1050	5-7
Ti6Al4V Cast+HIPing	800-900	850-950	8-10

Lütjering [39, 40] concludes that the size of the α colonies is the greatest influential microstructural parameter on the mechanical properties of the fully lamellar structures. Studies have confirmed that the α colonies determine the effective slip length, and with an increase in the cooling rate, the α colonies decrease, which in turn causes the slip to decrease and results in a higher yield stress ($\sigma_{0.2}$) [39, 40]. This phenomenon is supported by the results in Table 2. In Figure 16, a

drastic increase in yield strength can be observed because of the fact that the colony structure changes to a martensitic type of microstructure at this cooling rate [41]. Here, the slip length and colony size equal the width of individual α plates [40].

However, this hypothesis of the variations of the yield stress solely depends on the α -colony size is, according to Kar [42] just speculation – he explains that the cooling rate changes the microstructure in a very complex manner. Not only does the cooling rate affect the α -colony size but also the size and morphology of other microstructural features. Kar then concludes that it is not possible to use experimental methods to obtain a physical picture of the dependence of a particular property on a single parameter. This type of physical model of relating a property to a particular parameter is only a proposition [42], and Kar found that yield strength is influenced by the scale of the colonies, α -lath thickness and prior- β grains.

Subsequently, another important microstructural parameter in terms of the effect on the mechanical properties of fully lamellar structures, according to Lütjering and Williams [40, 43], is the length of prior- β grains. Fully lamellar microstructures with long prior- β grain boundaries generally exhibit poor ductility and resistance to short crack propagation.

Regarding the ductility and increase in cooling rate referred to in Figure 16, Lütjering found that the ductility gradually increases with an increase in the cooling rate, but the graph then passes through a maximum, and the ductility decreases drastically. The reason for this is a fracture mechanism change, as seen in Figure 17. The author further explains that the fracture mechanism changes from a ductile trans-crystalline dimple type of fracture mode to a ductile inter-crystalline dimple-type fracture mode along the continuous α layer at the β grain boundary [40]. These conclusions are supported by the study of Leyens and Peters [44].

Wallem and Boyer [38] investigated the correlation between microstructural features in different conditions and how they affected the tensile strength and ductility. They found that the faster cooling rates would result in a finer transformed structure, which results in higher strength. According to Ambard et al. [45] many glide systems can be activated in globular grains while the α colonies act as a single grain within which only the basal system is activated. The piling up of high-stress concentrations at α -colony boundaries from many dislocations of the same nature is the reason for the α colonies being more determinable from the ductility properties than from globular grains. They finally conclude that α -colony size is an important microstructural parameter as far as ductility is concerned [45].

Kar [42] found that while prior- β -grain size has little or no influence on the yield strength, it has a strong influence on ductility. Ductility depends on β grains, the length of β -grain boundary limits the maximum slip in the boundary layer [42].

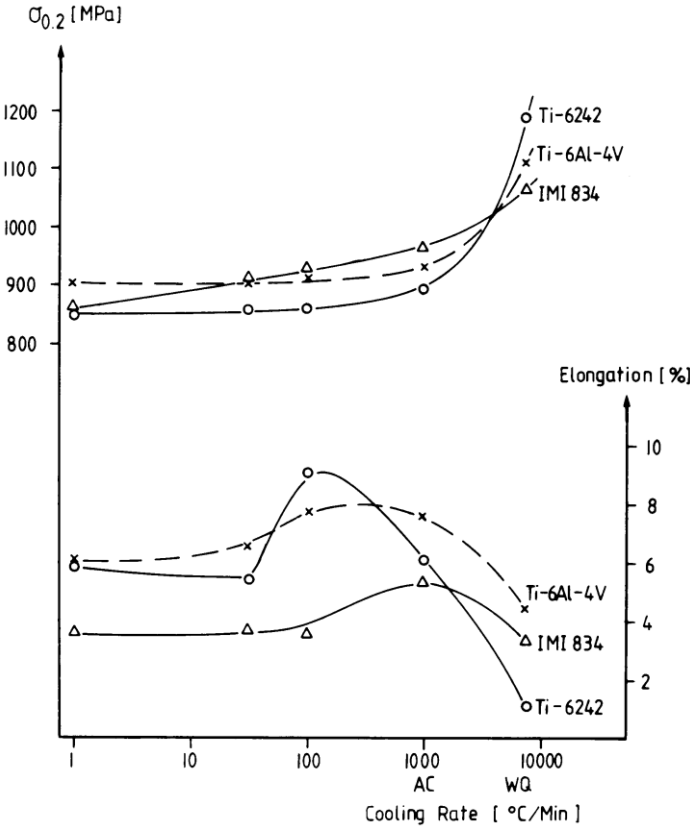


Figure 16: Effect of cooling rate from the β -phase field on yield stress and ductility of fully lamellar structures [40]

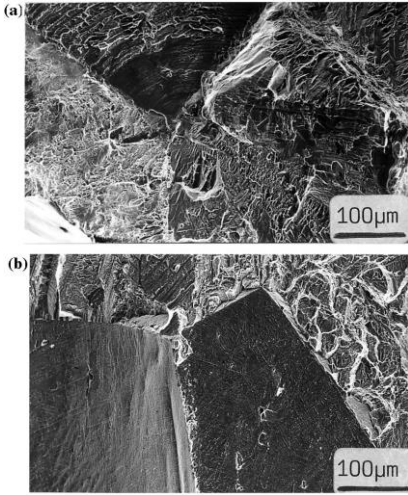


Figure 17: Tensile fracture surfaces of fully lamellar structures, (a) 100°C min⁻¹; (b) 8000°C min⁻¹ [40]

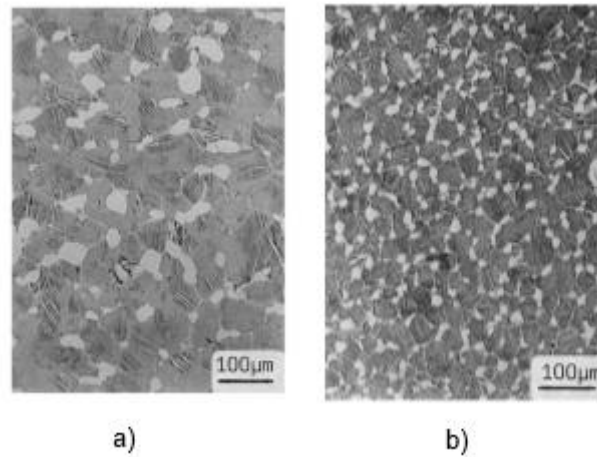


Figure 18: a) Microstructure of bi-modal) Bi-modal microstructure showing equiaxed α grains and decomposed β grains which form a lamellar matrix [40]

According to Lütjering the most influential microstructural parameter on the mechanical properties of bi-modal microstructures is: “the size of the β grains in the microstructure that is inversely proportional to the size of primary equiaxed α grains (α_p) and their volume fraction [40]”. As shown in Table 3, with the increase of the volume fraction of the α_p , the ductility and strength of the alloys increase [46]. The actual size of the β grains, instead, determines the final maximum α -colony size, and therefore small β grains are associated with high yield strength, decent ductility, and superior resistance to high-cycle fatigue [40].

Table 3: Properties of Ti-6Al-4V with bimodal microstructure [46, 47]

Alloy (% volume fraction α_p)	Yield strength [Mpa]	UTS [Mpa]	Elongation [%]
Ti6Al4V (10)	940	990	12.3
Ti6Al4V (30)	972	1069	14

From the optical image in Figure 19 of the microstructure in the longitudinal direction of wrought Ti6Al4V, it is clear that the bar consists of a fully equiaxed microstructure with intergranular β . On the other hand, with a DMLS Ti6Al4V as-built microstructure one could conclude, by referring to Figure 20, that the bar consists of a fine acicular α' -martensitic microstructure and columnar prior- β grains which are oriented more or less in the building direction [48–50].

Luca et al. [51–53] performed an X-Ray diffraction (XRD) analysis and indicated only the presence of the α phase, which can be recognised as both the α phase and the α' martensite, as seen in Figure 21. According to Becker et al., the microstructure of as-built DMLS Ti6Al4V may be

interpreted as martensitic [54]. Simonelli [55] explains that Ti6Al4V is an allotropic alloy that transforms fully into the β -phase field above the β -transus temperature and into an α + β -phase mixture below this critical temperature and the cooling rate from the β -phase field determines the amount of β phase retained at room temperature. Additionally, because of the rapid cooling of each layer during the SLM process (in the orders of thousands of degrees per second), the microstructure is fully martensitic.

The difference in the microstructures between wrought and DMLS Ti6Al4V is a result of the manufacturing process. During a DMLS process, the uneven, fast cooling causes inhomogeneity, thus resulting in a β -to-martensite transition [54].

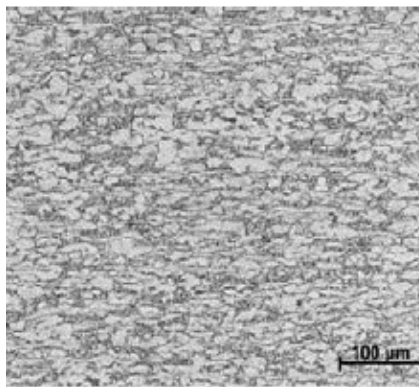


Figure 19: Optical image of wrought Ti6Al4V microstructure [48]

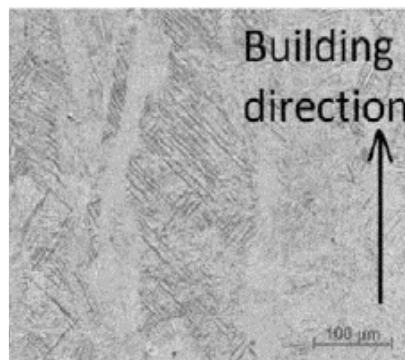


Figure 20: Optical image of DMLS as-built Ti6Al4V microstructure [48]

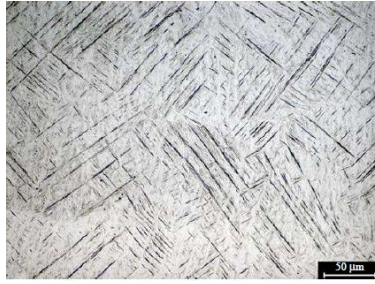


Figure 21: Microstructure of Ti6Al4V produced by SLM [51]

The mechanical properties of titanium alloys are highly dependent on the microstructure [48, 51]. Thus, the yield strength and ultimate strength of as-built DMLS Ti6Al4V are greater than that of wrought Ti6Al4V and conversely with ductility due to the fact that martensitic microstructure morphology exhibits a high strength and hardness but low ductility [54]. Vrancken et al. demonstrated the combined effect of martensite, micro cracks and residual stress is responsible for low ductility [50]. Another reason for the higher yielding of DMLS Ti6Al4V is that the fine powder used to produce components creates smaller grains sizes, which in turn provide higher yielding by inhibiting the dislocation motion according to the Hall-Petch equation:

$$\sigma_y = \sigma_0 + \frac{k}{\sqrt{d_g}}, \quad (3)$$

where σ_y is the yield stress; σ_0 a material's constant for the starting stress of the dislocation movement (or the resistance of the lattice to dislocation motion); k the strengthening coefficient (a material-unique constant); and d_g the average grain diameter [31]. This microstructure morphology can be altered with heat treatment.

The heat treatment process produces hardness and softness and improves the mechanical properties like tensile strength, yield strength, ductility, corrosion resistance and creep rupture, thus having a tremendous effect on the morphology of microstructure [31]. Therefore, the process can be described as the controlled heating and thereafter cooling of components to alter the material's microstructure in order to obtain certain desired mechanical properties [56]. The Ti6Al4V alloy is an α - β alloy and is suitable for various heat treatment processes to obtain different microstructures through different processes [54]. The overall microstructure of this alloy depends on the process history as well as post-process heat treatments, which make the heat treatment of the microstructure complex [57]. Given the microstructure's complexity, it is not necessarily the microstructure that provides the best combination of static strength and ductility that in turn deliver the optimum fracture toughness, fatigue strength or resistance to crack growth.

According to the study done by Ramoseu [58], heat treatment of DMLS Ti6Al4V below 700°C, which is much lower than the β -transus temperature, did not result in much of a difference in the microstructure of the DMLS samples. This occurrence was observed by a number of other authors [50, 59, 60]. Ramoseu [58] further indicates that by increasing the rate of cooling after heat treatment below 700°C does result in any significant change in the microstructural features as long as the cooling is homogeneous. From Figure 22, Figure 23 and Figure 24 it can be concluded that the microstructure consists of fine martensitic platelets.

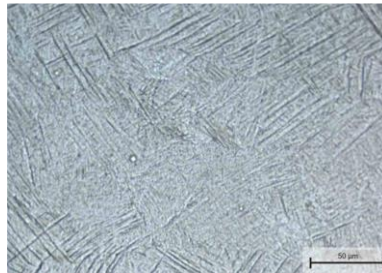


Figure 22: A 50 μm optical image of DMLS Ti6Al4V microstructure heat-treated below 700°C, soaked for 1h with the furnace-cooled [58]



Figure 23: A 250 μm optical image of DMLS Ti6Al4V microstructure heat-treated below 700°C, soaked for 1 hour then air-cooled [58]

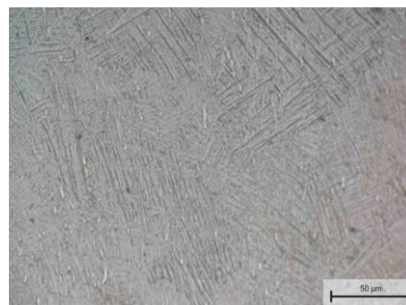


Figure 24: A 50 μm optical image of DMLS Ti6Al4V microstructure heat-treated below 700°C, soaked for 1 hour then water-quenched [58]

According to Donachie, residual stress can successfully be reduced within components by heat treatment [57] without alternating much of the microstructure of as-built DMLS Ti6Al4V parts since the stress relieving takes part at temperatures below 700°C and below β -transus temperature [58].

2.3.2.2 Geometry

When keeping the parameters influencing DMLS components the same (refer to Figure 5), except for the building geometry, it becomes evident from Figure 25 that the geometry of the specimen does play a role on the mechanical properties [16]. This phenomenon is the result of the microstructure being influenced by the building geometry [61, 61]. When building geometry is kept constant as in Figure 26, the geometry of the samples that have been machined out of this build geometry has little effect on the mechanical properties [62]. Another reason for this phenomenon is the fact that residual stresses affect the tensile properties of DMLS components, as residual stresses are geometry-dependent [63].

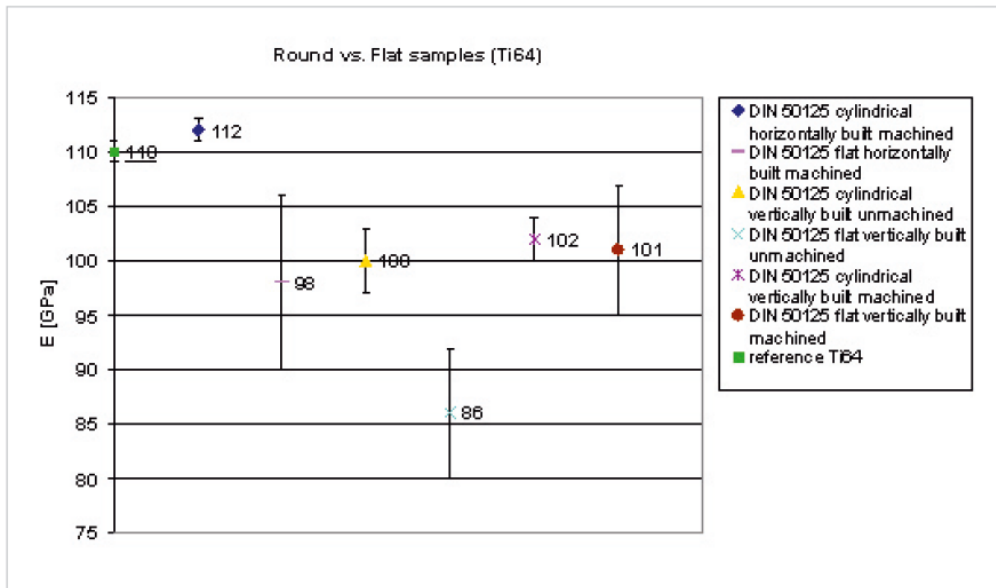


Figure 25: Comparison of Young's modules of DMLS samples [16]

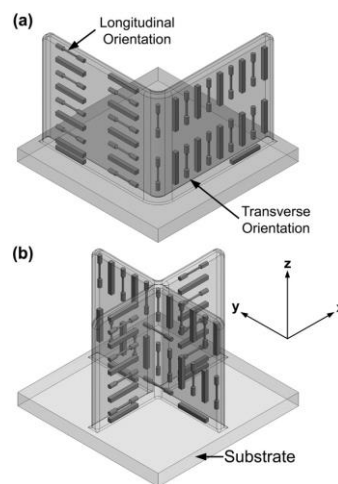


Figure 26: Locations where the tensile samples were obtained [62]

2.3.2.3 Surface finish

According to the test done by EOS GmbH Optical systems, the machined specimens displayed both higher Young's moduli and lower standard deviations than their unmachined counterparts, as displayed in Figure 25 [16]. Rafi [64] indicated that the surface finish of DMLS samples can affect the mechanical properties. The influence of the surface finish, however, is far less significant for tensile properties than fatigue properties, since the surface roughness can cause stress concentrations and enhance crack growth [65, 66]. A study by [67] investigated the influence of surface finish by testing polished and unpolished samples. The author concluded that the sample's UTS did increase after polishing. The surface finish proved to have a bigger effect on the miniature samples than the standard samples, as can be seen in Table 4.

Table 4: Tensile properties of DMLS samples indicating the effect of surface finish [67]

Specimens	UTS [MPa]	Elongation [%]
Standard round machined	1238±9	10.74±0.7
Standard round	1200±50	11±2
Polished mini samples	1172±144	6±0.9
Non polished mini samples	811±54	6.4±1.4

2.3.2.4 Build orientation

In Figure 28 an optical micrograph is showing that the microstructure of the as-built component is fully α' martensitic and only the vertical grain boundaries of the prior- β can be discerned. Simonelli et al. [68] found:

“Due to the layer-wise nature of the process, the prior β grain grow in a columnar way almost vertically through several layers in a range of 1-3mm, while the mid-length average width of the prior- β grains is $103 \pm 32 \mu\text{m}$. They concluded that the microstructure of the frontal and lateral planes differs significantly from the microstructure on the horizontal planes parallel to the build platform”.

Table 5 presents the tensile properties of the tensile bars tested as printed in Figure 27.

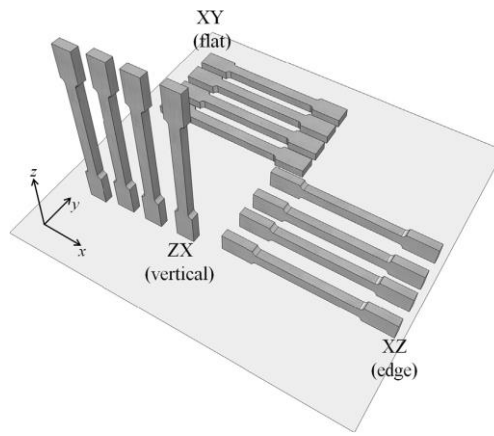


Figure 27: Tensile bars tested in research by Simoneli et al. [68]

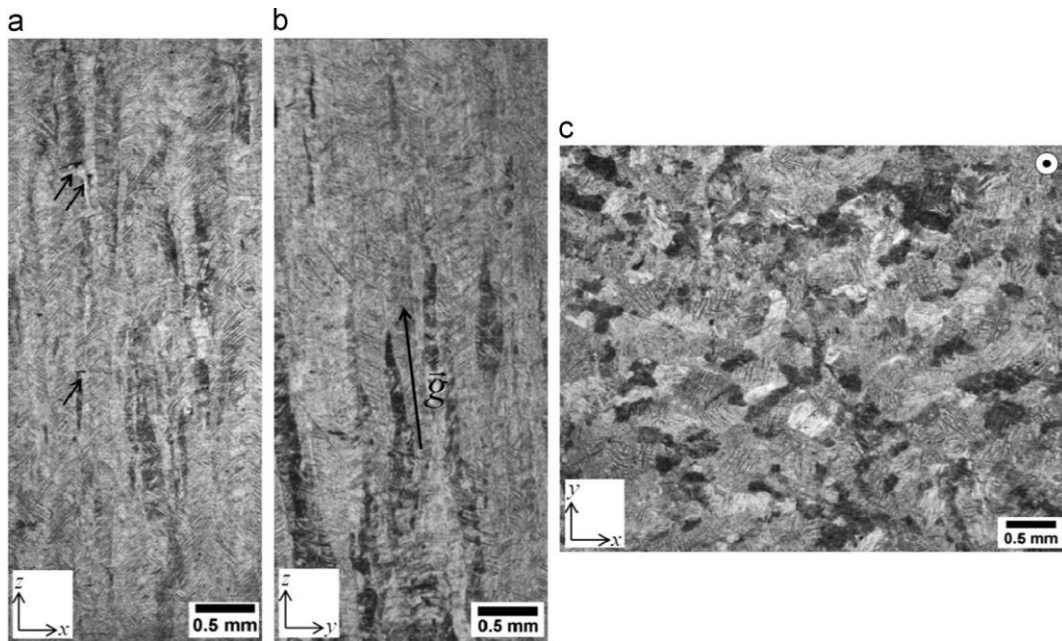


Figure 28: Optical micrographs showing the microstructure of as-built SLM Ti6Al4V; the arrows indicate in (a) the frontal plane, the pores in the microstructure, (b) the lateral plane, the dominant prior- β grain growth direction and (c) the horizontal plane. [68]

Table 5: Tensile properties of as-built SLM bars [68]

Print direction	E [GPa]	σ_y [MPa]	UTS [MPa]	Fracture [%]
xz	115 \pm 6	978 \pm 5	1143 \pm 6	11.8 \pm 0.5
zx	119 \pm 7	967 \pm 10	1117 \pm 3	8.9 \pm 0.4
xy	113 \pm 5	1075 \pm 25	1199 \pm 49	7.6 \pm 0.5

Simonelli et al. found that the orientation of the prior- β grain has no significant influence on the modulus of elasticity (E), but it does tend to influence other tensile properties. On the other hand, the literature reports that the α crystal anisotropy has been marked to have a significant effect on the modulus of elasticity [69]. However, Simonelli and others [69], [60] have found that all SLM Ti6Al4V samples have a weak α' (or α) texture, which explains why the modulus of elasticity does not vary when the build orientation is changed. Interlayer porosity can occur during SLM, and the vertical bars consist of the highest number of layers, which explain why the vertical bars have the lowest yield strength and UTS. It was also concluded that the ductility depends on the build orientation of the parts [68] because prior- β grains of a given layer tend to grow epitaxial on the grains of the previous layers, thus assuming an elongated morphology parallel to the direction for maximal heat conduction [59].

2.3.2.5 Residual stresses

When a part is printed successfully without deformation or delamination in the absence of an external force or thermal gradient, the part can still deform from residual stresses induced during the process. Paranjpe [70] classified residual stresses as displayed in Figure 29.

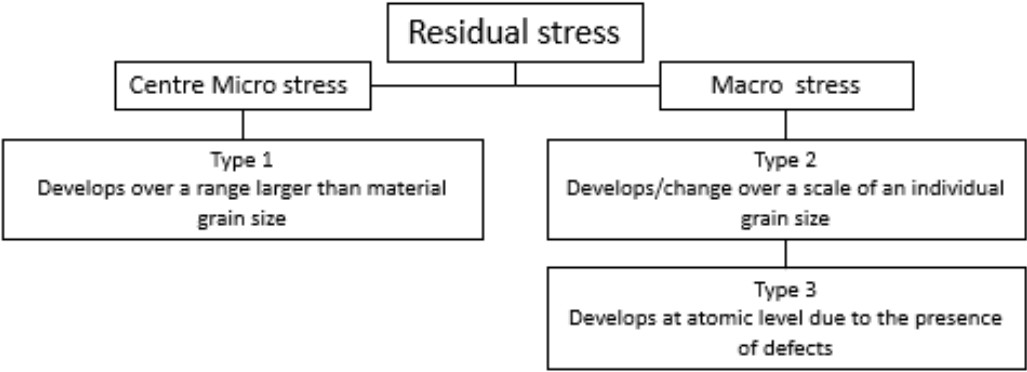


Figure 29: Classification of residual stresses [70]

Since the DMLS cycle naturally induces a local concentrated temperature gradient mechanism from the laser spot's size being 10 μm -150 μm , which produces a very small melt pool, and the related plastification thus results in residual stresses and part deformation. Figure 30 exhibits a result of this thermal cycling during DMLS. From Figure 31 it can be seen that the reduction in volume because of rapid cooling or solidification leads to strain. Already-solidified layers constrain the physical shrinkage of the top layer, which leads to residual stresses within the component. Subsequently, it can be observed that the residual stresses in the laser-melting process are built up of the quenching stresses caused by the solidification of the deposited layers and the thermal stresses from the misalliance between the thermal expansions and stiffness of the different

materials and the different states of the same material. These stresses can exceed the yield strength of the material and have been reported to initiate deformation and premature fracture of the component [18, 22].

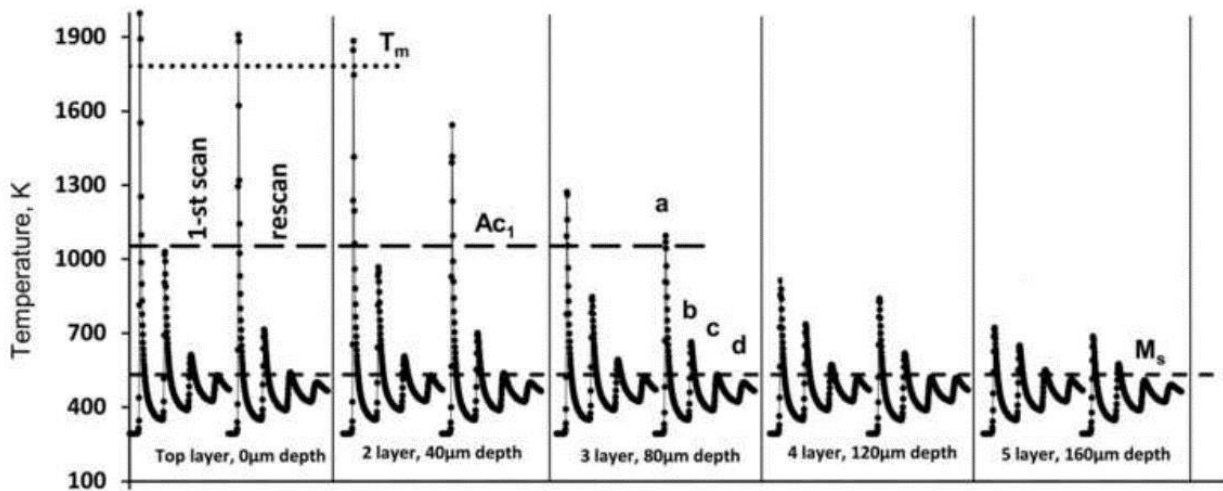


Figure 30: Thermal cycling at different depths during laser melting of AISI 420 steel [71].

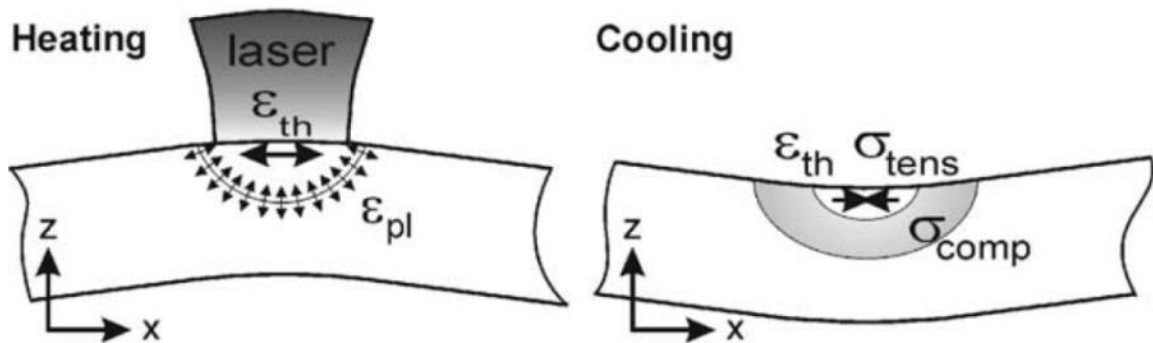


Figure 31: Schematic showing heating and cooling phenomena of laser passes

By performing a simplistic heat treatment process below the β -transus temperature before removing the part from the build plate and support structures, the deformations and distortions can be minimised or circumvented [49]. The Ti6Al4V alloy will begin oxidising when heated above 427°C in an unprotected environment; therefore, stress relieving should take part in an oxygen-depleted atmosphere e.g. argon atmosphere or vacuum. Donachie [57] found that when stress relieving the sample, the cooling rate, once the sample is heated, is not critical, although the uniformity of the cooling rate is of absolute importance.

2.3.2.6 Porosity

The literature shows that pores could either be seen as beneficial or as a defect [63]. Two main types of pore have been found to exist in metal AM, namely lack of fusion (LOF) and gas porosity. The LOF porosity occurs due to a poor choice of processing parameters, and the shape is random as seen in Figure 32. Gas porosity is spherical pores that apparently occur from gas trapped in the raw metal powder particles (as seen in Figure 33) or trapped environmental inert gas during the melting process; however, the exact causes of gas pores are still inconclusive [63]. The gas pores are formed inherently in a single melt pool, and it is generally difficult to detect with an in-situ monitoring system, however, the opposite in terms of in-situ monitoring applies for LOF pores, which shows early signs of formation at a given layer. Since pores can initiate stress concentrations and are therefore classified as failure-initiation points, it is desirable to reduce porosity in manufactured components.



Figure 32: Example of LOF porosity [28]

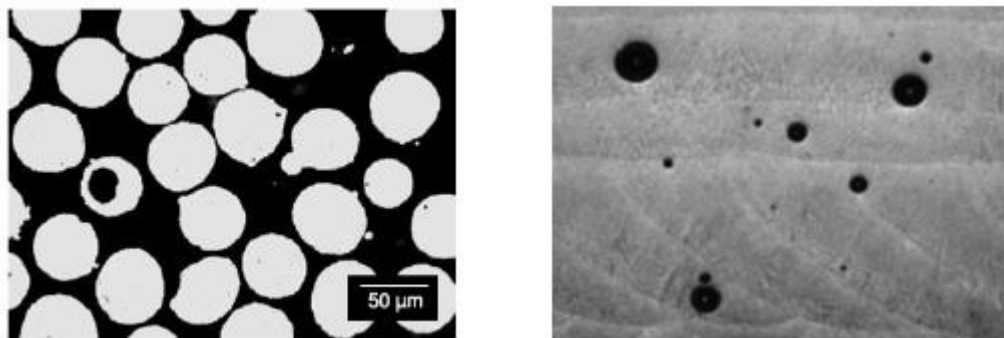


Figure 33: Optical micrographs of (gas-atomised powders showing pores within the powders on the left and cross-section of a laser deposit showing high level of gas porosity on the right [72]

2.3.2.7 Summary of mechanical properties out of the literature

In Table 6, the mechanical properties as found in the literature are presented.

Table 6: A summary of the literature regarding the mechanical properties of DMLS Ti6Al4V

Ref.	Process	Surface finish	HT	Build Orientation	UTS [MPa]	YS [MPa]	Elongation [%]	Young Modulus [GPa]
[73]	EBM	M	AB	xy	970±10	900±20	11.5±2[F]	NS
	EBM	M	AB	z	950±20	880±70	13.4±1.2[F]	NS
[54]	DMLS	AB	AB	xy	1155±20	NS	4.1±2[F]	NS
	DMLS	AB	SR	xy	1230±20	NS	7±2[F]	NS
[74]	DMLS	P	AB	xy	1043.3	797.7	15[F]	NS
[51]	SLM	M	AB	z	1095±10	990±5	8.1±0.3[F]	110±5
	SLM	M	AB*	z	1140±10	1040±10	8.2±0.3[F]	NS
[16]	DMLS	M	AB	z	1201	1088	10.6[F]	111
	DMLS	M	AB	xy	1248	1043	8.5[F]	112
[9]	SLM	AB	AB	z	1051±11	736±69	11.9±0.7[F]	109.9±11.3
	SLM	M	AB	z	1155±3	986±2	10.9±0.55[F]	112.4±4.6
[59]	SLM	P	AB	x	1321±6	1166±6	2.0±0.7[U]	NS
	SLM	P	SR	x	1225±4	1104±8	7.4±1.6[U]	NS
	SLM	P	SR	y	1214±24	1140±43	3.2±2.0[U]	NS
	SLM	P	SR	z	1256±9	1152±11	3.9±1.2[U]	NS
[60]	DMLS	M	AB	xy	1265±0.46	1098±2	9.4±0.46[F]	112±2
	DMLS	M	AB	xy	1170±6	1098±5	10.9±0.8[F]	117±2

Ref.	Process	Surface finish	HT	Build Orientation	UTS [MPa]	YS [MPa]	Elongation [%]	Young Modulus [GPa]
[75]	DMLS	AB	AB	z	1300*	1250*	4.0*[F]	NS
[64]	SLM	M	AB	z	1219±20	1143±30	4.89±0.6[F]	NS
	SLM	M	AB	xy	1269±9	1195±19	5±0.5[F]	NS
[48]	SLM	MP	SR	xy	1041	964	7[F]	NS
	SLM	MP	SR	z	1114	1058	3±2[F]	NS
[55]	SLM	MP	AB	xz	1143±6	978±5	11.8±0.5[F]	115±6
	SLM	MP	AB	z	1117±3	967±10	8.9±0.4[F]	119±7
	SLM	MP	AB	xy	1199±49	1075±25	7.6±0.5[F]	113±5
	SLM	MP	SR	xz	1057±8	958±6	12.4±0.7[F]	113±9
	SLM	MP	SR	zx	1052±11	937±9	9.6±0.9[F]	117±6
	SLM	MP	SR	xy	1065±21	974±7	7.0±0.5[F]	112±6
[67]	DMLS	M	AB	z	1238±8.9	1105±9.1	10.74±0.7[F]	109±1.5
	DMLS	M	SR	z	1171.6±6	1098±8.1	11.89±1[F]	115.8±1
[76]	SLM	M	AB	xy	1206±8	1137±20	7.6±2[F]	105±5
	SLM	M	AB	z	1166±25	962±47	1.7±0.3[F]	102±7
	SLM	M	SR	xy	1046±6	925±14	7.5±2[F]	98±3
	SLM	M	SR	z	1000±53	900±101	1.9±0.8[F]	110±29
[50]	SLM	M	AB	z	1267±5	1110±9	7.28±1.12	109.2±3.1

Ref.	Process	Surface finish	HT	Build Orientation	UTS [MPa]	YS [MPa]	Elongation [%]	Young Modulus [GPa]
[77]	DMLS	AB	SR	xy	1085±4	NS	6*[F]	NS
	DMLS	AB	SR	45°	1064±5	NS	5.5*[F]	NS
	DMLS	AB	SR	z	1040±11	NS	9.1*[F]	NS

Note: * estimated values deduced from graphs presented in the study. P-polished. M-Machined. AB-As Built. SR-Stress Relieved. [U]-uniform elongation. [F] – elongation at fracture, NS Not Specified.

In Table 7 a brief conclusion of various authors who investigated the issue regarding the mechanical properties of DMLS Ti6Al4V is presented.

Table 7: Brief conclusions of various authors

Ref.	Short conclusion
[73]	“Basket-weave microstructure with α lamellae. Samples tested in the xy build direction had higher strength and lower ductility.”
[54]	“Most commercial SLM processes achieve a near 100% density, and the material behaviour is directly related to its microstructure. DMLS produced parts may require a heat treatment process different from wrought materials.”
[74]	“DMLS technique produces Ti6Al4V component which has columnar grain with partial martensite structure and heat treatment reduced the UTS and also internal pores.”
[51]	“Mechanical properties of SLM Ti6Al4V strongly depends on microstructure. The as built material coming from the SLM process has a martensitic microstructure; the matrix is composed of acicular α -phase, while no β -phase is present.”
[16]	“Regarding the influence of the build orientation (horizontal vs. vertical), the results are inconclusive, with the horizontal values being somewhat higher for cylindrical and slightly lower for flat samples.”

[9]	“The tensile strength of SLM processed material without any heat treatment compared well with wrought Ti6Al4V, and machined components performed better with regards to fatigue properties but that’s not the case with regards tensile properties.”
[59]	“Ti6Al4V produces a complex microstructure and internal stresses and this causes the material to be anisotropic.”
[60]	“The results indicate that DMLS can meet the requirements of standards when process parameters are properly selected and the only post-processing necessary is stress-relieving.”
[75]	“DMLS samples delivered higher UTS and YS but lower elongation at break than wrought or cast Ti6Al4V samples.”
[64]	“SLM samples resulted in a martensitic microstructure with better surface finish than EBM and SLM process resulted in favourable mechanical properties for many applications.”
[48]	“The samples oriented in the transverse direction had higher yield strength and tensile strength than the longitudinal samples and, in both cases, lower ductility than wrought Ti6Al4V.”
[55]	“It was observed that the microstructure does indeed follow precise crystallographic rules and the layers solidify in the β phase field and precipitate as α' martensitic phase. The orientation of the prior β columnar grain boundaries has an influence on material properties and thus makes SLM orientation sensitive.”
[67]	“The effects of the orientation of primary β grain boundaries should be investigated in order to produce more reliable components with smaller cross-sectional areas.”
[76]	“The anisotropy remained prominent regardless of the heat treatment processes followed.”
[50]	“Heat treatment below the β transus temperature and then furnace cooled proved to be the optimal for an overall optimization of tensile properties.”
[77]	“Built orientations influences the dimensional accuracy as well as the surface roughness and in turn effects the mechanical properties.”

[78]	"The tensile properties of the laser-formed material were isotropic."
------	-----------------------------------------------------------------------

2.3.3 Mechanical testing

Tensile testing is a common method used to characterise the fundamental mechanical properties of engineering materials, either to verify or to develop new fundamental properties [16]. Mechanical tests include compression, bending, torsional and, the most common, the tensile test.

2.3.3.1 Standard metal tensile test

The literature recognises two main methods of testing DMLS material at room temperature, namely ISO 6892 and ASTM E8/E8M.

In [16], the proposed method of testing DMLS materials is in accordance with ISO 6892. A typical sample is presented in Figure 34. According to EOS, the reasons for selecting the geometry represented in Figure 34 as standard for DMLS are as follows:

- "Cylindrical sample geometry ensures a homogenous distribution of stress.
- Cylindrical sample geometry is easy and efficient to produce, and easier to post machine with high tolerances (if desired) compared to e.g. flat specimens.
- The results are also comparable to ASTM E 8M, because the dimensional guidelines correlate to ISO 6892, DIN EN 10002-1 and DIN 50125 by a factor of 0.8333.
- 5mm diameter provides better reliability of results (smaller is less reliable, 4mm is the smallest permitted by the standards) combined with cost-effective production (larger sizes mean longer build times and higher costs)."

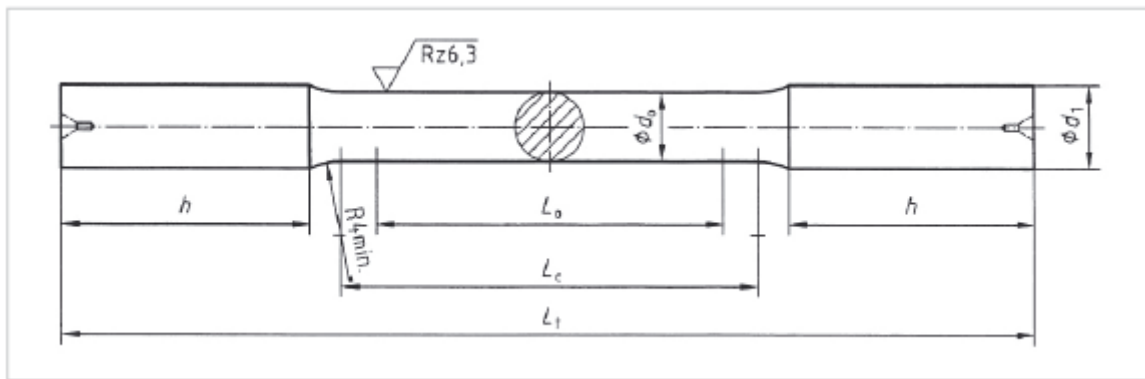
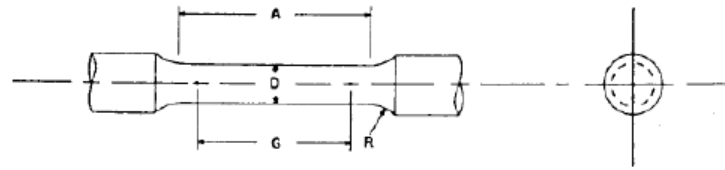


Figure 34: Recommended tensile test sample for DMLS according to ISO 6892 using $L_t=80\text{mm}$, $L_c=40\text{mm}$, $L_0=25\text{mm}$, $d_0=5\text{mm}$, $d_1=6\text{mm}$, $h=20\text{mm}$ [16]

In Figure 35, the typical dimensions of a standard 12.5-mm round tension test specimen and examples of small-sized specimens proportional to the standard specimen are represented. According to ASTM Standard E8 the standard specifications for round specimens are as follows:

- “Note 1: the reduced section may have a gradual taper from the ends toward the centre, with the ends not more than 1% larger in diameter than the centre (controlling dimension).
- Note 2: If desired, the length of the reduced section may be increased to accommodate an extensometer of any convenient gage length. Reference marks for the measurement of elongation should, nevertheless, be spaced at the indicated gage length.
- Note 3: The gage length and fillets may be as shown, but the ends may be of any form to fit the holders of the testing machine in such a way that the force shall be axial. If the ends are to be held in wedge grips it is desirable, if possible, to make the length of the grip section great enough to allow the specimen to extend into the grips a distance equal to two thirds or more of the length of the grips.
- Note 4: On the round specimens in Figure 34, the gage lengths are equal to four [E8] or five times [E8M] the nominal diameter. In some product specifications other specimens may be provided for, but unless the 4-to-1 [E8] or 5-to-1 [E8M] ratio is maintained within dimensional tolerances, the elongation values may not be comparable with those obtained from the standard test specimen.
- Note 5—The use of specimens smaller than 6-mm [0.250-in.] diameter shall be restricted to cases when the material to be tested is of insufficient size to obtain larger specimens or when all parties agree to their use for acceptance

testing. Smaller specimens require suitable equipment and greater skill in both machining and testing.”



Dimensions, mm [in.]					
For Test Specimens with Gauge Length Four Times the Diameter [E8]					
	Standard Specimen	Small-Size Specimens Proportional to Standard			
	Specimen 1	Specimen 2	Specimen 3	Specimen 4	Specimen 5
G—Gage length	50.0 ± 0.1 [2.000 ± 0.005]	36.0 ± 0.1 [1.400 ± 0.005]	24.0 ± 0.1 [1.000 ± 0.005]	16.0 ± 0.1 [0.640 ± 0.005]	10.0 ± 0.1 [0.450 ± 0.005]
D—Diameter (Note 1)	12.5 ± 0.2 [0.500 ± 0.010]	9.0 ± 0.1 [0.350 ± 0.007]	6.0 ± 0.1 [0.250 ± 0.005]	4.0 ± 0.1 [0.160 ± 0.003]	2.5 ± 0.1 [0.113 ± 0.002]
R—Radius of fillet, min	10 [0.375]	8 [0.25]	6 [0.188]	4 [0.156]	2 [0.094]
A—Length of reduced section, min (Note 2)	56 [2.25]	45 [1.75]	30 [1.25]	20 [0.75]	16 [0.625]

Figure 35: Typical dimensions of standard 12.5-mm round tension test specimen and examples of small-sized specimens proportional to the standard specimen [79]

Also recommended for the tensile tests of DMLS samples are the following:

1. “To indicate whether the specimens were machined or not, building direction, post-stress relieving.
2. To test both horizontal and vertical samples.
3. As with all manufacturing methods, it should be kept in mind that the mechanical behaviour of real three-dimensional parts is not only determined by the bulk material properties, but also by surface roughness and other geometric effects, such as stress-concentrations at corners. This is especially relevant for fatigue behaviour”.

2.4 Topology Optimization

Topology describes mathematically the geometric continuity and connectivity of a material space or domain. A simple polyhedron is one of the basic entities in the study of topology, and if it were fabricated with a rubber-like substance, a polyhedron could be deformed to a sphere by twisting, bending or compressing but without tearing, puncturing or fusing [80]. The Euler characteristic is used to describe the topological property of an object and is typically calculated as the sum of the vertices and faces minus the sum of the edges. Furthermore, according to the Euler characteristic, as described by Mortenson, all simple polyhedral structures like plates, bolts and bowls are topological equivalents. Topologically complex objects are then derived from simple topologically

non-equivalent parent objects by introducing discontinuities or holes via discontinuous deformations like tearing or fusing of surfaces. Examples of the phenomenon are displayed in Figure 36, from which it can be seen that the shape or dimensions of an object, both interior and exterior surfaces, can be alternated without alternating its topology, and in order to obtain a topological transformation additional discontinuities must be introduced in the object. It is therefore clear that the ability to characterise a physical object or virtual design for both topological and continuous properties, like shape and dimensions, is required.

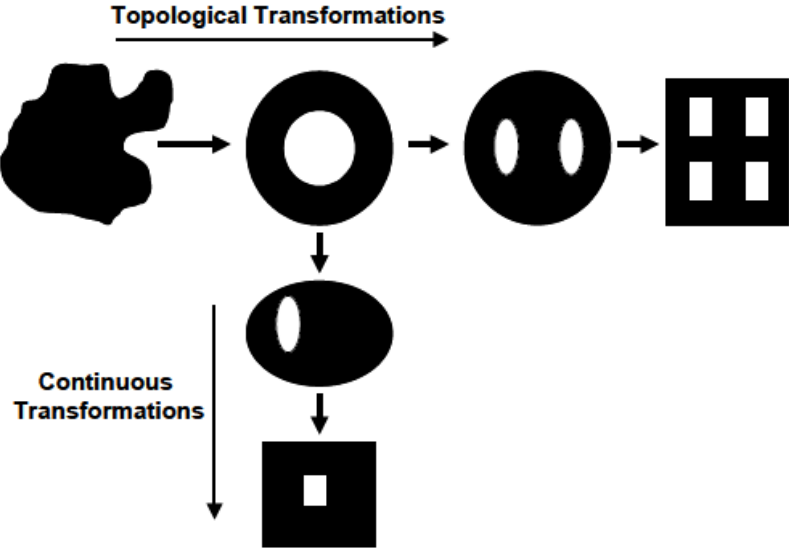


Figure 36: Continuous and topological transformations of a simple object [81]

Structural optimization can be described as the assemblage of material that can best sustain the specified conditions [82]. Christensen et.al. [82] explain the method of structural optimization to obtain certain outcomes like minimising weight or maximising stiffness as follows:

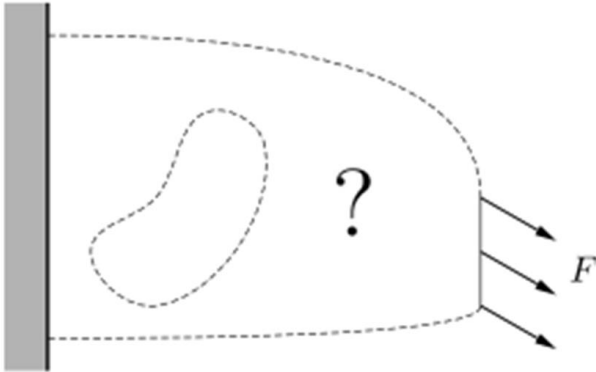


Figure 37: Structural optimization problem [82]

By referring to Figure 37, the optimization can be defined as the process of finding the best possible manner to minimise or maximise the objective function in a design domain; this is done to ensure that the forces (F) applied are transmitted to the support and keep the constraints in check. To formulate:

$$\text{Minimize } f(x)$$

$$\text{Subject to } \begin{cases} g(x) \leq 0 \text{ for } i = 1, 2, \dots, l \\ h(x) \leq 0 \text{ for } j = 1, 2, \dots, m \end{cases}$$

In this case, x is the design variable belonging to a domain Ω , and constraint functions are $g(x)$ and $h(x)$, respectively [82]. Structural optimization can be divided into size-, shape- and topology optimization as displayed in Figure 38. In size-optimization, the design variables are the parameters that dictate the structure's size. These variables are involved in calculating the optimal plate thickness, and the fixed variables include the connectivity and shape of the elements. During the process of shape-optimization, the design variables represent the shape or contour of the domain; thus, only the shape of the holes change. However, during topology optimization, the algorithm aims to determine the number, location, shape and connectivity in the design domain [2].

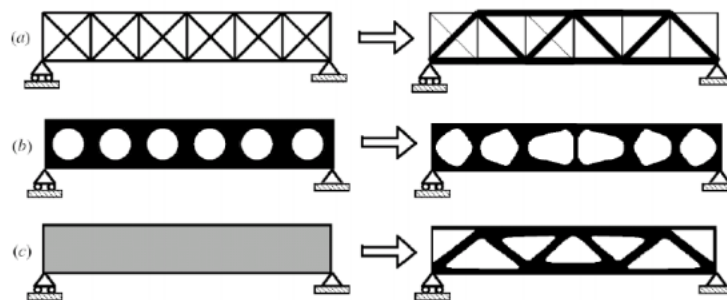


Figure 38: Examples of (a) size optimization, (b) shape optimization and (c) Topology Optimization [2]

Competitive pressure in the industry and the depletion of natural resources force engineers to seek designs closer to the optimum material usage through diverse optimization algorithm approaches. The advantage of incorporating topology optimization into the design process is that it leads to improved designs, and the use of topology optimization in many industries is expanding. Optimization in a greater perspective can be applied to many fields, for example:

- Design of prosthetic leg for **minimum weight**
- Optimum design of a truss for **maximum stiffness**
- Design of a walkway to maximum the **lowest natural frequency**
- Design of heat exchanger systems to **maximise the heat transfer**.

The field of topology optimization has been extensively researched over the years and a few different algorithms have been developed, such as the ground structure approach, homogenisation [83], solid isotropic material with penalisation (SIMP) [84, 85], bi-directional evolutionary structural optimization [86] and genetic algorithms [87]. A brief overview of the SIMP approach is presented since this is the approach the software used for the topology optimization.

The SIMP method was originally presented by Bendsoe in the 1980s [88, 89]. The SIMP method is also referred to as the power law method, the artificial density method or the direct approach method. This method is based on the principle of keeping a fixed finite element discretisation and associates a density function $\rho(x)$ with values between 1 (solid) and 0 (void) to each finite element. Rosvany et al. [90] discuss the intermediate values to a sort of artificial material that can be interpreted as porous or a type of mesostructure containing holes. The final design solution is thus made up of black regions (or solid regions), grey regions (or intermediate porous) and white regions (or voids). Since these intermediate regions are impractical, several design filters are introduced to eliminate them and a review is available in the book by Bendsoe et al. [2]. A complete review is presented in the study done by Rozvany [91]; this includes terminology, history and aim.

From the literature [92–97], the following advantages were obtained and thus give the SIMP method the upper-hand in popularity:

- “The simple parameterization technique is easily implemented
- The method has been thoroughly studied over the years and can thus be applied to problems with complicated conditions
- The method uses only one design parameter (density) for each element and thus the computational effort is minimized as well as storage needed to perform the optimization.”

The one concern regarding the SIMP method is the inaccurate estimation of the material properties for the mesostructures as well as the difficulty of manufacturing. This concern can be eliminated by raising the intermediate densities to a higher ‘ p -value’. By doing this, both the inaccuracy of the parameterisation model at intermediate densities and the difficulty of fabricating those intermediate densities with conventional non-additive manufacturing processes are eliminated [97]. This is discussed by Allaire, who points out the importance of choice in the penalisation parameter [98].

In general, the SIMP procedure is described in Figure 39:

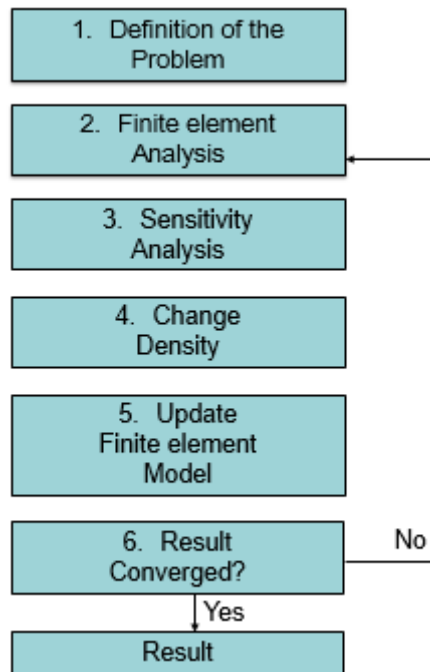


Figure 39: SIMP procedure [92]

As previously discussed, this process is based on the power law method. The first step of the SIMP process is defining the problem; this includes the desired design domain with fixed boundary conditions, as illustrated in Figure 40.

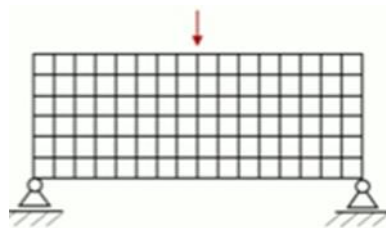


Figure 40: Definition of the problem [99]

The next step would be to perform a finite element analysis on the defined problem without alternating the design domain, but since this is an iterative process, the model is updated for each iteration, and the finite element analysis step is displayed in Figure 41.

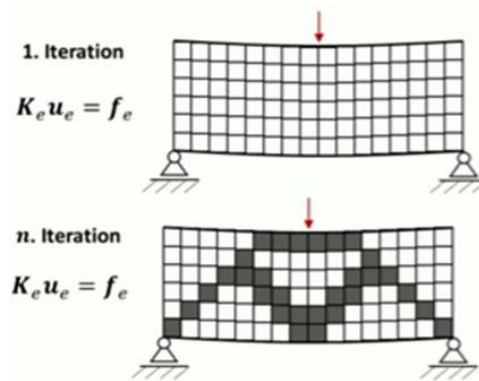


Figure 41: Finite element analysis [99]

Before the model is updated, a sensitivity analysis is performed to determine the densities assigned to each element, as displayed in Figure 42. Each element in the design domain is associated with a function called density, and this value varies between 0 and 1. The objective of the program is to determine the density function that would resemble optimal material distribution. The density of 0 and 1 can be viewed as void and solid material, respectively, and values between 0 and 1 as grey regions. Then the white regions are penalised and, depending on the penalisation factor, the grey regions are also penalised.

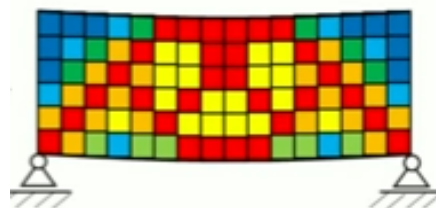


Figure 42: Sensitivity analysis [99]

Once the densities for each element are determined and assigned, they are then updated, as displayed in Figure 43.

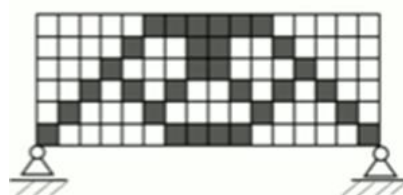


Figure 43: Changed density [99]

The FEM is then updated, and a conclusion is drawn on whether the results converged or not. If the results converged, a model is obtained for further analysis and refinement. Figure 44 represents an example of the SIMP approach.

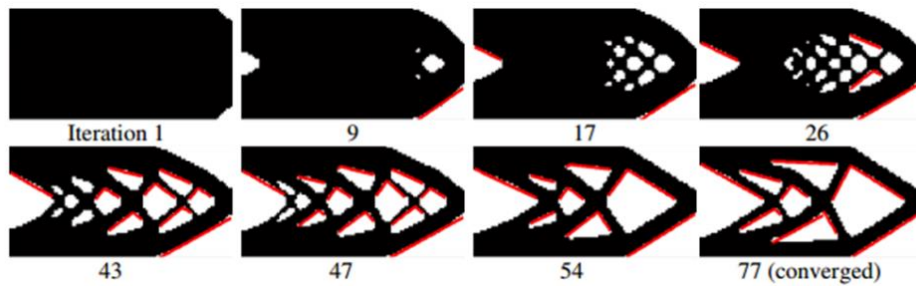


Figure 44: Typical example of the SIMP approach [2]

2.4.1 Topology Optimization software

In this study, different topology optimization softwares are investigated and discussed.

The programming platform MATLAB® is used to code efficient topology optimization algorithms [100–102]. Over the past few years, extensive research has gone into topology optimization and MATLAB® became an effective platform for testing these new developing algorithms [87, 93, 96, 97, 103–108]. The one major drawback from performing an optimization within MATLAB® is the post optimization processing and the geometry obtained from the optimization performed in MATLAB® which must be exported in the form of an STL into a CAD software in order to perform post optimization processes.

The method of topology optimization in both NX™ and solidThinking Inspire™ are based on the SIMP method [109, 110]. However, the solutions obtained when given the same case study are different due to the intensive development of topology optimization constraints and filters over the past several years [2, 6, 85, 93, 97, 98, 100–102, 104–106, 111–114] as well as the different finite elements used. The finite elements used during any finite element analysis are fundamental since the elements represent the geometry of the structure completely [109]. It is thus naïve to expect to obtain the same topology optimized results with two different optimization software packages.

Extensive research and evaluation have been done on topology optimization within solidThinking Inspire™ [7, 115–121]. Therefore, this proves solidThinking Inspire™ to be a reliable optimization software.

2.5 Finite element analysis

FEA is commonly used to verify CAD designs [122]. In this dissertation, the author aims to exploit the validity of FEA on topology optimized DMLS structures. FEA is used to verify a CAD model to identify possible weaknesses and limitations before a model is manufactured and validated. FEM is a numerical method governed by differential or integral equations and is used to solve physical

problems that are nearly impossible to solve routinely [123]. In this dissertation, a linear, static analysis is performed, and the following assumptions are made according to NX™ online help forum [110]:

“Static assumption

- The loads are applied gradually until they reach their full magnitudes
- After the loads reached their full magnitude, they remain constant and thus invariant of time
- Inertial and damping forces are neglected due to the negligibly small accelerations and velocities.

Linearity assumptions

- The relationship between loads and induced responses is linear.

The linear static analysis is thus only valid when:

- All materials in the model comply with Hooke’s law
- The induced displacements are small enough to ignore the change in stiffness caused by loading
- Boundary conditions do not vary during the application of loads”.

2.5.1 FEA and metal AM

In almost all engineering disciplines, FEM has proven to be a viable tool for solving boundary, initial and eigenvalue problems [124]. According to Schoinochoritis et al. [125] , FEM has proven to be an essential tool when it comes to the physical study of AM processes and their parametric optimization since FEM is a resource-efficient methodology that saves on physical experiments. Schoinochoritis et al. [125] then claim FEM to be the most common technique for predicting the residual stresses, porosity and distortion of parts produced by AM processes. However, to predict the mechanical performance of parts produced by AM, the powerful numerical tool of FEA must be used, since FEA can save money and time when compared to conducting physical experiments. Schoinochoritis et al. [125] concluded that the simulation of AM is lacking due the great diversity in the modelling of the properties as well as the limited understanding of the physics of the process. However, it is essential that simulation forms part of the processing chain to ensure safe components.

In a study, Dzogbewu used FEA to predict the von Mises stresses and true strain. This was done to compare Ti6Al4V to human bone and to experiment with different designs before the final product was produced. The author concluded FEA to be a valuable tool for predicting the behaviour under a static load of advanced lightweight DMLS implants [126]. According to Lunbäck et al. [127], the sustainability of AM structures increases when modelling and simulation are included in the development of the product.

A linear static analysis was performed by Brusa et al. [128] to validate the complex AM component and demonstrated that FEA can be effective in predicting the material and component strength when statically loaded. Monaheng [129] reached the same conclusion in her dissertation.

Abdi used the FEA to obtain the stiffness and the equivalent von Mises stresses in order to compare different designs [130]. In a similar fashion, the FEA was used to validate the DMLS topology optimized components by other researchers [119], [120], [121].

2.5.2 Validation of FEA

The FEA has proven in many cases to be a powerful tool for predicting the mechanical behaviour of complex structures under tension. To build confidence in the FEA of a specific case study, the simulation results should be validated by comparing them to experimental results. Throughout the literature, two types of experimental validation are observed by either comparing the simulation results against experimentally obtained strain gauge or digital image correlation (DIC) results. Validating FEA has proven to be successful with strain gauge measurements [129] and DIC [121]. However, since the aim of this dissertation was to capture the nature of the complexity, DIC was concluded as a preferred means of validating the FEA results obtained.

2.6 Conclusion

A brief summary of the conclusions drawn from the in-depth literature review is provided:

1. Numerous factors influence the quality of a DMLS component, as illustrated in Figure 5
2. When the process parameters are kept at near optimum and constant values, the most influential attributes of the mechanical properties are:
 - Microstructure
 - Geometry
 - Surface finish
 - Build orientation
 - Residual stresses

- Porosity.
3. Residual stress can successfully be reduced within components by heat treatment without alternating much of the microstructure of as-built DMLS Ti6Al4V parts.
 4. From Table 7 the conclusion is clear that there is a necessity to test the mechanical properties of the specific samples printed on a specific machine to either confirm the mechanical properties in Table 6 or create its own database.
 5. Two main standards are used throughout the literature to determine the mechanical properties of DMLS material:
 - ISO 6892
 - ASTM E8/E8M
 6. solidThinking Inspire™ uses the SIMP method for topology optimization.
 7. From the literature it is clear that solidThinking Inspire™ is a trusted optimization software and thus the preferred optimization software for this dissertation.
 8. The FEA results will be influenced by the assumptions made for linear static analysis. The FEA results would further be influenced by the size of the elements and type of element used.
 9. Throughout the literature, FEA is used to verify designs.
 10. Experimental procedures are used to validate FEA.

3.1 Introduction

This chapter focusses on the theory behind the tensile stress and provides the reader with the basic principles of FEM in order to understand the difference between simulation results, hand calculations and practically obtained results. This chapter also strives to provide a firm understanding of von Mises stress and how to determine it from strain rosettes.

3.2 Tensile test

The tensile test is a method where stresses are applied to the sample in defined intervals, and the material's response is recorded in terms of strain. Figure 47 represents a typical stress-strain diagram.

During the tensile test, the material initially undergoes elastic deformation followed by plastic deformation. Elastic deformation is when a material returns to its original position once the uniaxial tensile force subjected to the material is removed. During elastic deformation, the material's atoms are displaced from their original positions but not to the extent that they take up new positions, thus when the uniaxial force is removed the atoms return to their original positions as does the material. On the other hand, with plastic deformation, the material's atoms are permanently displaced from their original positions and, therefore, the material deforms plastically [31].

In order to form a conclusion from the mechanical properties of a material, regardless of geometry, the engineering stress and strain are thus used. From Figure 45, the engineering stress (σ) on the bar can be described as being equal to the average uniaxial tensile force F on the bar divided by the original cross-sectional area A_0 of the bar [31]. Therefore,

$$\text{Engineering stress } \sigma = \frac{F(\text{average uniaxial tensile force})}{A_0(\text{original cross - sectional area})} \quad (4)$$

Engineering strain can be described as seen in Figure 45. Strain occurs when a uniaxial tensile force is applied to a rod such as that it causes the rod to elongate in the direction of the applied force. Thus, by definition, engineering strain is the ratio of the change in length of the sample in the direction of the force to the original length of the sample considered. The engineering strain is therefore dimensionless; it is common to convert these dimensionless entities to a strain or elongation percentage [31]. Hence, the obtained equation:

$$\text{Engineering strain } \varepsilon = \frac{\Delta l(\text{change in length of sample})}{l_0(\text{original length of sample})} \quad (5)$$

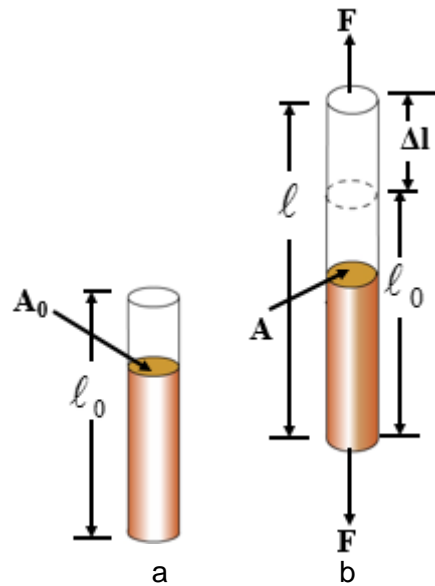


Figure 45: Elongation of a cylindrical metal rod subjected to a uniaxial tensile force F . a) The rod with no force applied on it; b) the rod subjected to the force F , which elongates the rod from length l_0 to l .

When a longitudinal tensile force applied to a material and an elastic deformation in the force's direction occurs, it produces an accompanying lateral dimensional change as displayed in Figure 46. Poisson's ratio is thus the ratio of lateral deformation to longitudinal deformation [31]. Hence, equation 6 follows:

$$\nu = -\frac{\varepsilon(\text{lateral})}{\varepsilon(\text{longitudinal})} \quad (6)$$

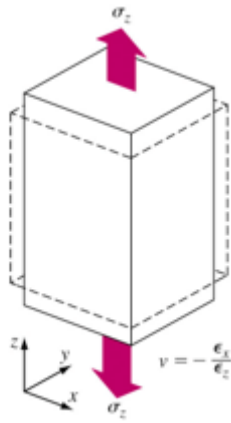


Figure 46: Cubic body subjected to tensile stress.

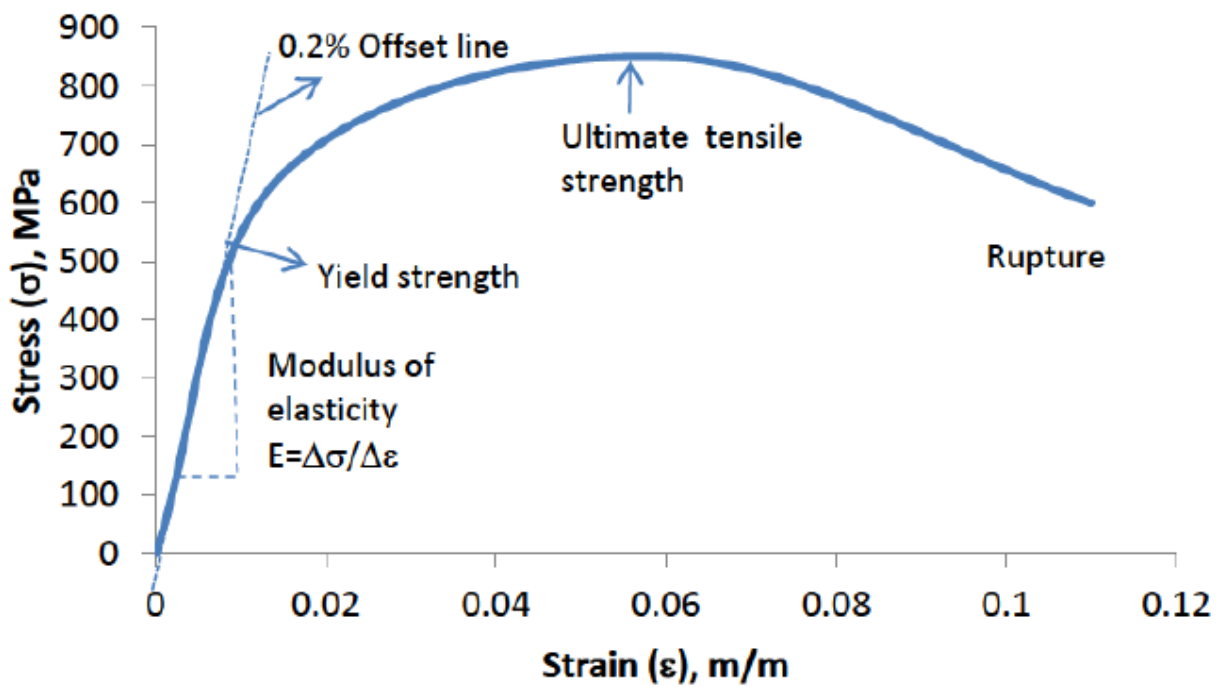


Figure 47: Typical stress-strain diagram [131]

The typical properties obtained from a stress-strain curve is as follows:

- **Modulus of elasticity**

During the initial phase of the tensile test, the material undergoes uniform Elastic deformation. This linear relationship between stress and strain is called modulus of elasticity and is described by Hook's law:

$$E(\text{modulus of elasticity}) = \frac{\sigma(\text{stress})}{\varepsilon(\text{strain})} \quad (7)$$

- **Yield strength at a 0.2-percent offset**

The yield strength is the very critical point where the elastic region of the material ends and the plastic region begins. Since this point is almost impossible to determine due to the dependence on equipment sensitivity [132], it is chosen as the strength for a definite amount of plastic strain. For American engineering structural design, the yield point is chosen where 0.2 percent plastic strain has taken place. The construction line begins at 0.2 percent strain and is parallel to the elastic region, as displayed in Figure 48.

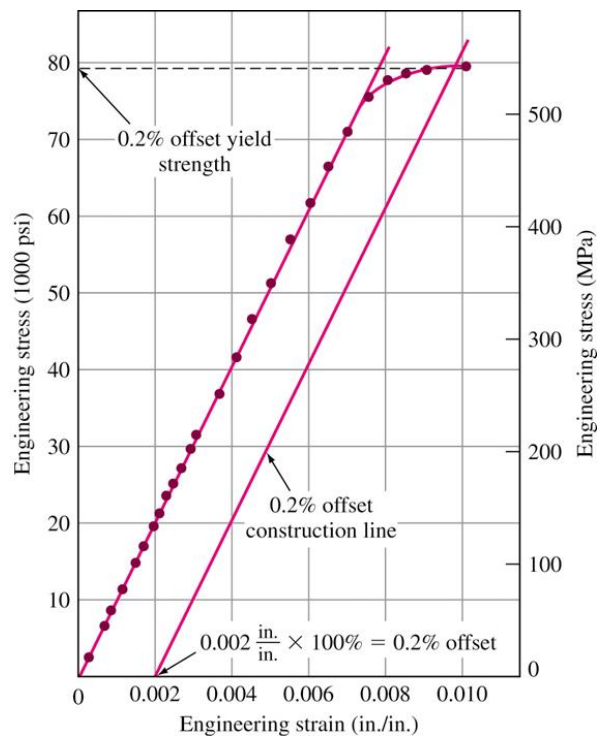


Figure 48: Linear part of an engineering stress-strain curve [31]

- **Ultimate tensile strength**

Ultimate tensile strength (UTS) is the maximum strength reached by the engineering stress-strain curve after the ultimate stress necking has begun to occur, which is a localised decrease in cross-sectional area, as illustrated in Figure 49. Note that engineering stress does not consider the phenomenon necking.

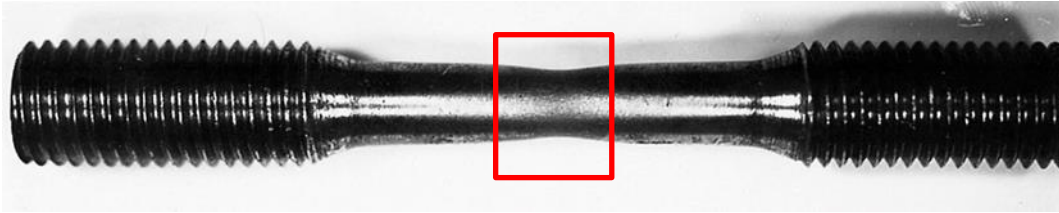


Figure 49: An illustration of necking [31]

3.3 Basic principles of FEM

The basics principles of FEM are discussed in the following section, based on the handbook The finite element method in engineering [133]. According to the author, FEM follows an orderly step-by-step process, with the first step being the discretisation of the continuum or dividing the complex problem into smaller manageable elements. This division of a region into finite elements includes scalar parameters, coordinates of nodal points, material properties, array of element types, array for the description of displacement boundary conditions, connectivity array of finite elements and array for the description of surfaces and point loads. The next step is defining an equation for each of the smaller elements derived from the discretisation of the continuum. All the elements are then added together to create a mesh and form a combined equation. The boundary conditions are then applied to some of the elements, after which the results are calculated for every element, taking into account the results on adjacent elements. In order to understand how FEM works, an example is presented.

The example begins consisting of one element and two nodes as presented in Figure 50. The element has a given stiffness of k . The assumption is made that the deflection of the element is linearly proportional to the applied force and the value of k is thus constant. The element is given a single degree of freedom; thus, the element can only translate linearly, as indicated in Figure 51.

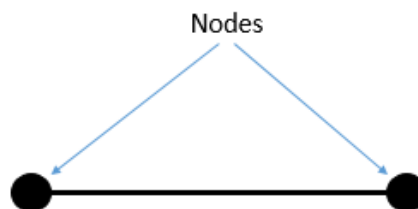


Figure 50: Single element [134]

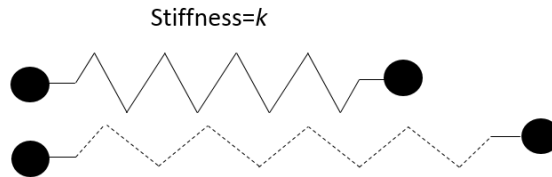


Figure 51: Single degree of freedom [134]

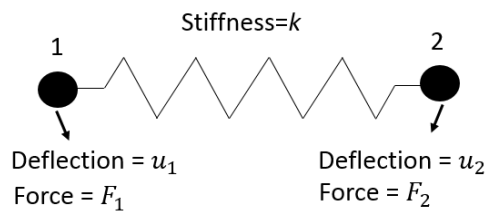


Figure 52: Defining the nodes [134]

The first step would be to calculate the individual stiffness of a typical element. At node 1 in Figure 52:

$$F_1 = k * \{u_1 - u_2\} \quad (8)$$

For static equilibrium:

$$F_1 - F_2 = 0$$

Then at node 2:

$$F_2 = -k * \{u_1 - u_2\} \quad (9)$$

When rewriting equation 8 and 9 in matrix form:

$$\begin{bmatrix} F_1 \\ F_2 \end{bmatrix} = \begin{bmatrix} k & -k \\ -k & k \end{bmatrix} * \begin{bmatrix} u_1 \\ u_2 \end{bmatrix}$$

With:

$$\begin{bmatrix} F_1 \\ F_2 \end{bmatrix} = [F] = \text{Force matrix for one element}$$

$$\begin{bmatrix} k & -k \\ -k & k \end{bmatrix} = [k] = \text{Stiffness matrix for one element}$$

$$\begin{bmatrix} u_1 \\ u_2 \end{bmatrix} = [u] = \text{Deflection matrix for one element}$$

A second element is added to the equation as in Figure 53 so that there are now two elements and three nodes; this is called a three-degrees-of-freedom problem and is used to describe the size of the problem.

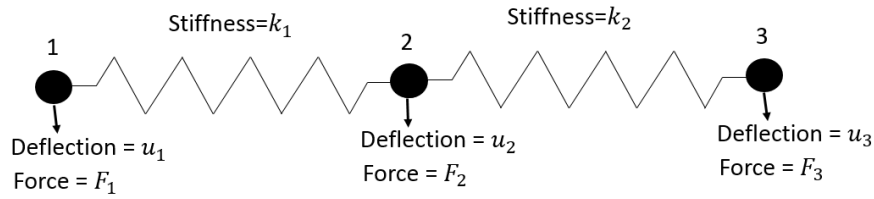


Figure 53: Second element added to equation [134]

The stiffness matrix is rewritten for the three nodes:

$$\begin{bmatrix} F_1 \\ F_2 \\ F_3 \end{bmatrix} = \begin{bmatrix} k_1 & -k_1 & 0 \\ -k_1 & (k_1 + k_2) & -k_2 \\ 0 & -k_2 & k_2 \end{bmatrix} * \begin{bmatrix} u_1 \\ u_2 \\ u_3 \end{bmatrix}$$

Now the boundary conditions are added as displayed in Figure 54.

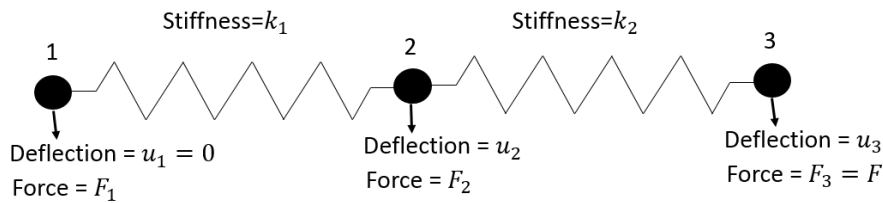


Figure 54: Applied boundary conditions [134]

$$\begin{bmatrix} F_1 \\ F_2 \\ F \end{bmatrix} = \begin{bmatrix} k_1 & -k_1 & 0 \\ -k_1 & (k_1 + k_2) & -k_2 \\ 0 & -k_2 & k_2 \end{bmatrix} * \begin{bmatrix} 0 \\ u_2 \\ u_3 \end{bmatrix}$$

$$F_1 = (k_1 * 0) + (-k_1 * u_2) + (0 * u_3) = -k_1 u_2$$

$$F_2 = (-k_1 * 0) + ((k_1 + k_2) * u_2) + (-k_2 * u_3) = (k_1 + k_2)u_2 - k_2 u_3$$

$$F = (0 * 0) + (-k_2 * u_2) + (k_2 * u_3) = -k_2 u_2 + k_2 u_3$$

$F_2 = 0$ since it is an internal force. Then:

$$u_2 = \frac{F}{k_1}$$

$$u_3 = F + k_2 \frac{F}{k_1}$$

For more complex problems, the general linear equation (equation 10) must be solved. This numerical method is suitable for computer solutions.

$$[F] = [k] * [u], \quad (10)$$

with the inverse matrix of $k = [k]^{-1}$, and multiplying the inverse matrix with equation 10 yields the following equation:

$$[k]^{-1} * [F] = [u]$$

With

$$[k]^{-1} = \frac{1}{det} * [k]^T,$$

and where:

det =determinant of k

$[k]^T$ =transpose matrix of k

Thus,

$$[u] = \frac{1}{det} * [k]^T * [F].$$

If this equation is applied to the same example as in Figure 54, the same results for u_2 and u_3 are obtained. Therefore, this method is used to solve large stiffness matrices.

3.4 Von Mises stress

The von Mises stress is a value used to describe the stress that a material experiences under complex loading conditions [110]. With principal plane stress, the von Mises stress is described by the following equation:

$$\sigma_v = \sqrt{\sigma^2_1 - \sigma_1\sigma_2 + \sigma^2_2 + 3\tau_{12}^2}$$

With σ_1 and σ_2 being the principal stresses and the corresponding planes on which they act are called principal planes of stresses.

The principal stresses are defined as follows:

$$\sigma_{1,2} = \frac{\sigma_x + \sigma_y}{2} \pm \sqrt{\left(\frac{\sigma_x - \sigma_y}{2}\right)^2 + \tau_{xy}^2}$$

However, no shear stress acts on the principal planes; therefore, von Mises stress is:

$$\sigma_v = \sqrt{\sigma_1^2 - \sigma_1\sigma_2 + \sigma_2^2}$$

3.5 Strain rosette

Strain rosette is used to specify the state of strain of a point on a free surface. A strain rosette is a cluster of strain gauges arranged in a specific pattern. In general, the cluster consists of three strain gauges arranged at specific angles, as displayed in Figure 55.

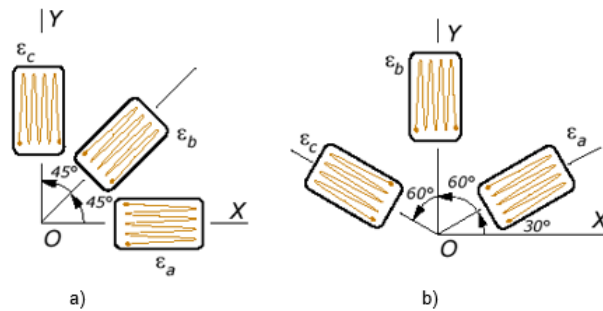


Figure 55: a) 45° strain rosette, b) 60° strain rosette [135]

When the readings $\epsilon_a, \epsilon_b, \epsilon_c$ are taken and $\theta_a, \theta_b, \theta_c$ known the strain components $\epsilon_x, \epsilon_y, \gamma_{xy}$ can be determined by solving the following equations:

$$\epsilon_a = \epsilon_x \cos^2 \theta_a + \epsilon_y \sin^2 \theta_a + \gamma_{xy} \sin \theta_a \cos \theta_a$$

$$\epsilon_b = \epsilon_x \cos^2 \theta_b + \epsilon_y \sin^2 \theta_b + \gamma_{xy} \sin \theta_b \cos \theta_b$$

$$\epsilon_c = \epsilon_x \cos^2 \theta_c + \epsilon_y \sin^2 \theta_c + \gamma_{xy} \sin \theta_c \cos \theta_c$$

Once $\epsilon_x, \epsilon_y, \gamma_{xy}$ are determined, the transformation equations of Mohr's circle can be used to determine the maximum in-plane shear strain and principal in-plane strains at that point.

3.6 Conclusion

During the chapter the theory behind the tensile stress was discussed in order to enlighten the reader of certain aspects discussed later in this dissertation. The basic principles of FEM are

explained to be able to understand the difference between simulation results, hand calculations and practically obtained results. This chapter strived to provide a firm understanding of von Mises stress and how to determine it from strain rosettes.

4.1 Introduction

This chapter focusses on developing a topology optimized model by using the background obtained from the literature review. In order to develop the model, the material properties must be obtained. Hence, the design space is determined and the loads calculated.

4.2 Mechanical properties of DMLS Ti6Al4V

The DMLS samples used to determine the mechanical properties of Ti6Al4V are manufactured and tested according to ISO 6892. The Ti6Al4V sample is printed in an argon-protected atmosphere by the EOSINT M280 machine (EOS GmbH) equipped with an ytterbium-fibre laser operating at a wavelength of 1075 nm at the CRPM facility. The laser-beam had a TEM00 Gaussian profile with 80 μm spot diameter, and the build volume rate was 1.2 mm^3/s with a powder layer thickness of 30 μm . A zigzag scanning by stripes strategy was followed with changing scanning angle of 67° from layer to layer, and the strip's hatch distance is 100 μm . The laser output power is 170 W. The recommended EOS process parameters and strategy were followed. The printed specimens are removed from the printer attached to the build platform and stress relieved in argon atmosphere at 650°C for three hours before removing from the build platform. A chemical composition of the employed powder is displayed in Table 8.

Table 8: Chemical composition of Ti6Al4V powder (in weight %)

Ti	Al	V	O	N	H	Fe	C
ASTM standard Ti grade 23							
88.1-91	5.5-6.5	3.5-4.5	≤0.13	≤0.03	≤0.0125	≤0.25	≤0.08
Employed powder							
89.13	6.26	4.1	0.09	0.01	0.002	0.20	0.01

The dimensions of the samples are displayed in Figure 56 and based on ISO 6892 and the suggested dimensions from EOS [16].

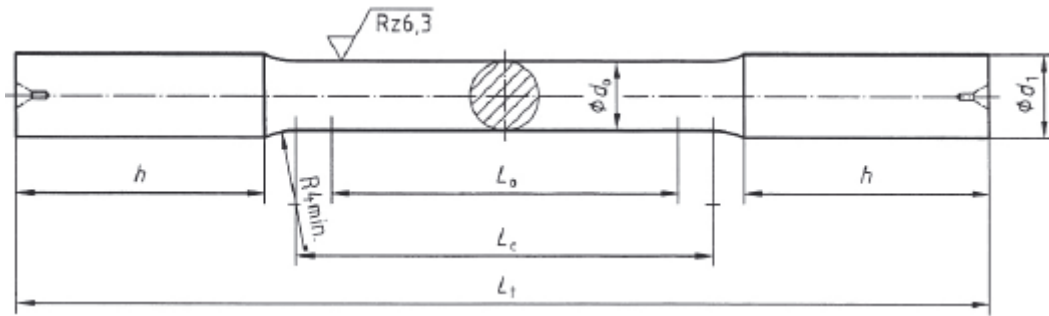


Figure 56: Geometry of DMLS tensile samples [16]

With:

- $L_t = 80 \text{ mm}$
- $L_c = 40 \text{ mm}$
- $L_o = 25 \text{ mm}$
- $d_o = 5 \text{ mm}$
- $d_1 = 6 \text{ mm}$
- $h = 20 \text{ mm}$.

The reason for this specific geometry is, according to EOS, as follows:

- “The cylindrical geometry of the samples ensures a homogenous distribution of stress
- It is easier to manufacture and post-machine (if desired) of cylindrical samples compared to e.g. flat samples
- The results are comparable to ASTM 8M-04
- 50-mm diameter provides reliable results and is cost-effective.”

The mechanical testing of the samples according to ISO 6892-1:2009 (Metallic materials – Tensile testing, Part 1: Method of test at room temperature) [136] was done on the MTS Landmark 370.10 (actuator integral to base) machine with an extensometer as displayed in Figure 58. Table 9 provides specifications and Figure 57 offers a description of the MTS Landmark 370.10. The machine was calibrated by IMP Calibration Services (Pty) Ltd and the calibration certificate number is NHQ-70401A.

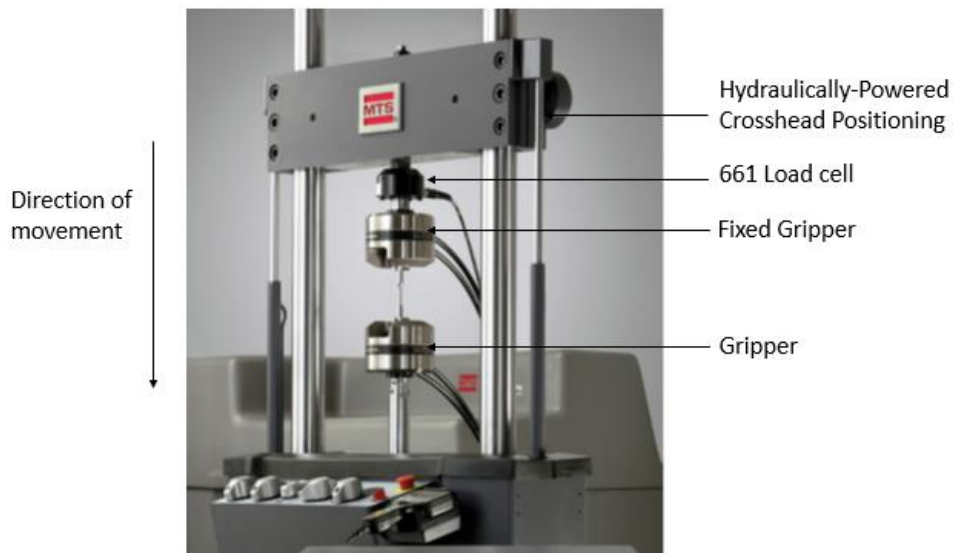


Figure 57: MTS Landmark 370.10 description



Figure 58: Mechanical testing of samples

Table 9: MTS Landmark 370.10 specifications [137]

Load frame specifications	Value	Unit
Dynamic force capacity	100	kN
Available nominal actuator rating	100	kN
Actuator dynamic stroke	150	mm
Standard vertical test space	140-1283	mm
Extended vertical test space	363-1753	mm
Stiffness	467×10^6	N/m

In order to test the anisotropy of the material, differently orientated samples were printed, as displayed in Figure 59.

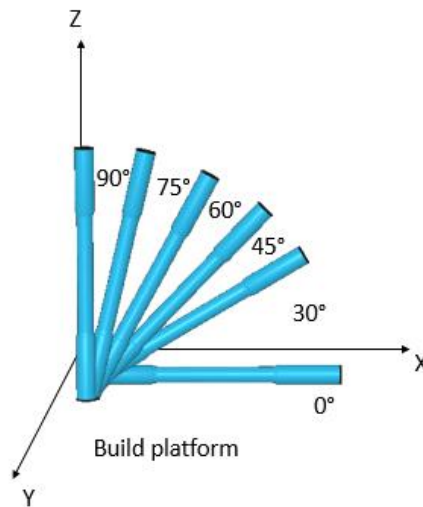


Figure 59: Sample orientation

The dimensions of the samples printed in the 0° and 90° print orientation are displayed in Figure 60. These samples were also tested in accordance with ISO 6892-1:2009 (Metallic materials – Tensile testing, Part 1: Method of test at room temperature) [136].

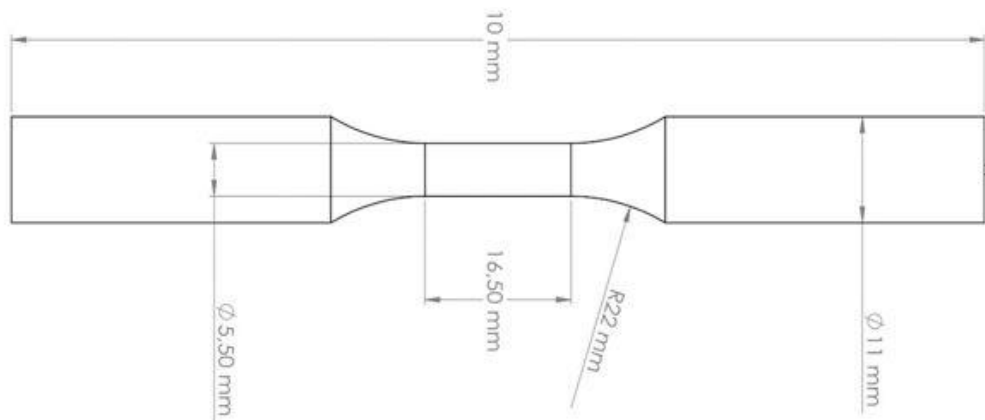


Figure 60: ASTM E606 test specimen [138]

As mentioned under the section **Yield strength**, it is nearly impossible to determine the exact yield point, hence the 0.2-percent offset yield is used. This is obtained by determining the slope of the linear elastic region of the stress-strain graph (Figure 61); this slope is also the modulus of elasticity (E). In Figure 62, a linear trend line is used to determine the slope, and by referring to the R^2 coefficient of determination (0.99972), it is clear that the trend line is a good representation of the linear region.

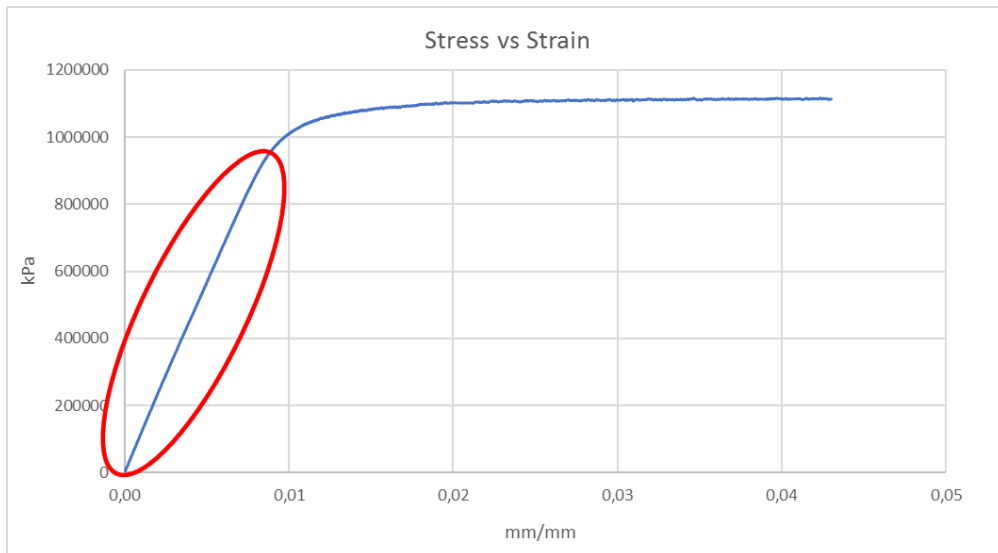


Figure 61: Determining the linear elastic region of a stress-strain graph

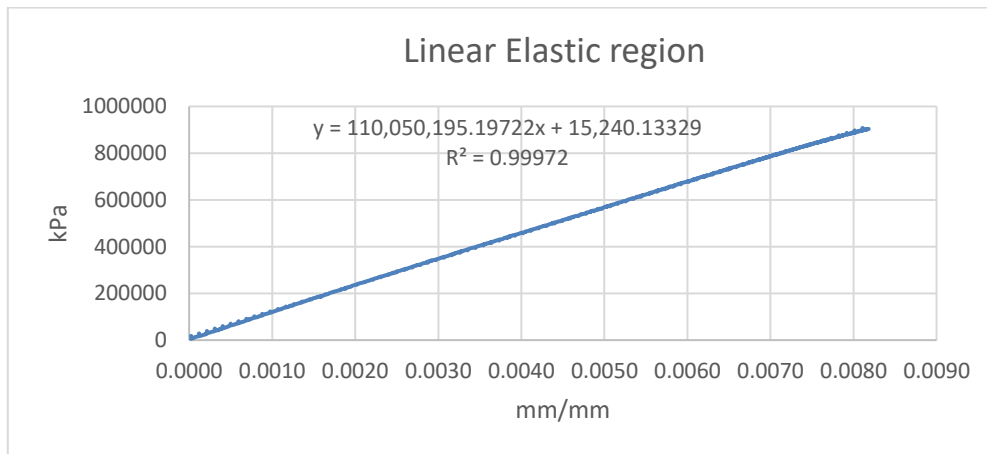


Figure 62: Linear elastic region

The 0.2-percent offset linear elastic region is then applied on the stress-strain graph. The point where the two graphs intersect is then considered to be the 0.2-percent offset yield point, as displayed in Figure 63.

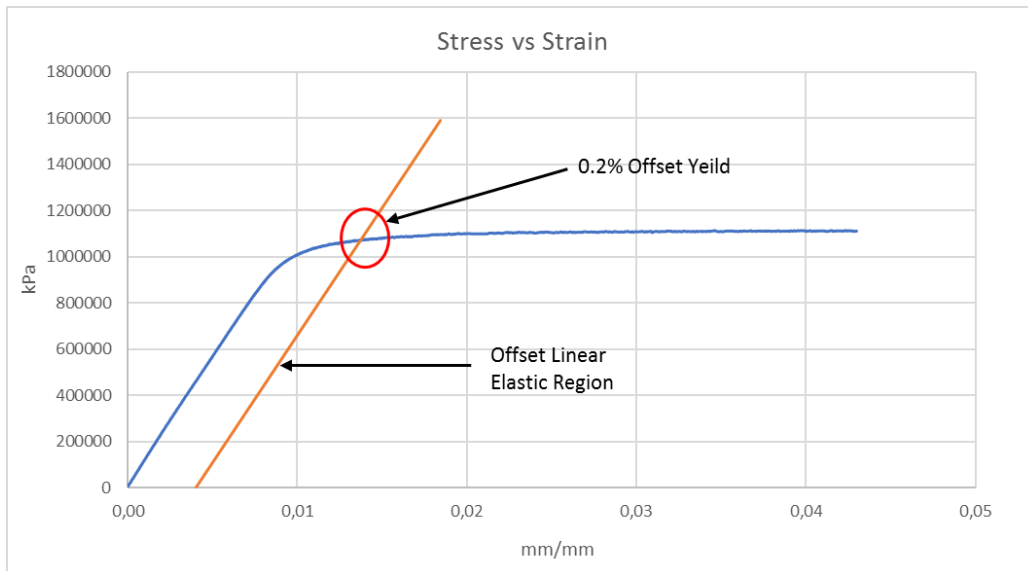


Figure 63: Determining 0.2% Offset Yield

A typical test result of the stress-strain curve is displayed in Figure 64, and all the results are displayed in APPENDIX B. The weakest coefficient of variance is 4.43 percent, as presented in APPENDIX B, which means these tensile tests are highly repeatable and thus contributes to the confidence in the results. Please note that all the tests were stopped after the UTS had been reached in order to protect the extensometer from damage. Also note that stress is calculated using the measured values of the diameter.

In Figure 64 depicts the proportional relationship between stress and strain, which can clearly be observed up to the proportional limit, point A, on the graph. This linear behaviour is a good indication of properly produced samples without defects or abnormalities. This stress-strain relationship is known as Hooke's Law, and in this region, the slope of the stress-strain curve is also the modulus of elasticity (E). The modulus of elasticity for the tensile test represented in Figure 64 is 109,568 GPa. The modulus of elasticity is essentially a measure of stiffness and one of the factors used to calculate a material's deflection under load.

At the elastic limit, the material transition from elastic behaviour to plastic behaviour, thus when the load greater than the elastic limit is applied and removed, the material no longer returns to its original position. For the stress-strain graph in Figure 64, the proportional limit is the same as the elastic limit. The offset yield is represented by point B on the graph and for this specific stress-strain graph is 1022,871 MPa. The UTS is determined as the maximum stress the material can withstand, which is represented by point C on the graph (1081,435 MPa).

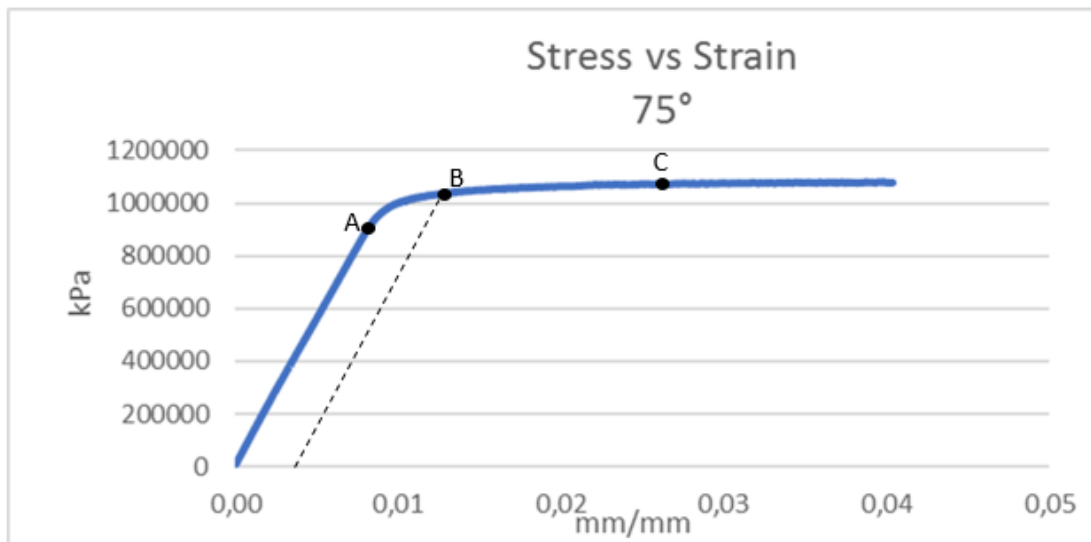


Figure 64: Tensile test result for a 75° sample

In Table 10, the average UTS values of each orientation is presented. As expected, the average UTS for each orientation is higher than for cast and wrought Ti6Al4V due to the microstructure of DMLS Ti6Al4V. The microstructure is strongly affected by the grain size, and the fine powder used in DMLS process generates a fine microstructure which, in turn, provides a higher UTS by inhibiting the dislocation motion as per the according to the Hall-Petch equation. Another reason for the higher UTS is the fact that martensitic microstructure morphology exhibits a high strength and hardness but low ductility.

When analysing the microstructure of DMLS Ti6Al4V it should exhibit a form of anisotropy. In Figure 65, the conclusion can easily be made that the 45° build orientation exhibits the highest UTS, which would be in contrast to some of the conclusions made in literature (Table 7). However, the tested samples are as-built stress-relieved samples and not machined samples to eliminate the effect of the surface conditions. In Figure 65 it is clear that before the effect of the anisotropic microstructure could have an influence on the anisotropy, the effects of all the factors influencing the mechanical properties (as presented in Figure 5) cause the material to fail. Thus, it is not possible to determine whether the difference in strength is due to the layer orientation or merely deviation in dimensions and surface conditions resulting from the build orientation. The lowest UTS and highest UTS differ a mere 5.24 percent, and a definitive conclusion can therefore not be made in terms of anisotropy.

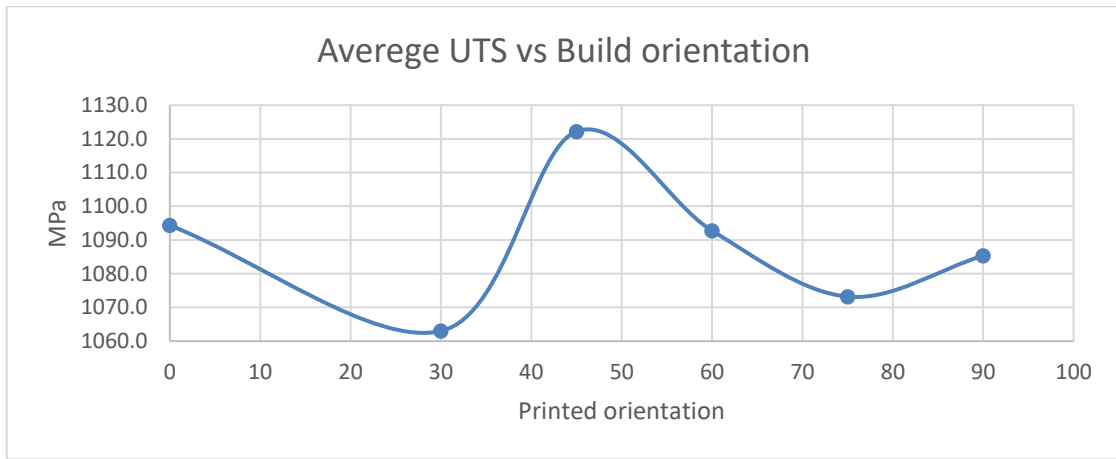


Figure 65: Average UTS vs. printed orientation

Table 10: Average UTS, 0.2% offset yield and modulus of elasticity for each orientation

Orientation	Average UTS (MPa)	Average 0.2% offset Yield (MPa)	Average modulus of elasticity (GPa)
0°	1094,771	1081,167	107,593
30°	1063,459	1022,808	107,834
45°	1122,241	1070,794	111,359
60°	1093,065	1050,388	107,712
75°	1074,066	1021,291	109,505
90°	1085,327	1074,509	111,852

A conservative homogeneous constitution of material with average values of mechanical properties is used as stated in the Problem statement. Thus, the chosen material properties in this study are the average values for the samples printed at 30° with respect to the build platform, since the overall average of the orientation is the lowest of the samples. The chosen material properties are presented in Table 11. These material properties correlate well with the average material properties found in the literature, as presented in Table 6.

Table 11: Material properties of DMLS Ti6Al4V

	UTS	0.2% offset Yield	Modulus of elasticity	Poisson's ratio [129]	Density [129]
Determined	1063,459 MPa	1022,808MPa	107,834GPa	0.35	4400(kg/m ³)
Literature	1146	1028,93	111,1737		
Correlation	92.8%	99.4%	97%		

4.3 Design space

As mentioned in the Problem statement, the topology optimized model must reflect the long term goal of this dissertation, therefore the design space must mimic that of the intended prosthetic arm. Since the design space is limited by the test procedure and the manufacturing cost, a scaled design space with large enough radius at the reduction in diameter was opted for to minimise the stress concentration factor. The test model before topology optimization is presented in Figure 66.

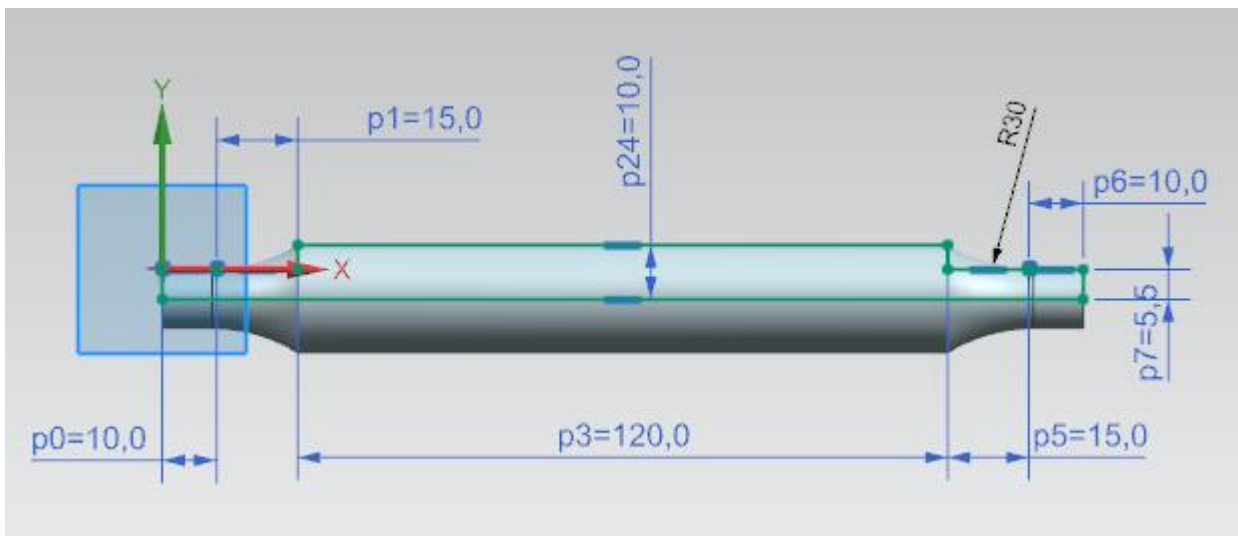


Figure 66: Initial model

In Figure 67, the initial model is presented with the design space highlighted and the grey areas being non-design spaces. The non-design spaces' areas are the areas where the test machine would grip the specimen to perform a stress-related test.

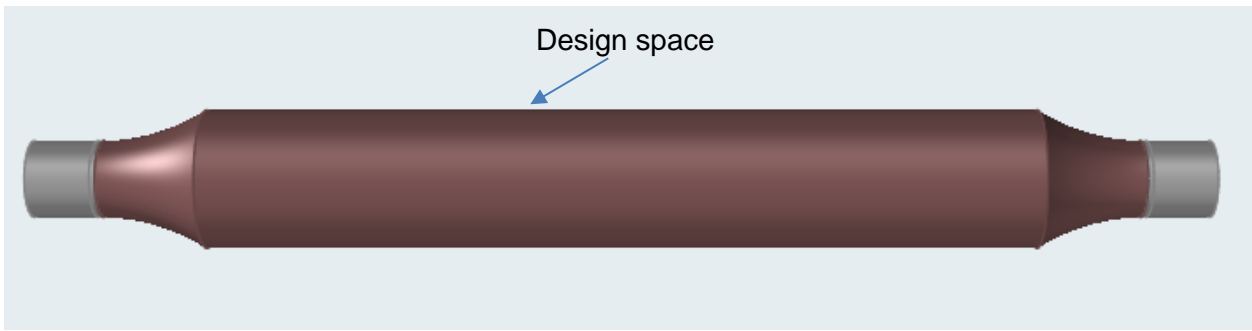


Figure 67: Design space

4.4 Loads

The loads must be balanced to ensure that the model is topology optimized under complex loads (axial, bending and torsional loads), and that the loads play an equally important role in the optimization. According to Hibbeler [135] stress can be defined as “the intensity of the internal forces acting on a specific plane (area) passing through a point”. According to this definition, the loads can be balanced by ensuring their maximum stress is equal and thus have the same effect on the topology optimization. It was decided that the maximum in-plane stress should not exceed 400 MPa. This is done to ensure that there is room for topology optimization.

4.4.1 Axial load

Hibbeler [135] defines an axial load as a load acting along a fixed axis, as seen in Figure 68. Equation 11 is used to calculate the stress induced by an axial load.



Figure 68: Axial load [135]

$$\sigma = \frac{P}{A}, \quad (11)$$

where

σ is the average normal stress at any point on the cross-sectional area, P the internal resultant normal force which acts through the centroid of the cross-sectional area and A is the cross-sectional area of the bar where σ is determined.

By analysing the initial model, it is clear that a stress concentration is likely to occur in the regions where there is a sudden reduction in the cross-sectional area of the model. When the actual stress distributions in Figure 69 b) and average stress distribution in Figure 69 a) are considered, the stress concentration factor K can be determined as follows:

$$K = \frac{\sigma_{max}}{\sigma_{avg}} \quad (12)$$



Figure 69: Stress distribution [135]

When K is known and the average normal stress has been calculated from $\sigma_{avg} = \frac{P}{A}$, and A is the smallest cross-sectional area, the maximum stress can then be determined as $\sigma_{max} = K\sigma_{avg}$.

The stress concentration K has been developed and logged through experiments. In Figure 70, the stress concentration graph is presented for a shoulder fillet in a stepped circular shaft.

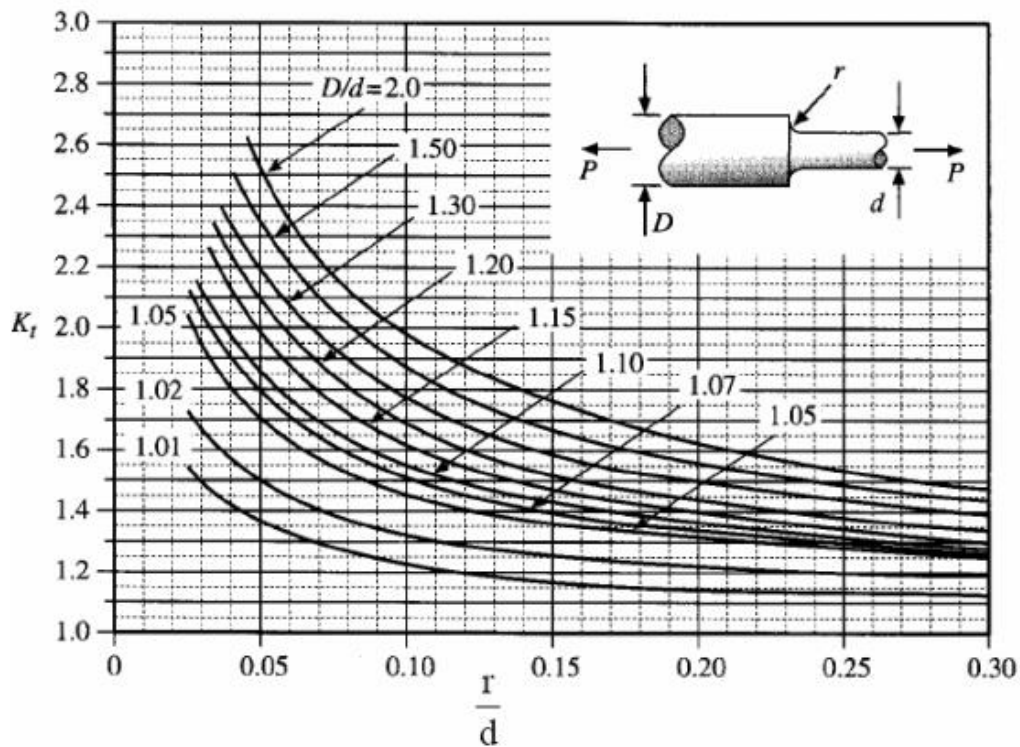


Figure 70: Axially loaded shoulder fillet in stepped circular shaft [135]

For this specific geometry, the stress concentration factor can be determined by the following equation, as derived from Figure 70:

$$K = C_1 + C_2 \frac{2h}{D} + C_3 \left(\frac{2h}{D}\right)^2 + C_4 \left(\frac{2h}{D}\right)^3 \quad (13)$$

Now, if $0.1 \leq \frac{D}{d} \leq 2.0$ then:

$$C_1 = 0.926 + 1.157 \sqrt{\frac{D}{d}} - 0.099 \frac{D}{d}$$

$$C_2 = 0.012 - 3.036 \sqrt{\frac{D}{d}} + 0.961 \frac{D}{d}$$

$$C_3 = -0.302 + 3.977 \sqrt{\frac{D}{d}} - 1.744 \frac{D}{d}$$

$$C_4 = 0.365 - 2.098 \sqrt{\frac{D}{d}} + 0.878 \frac{D}{r}$$

When substituting D, d and r, as indicated in Figure 70, the stress concentration factor $K = 1.07$.

To determine a load that corresponds with the defined maximum stress of 400 MPa, equation 11 must be substituted into equation 12:

$$\sigma_{max} = K \frac{P}{A} \quad (14)$$

With

$$\sigma_{max} = 400 \text{ Mpa.}$$

$$K = 1.07.$$

$$A = \pi 0.0055^2 = 0.000095 \text{ m}^2$$

Then

$$\mathbf{P = 29360.68N}$$

The resulting stress for a tensile load of 29360.98 N is displayed in Figure 71. The maximum stress is 399.60 MPa, which is within 1 percent of the hand-calculated stress. This small difference comes from the assumption made in the hand-calculated operations and FEA.

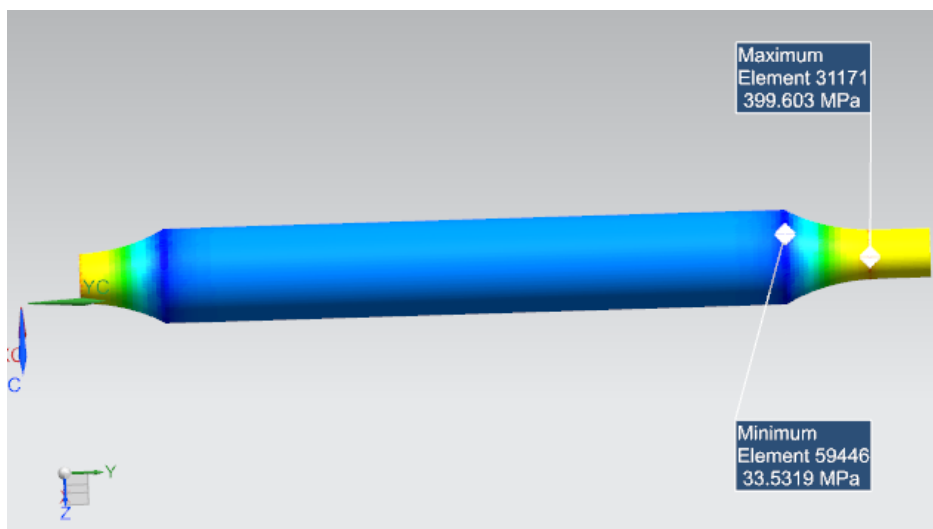


Figure 71: Simulating tensile load in NX™ Pre/Post-application

4.4.2 Bending load

According to Hibbeler [135], a beam is a slender member supporting loads that is applied perpendicularly to the longitudinal axis. When a load is applied to the member away from the point of reference, in other words, a force acting on the member and not passing through the fixed axis, the member will tend to bend. The bending moment is thus a function of the force acting perpendicularly on the longitudinal axis of the member and the distance from the reference point.

In order to determine the maximum internal stresses of a beam, the Flexure formula must be used.

$$\sigma_{max} = \frac{Mc}{I}, \quad (15)$$

where

σ_{max} is the maximum stress which occurs at the furthest point from the neutral axis, M the resultant internal moment, c the perpendicular distance from the neutral axis, and I the moment of inertia of the cross-sectional area about the neutral axis.

The flexure formula can only be used when the normal-stress distribution is linear, and since the sudden change in a cross-sectional area causes the stress distribution to become nonlinear, an alternative method must be discussed. As previously discussed, in the case of axially loaded bars, the maximum stress can be obtained by using a stress concentration factor. The sudden change in cross-sectional area causes a stress concentration, which is described as K. The maximum stress can thus be described by the following equation:

$$\sigma_{max} = K \frac{Mc}{I} \quad (16)$$

K is determined by the following equation for a shoulder fillet in a stepped circular shaft derived from Figure 72:

$$K = C_1 + C_2 \frac{2h}{D} + C_3 \left(\frac{2h}{D}\right)^2 + C_4 \left(\frac{2h}{D}\right)^3 \quad (17)$$

Now, if $0.1 \leq \frac{D}{r} \leq 2.0$, then:

$$C_1 = 0.947 + 1.206 \sqrt{\frac{D}{d}} - 0.131 \frac{D}{r}$$

$$C_2 = 0.022 - 3.405 \sqrt{\frac{D}{d}} + 0.915 \frac{D}{r}$$

$$C_3 = 0.869 + 1.777 \sqrt{\frac{D}{d}} - 0.555 \frac{D}{r}$$

$$C_4 = -0.810 + 0.422 \sqrt{\frac{D}{d}} - 0.260 \frac{D}{r}$$

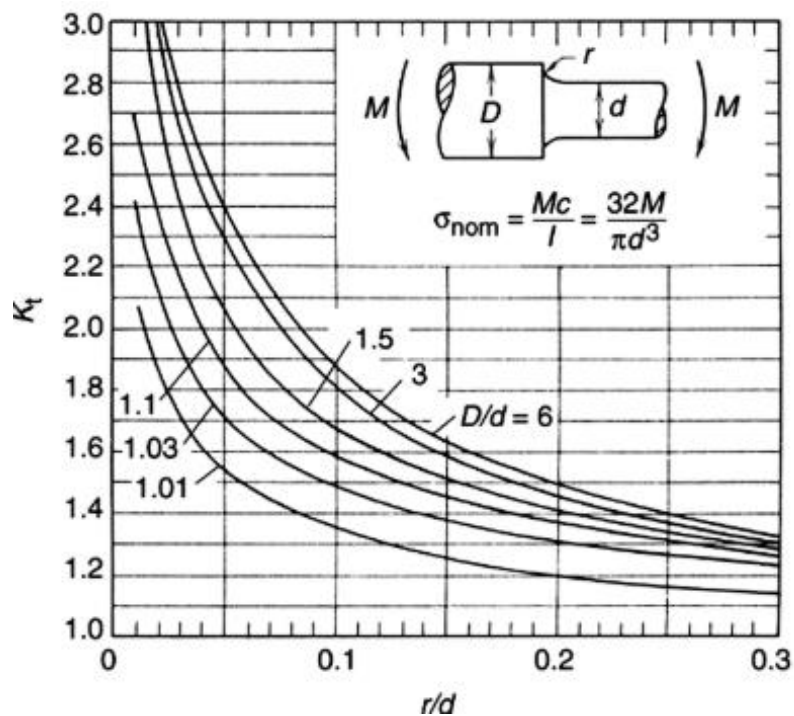


Figure 72: Bending load shoulder fillet in stepped circular shaft [135]

When substituting D , d and r , as indicated in Figure 72, the stress concentration factor $K = 1.11$.

Equation 16 is used to determine the bending load that corresponds with the defined maximum stress of 400 MPa, with:

$$\sigma_{max} = 400 \text{ MPa}$$

K= 1.11

$$\frac{c}{I} = \frac{32}{\pi d^3} = 7652830$$

then

$$M = 47.088512\text{Nm}$$

since $M = PX$,

where X is the distance from the reference point and P the force acting in on the member perpendicular to the neutral axis and which does not pass through the fixed axis.

With

$$X = 150\text{mm}$$

$$M = 47.088512\text{Nm}$$

then

$$\mathbf{P = 313.923N.}$$

The resulting stress for a load of 313.923 N inducing a bending moment is displayed in Figure 73. The difference between hand calculations and FEA results is 1,2 percent due to the assumptions made by both methods.

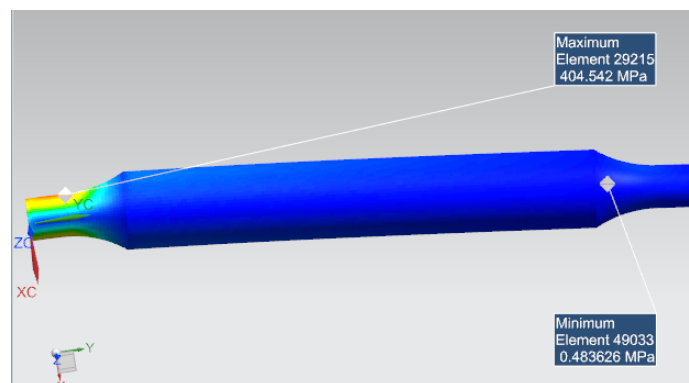


Figure 73: Simulation of bending moment in NX™ Pre/Post-application

4.4.3 Torsional load

According to Hibbeler [135] a torque can be described as the load that causes a member to twist around its longitudinal axis. This phenomenon is illustrated in Figure 74., and the resultant shear stress formula is presented in equation 18.

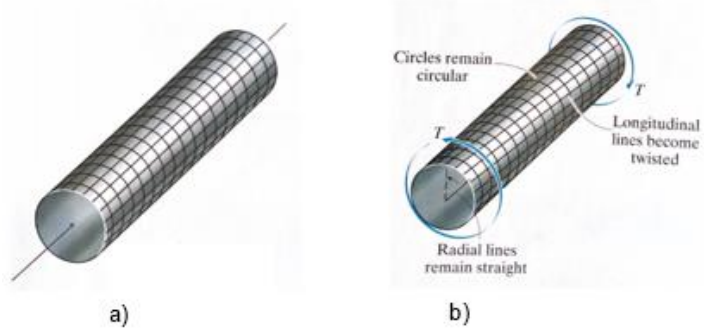


Figure 74: A circular member a) before deformation and b) after deformation [135]

$$\tau_{max} = \frac{Tc}{J} \tag{18}$$

Where

τ_{max} is the maximum shear stress in the shaft, T the resultant internal torque, J the polar moment of inertia, and c the outer radius of the shaft.

To compare the maximum shear stress (τ_{max}) with maximum normal stress (σ_{max}) in the circular member, an axially loaded bar must be considered, as presented in Figure 75.



Figure 75: Axially loaded bar

It is known that the element representing the maximum in-plane shear stress with the associated average normal stresses is oriented at 45° from the element representing the principal stresses, with:

$$\tau_{\max \text{ in plan}} = \sqrt{\left(\frac{\sigma_x - \sigma_y}{2}\right)^2 + \tau_{xy}^2}$$

$$\tau_{\max \text{ in plan}} = \sqrt{\left(\frac{\sigma - 0}{2}\right)^2 + 0^2}$$

$$\tau_{\max \text{ in plan}} = \pm \frac{\sigma}{2}$$

A maximum shear stress of 200 MPa should be used to induce a maximum normal stress of 400 MPa.

With

$$\tau_{\max} = 200 \text{ MPa}$$

$$c = 0.0055 \text{ mm}$$

$$J = \frac{\pi}{2} * 0.0055^4 = 1.4374 * 10^{-9}$$

Substituting these values into equation 18, the Torsion (T) is then equal to **52.26 N.m**.

The resulting stress for a torsional load of 52.26 N.m is displayed in Figure 76. The difference between hand calculations and simulated calculations is 1.15 percent due to the assumptions made by both methods.

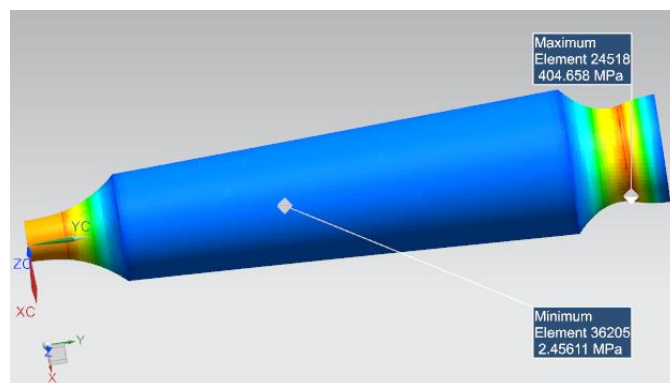


Figure 76: Simulation of torsional load in NX™ Pre/Post-application

4.4.4 Concluding the loads

A simulation of the combined loads is displayed in Figure 77, and it is clear that the maximum stress induced by these loads does not exceed the yield strength as determined in Table 11.

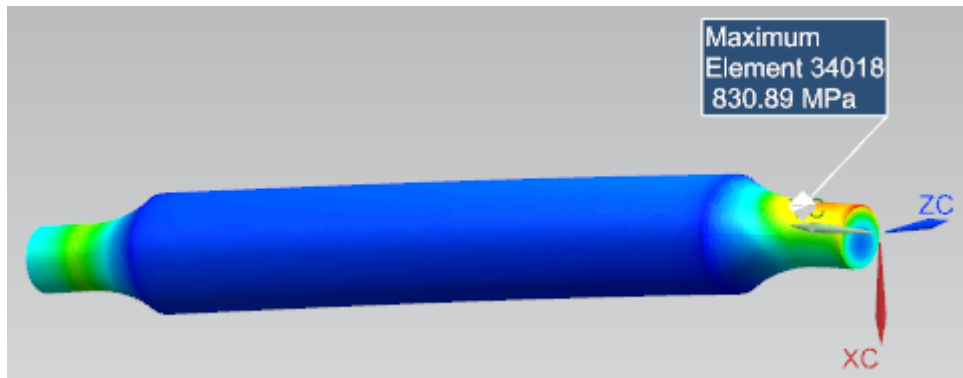


Figure 77: Simulation of combined loads in NX™ Pre/Post-application

To conclude:

Tension load = 29360.68N

Bending load = 313.923N

Torsional load = 52.26 N.m

4.5 Geometry optimization

The topology optimization is done in Altair Inspire™, a proven Topology Optimization software, and the optimization process is divided into the following steps:

The **first step** is to import the model and material properties into the program as specified in Figure 66 and Table 11, respectively. The design space (Figure 67) and material properties are then assigned to the initial imported model (Figure 78).

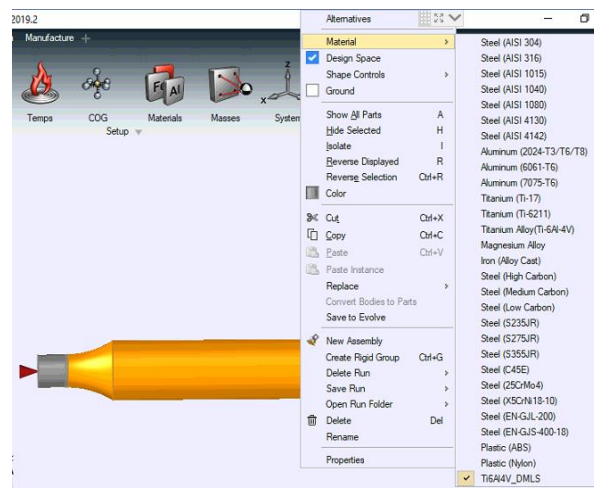


Figure 78: Assigning imported material properties to initial model

In **step two**, the loads and constraints are applied to the model as determined in the Loads section (Figure 79).

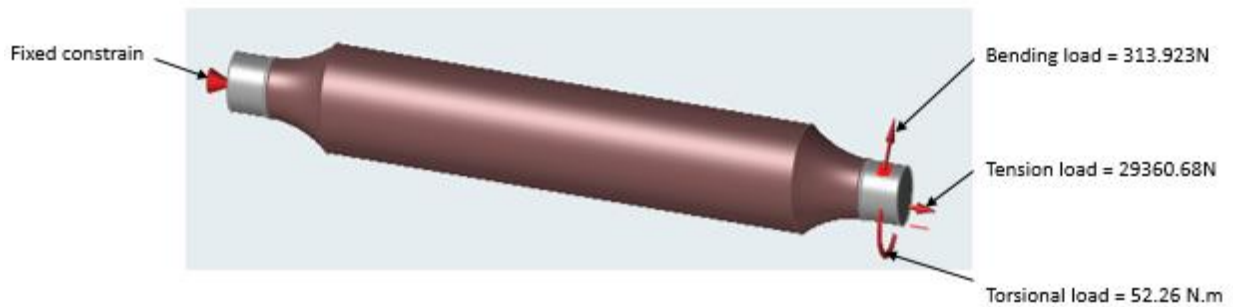


Figure 79: Assign loads to model in Altair Inspire™

The **third step** is to set up the optimization. The desired optimization type is topology, and the desired mass target is defined as 30 percent of the design space. This desired percentage is not the final mass percentage since a feasibility analysis needs to be performed before the final percentage is determined. The minimum thickness constraints are kept to the recommended thickness and the assigned load cases (Figure 80).

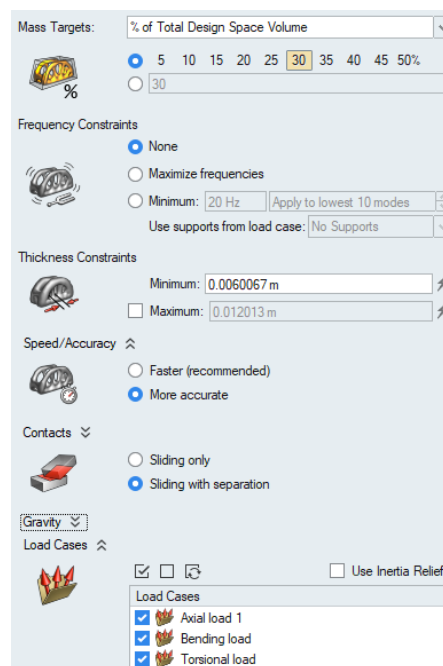


Figure 80: Optimization setup

The **fourth step** is to analyse the obtained geometry and select a feasible mass percentage (Figure 81). The geometry obtained depends on the element size, since the iterative SIMP method focusses on removing elements during each iteration.



Figure 81: Obtained Topology optimized geometry

In the **fifth step** the polynurb function is used to obtain a geometry that is not dependent on the element size (Figure 82).

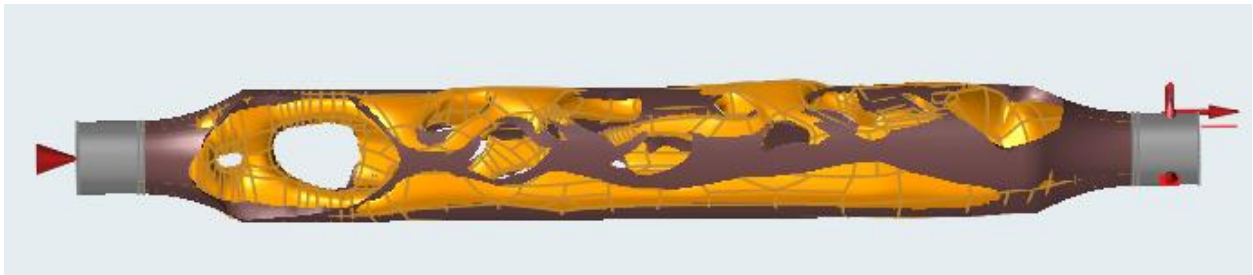


Figure 82: Polynurb geometry

The **sixth** and final step would be to export the polynurb geometry (Figure 83) as a parasolid file in order to do FEM analysis. The log sheet of the topology optimization process is available in APPENDIX C.

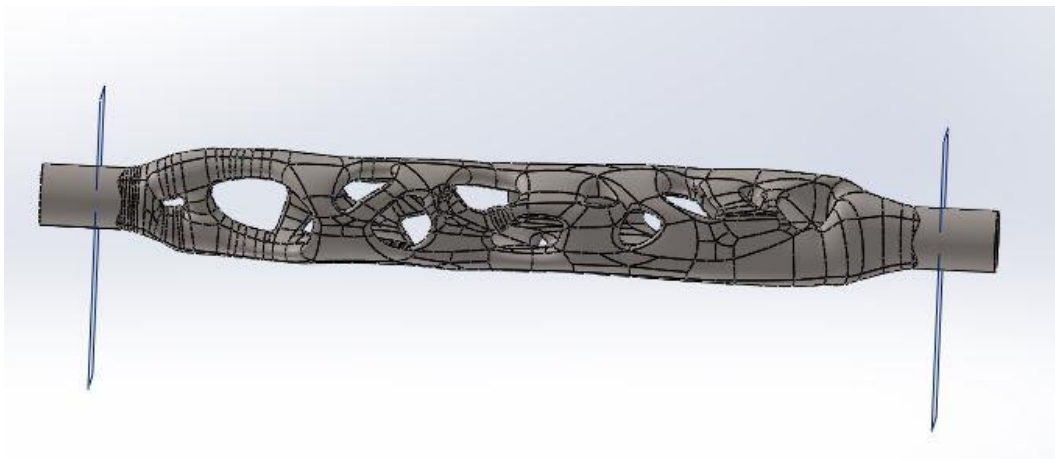


Figure 83: Exported geometry

The initial model as presented in Figure 66 weighs 195.45 g, and the topology optimized model as presented in Figure 83 weighs 104.58 g. The topology optimization thus resulted in 46.5 percent weight reduction. It is important to note that this is not the absolute minimum weight

required to sustain the applied loads but rather close to the optimum, but represents the optimized topology as described in section 2.4.

4.6 Conclusion

In this chapter, the material properties were determined and discussed. The material properties obtained correlate well with the average material properties found in the literature. The initial model and design space were determined. With the initial model's geometry known, the loading conditions used for the topology optimization were calculated. The loads and boundary conditions were then used to obtain a topology optimized model. The topology optimization process is discussed in a step by step fashion.

5.1 Introduction

An FEA is performed on the topology optimized model during this chapter, and the FEA in NX™ 12-Pre/Post-application is compared to FEA performed in SOLIDWORKS® SIMULATION to verify the FEA. Also, this chapter serves to validate the topology optimized model.

5.2 FEM setup

FEM setup is done in NX™ 12 and the process begins by importing the topology optimized model into NX™ 12-Pre/Post-application. A new FEM with solid mesh CTETRA (10) and 1-mm global element size is initialised (Figure 84). This specific mesh is chosen to represent the geometry of the model because of its ability to successfully mesh complex geometries and its ability to handle stress analyses. The CTETRA (10) mesh consists of linear quadratic shape functions.



Figure 84: CTETRA (10) with a 1-mm global element size

The mesh is refined in stress-concentrated areas by applying mesh controls, which leads to reliable results, as presented in Figure 85.

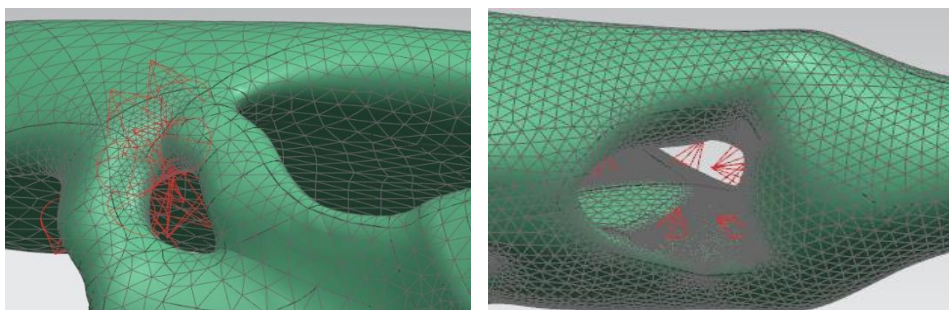


Figure 85: Mesh controls applied to stress concentrated areas

The conservative isotropic homogeneous material properties, as presented in Table 11, are assigned to the imported model (Figure 86).

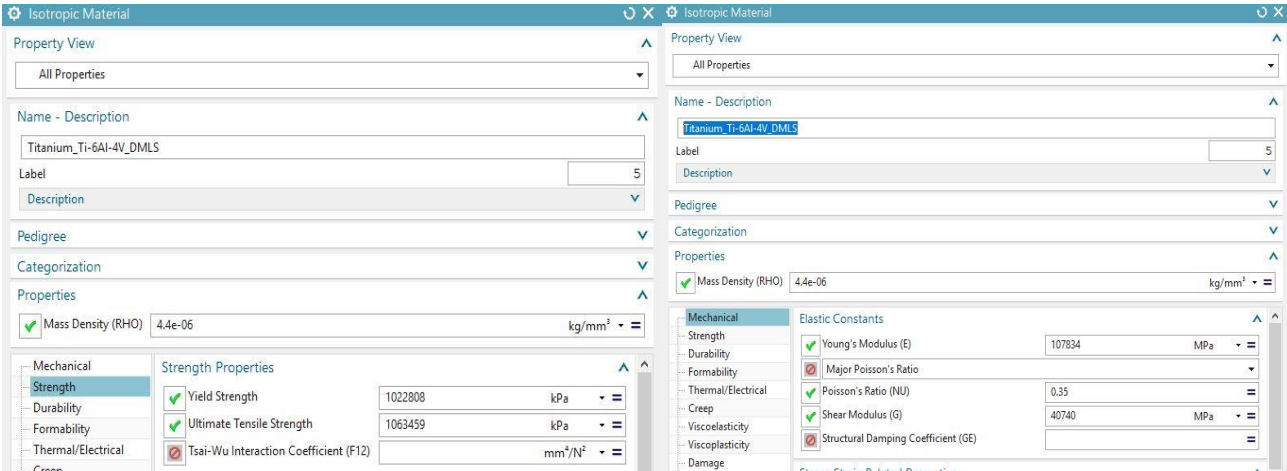


Figure 86: Assigning material properties to FEM model

5.3 FEA of practical test conditions

A new simulation is generated from the FEM file. The current linear static finite element analysis is performed in NX™ 12. The loads and boundary conditions are assigned to the model, and the simulation strives to simulate the exact conditions of the virtual model of the practical test done on the MTS Landmark 370.10 (Figure 57). Thus, the first constraint is a fixed constraint which prohibits any deflection and represents the fixed gripper of the MTS Landmark 370.10. The user defined constraint prohibits displacement in all the degrees of freedom, except for axial displacement along the Y axis. This constraint is applied to represent the gripper's unidirectional movement. The load applied to the model is thus along the Y axis to represent the gripper applying an axial load on the model in the direction of movement. These constraints and load are presented in Figure 87.

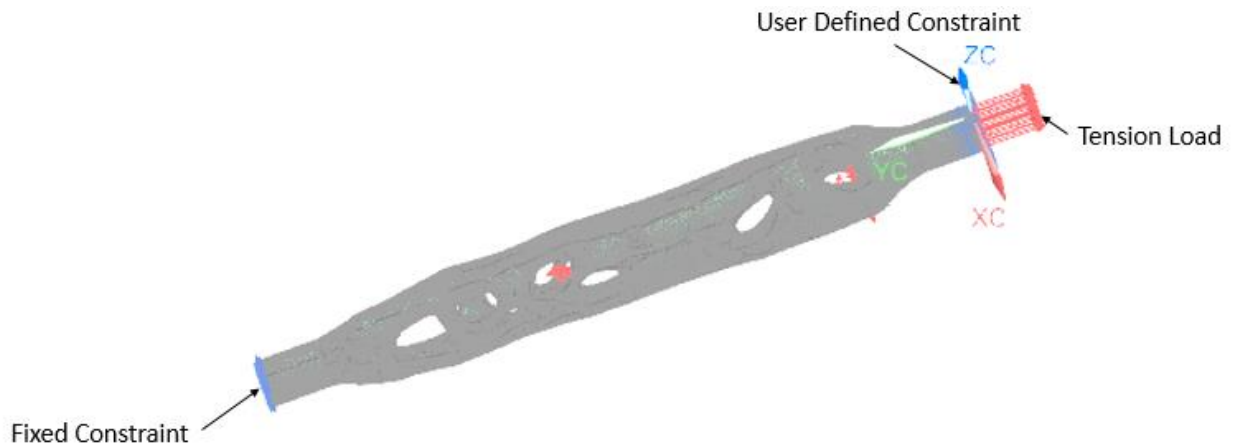


Figure 87: FEA setup of Topology optimized model subjected to practical test conditions.

Various tension loads are applied to the topology optimized model, and a FEA analysis is performed. This is done to compare the stress obtained from the FEA analysis in order to practically determine stress with a variety of loads. The three FEA analysis are FEA 1 = 20 kN; FEA 2 = 25 kN; FEA 3 = 29.36 kN. For all the different loads applied, the boundary conditions and material properties are kept constant.

5.4 Verifying finite element analysis

The FEA is verified by comparing the maximum stress and stress distribution as obtained from the FEA done in NX™12- Pre/Post-application and the FEA performed in SOLIDWORKS® SIMULATION. For the purpose of verifying the FEA, the results of FEA 3 are discussed and compared, since this is the tension load at which the model is topology optimized.

The results for FEA 3 performed in the NX™12- Pre/Post-application are displayed in Figure 88. The maximum von Mises stress is 972.2 MPa and is located at the position displayed in Figure 89. The results for FEA 3 performed in the SOLIDWORKS® SIMULATION is displayed in Figure 90. The maximum von Mises stress is 930,5 MPa and is located at the position as indicated in Figure 91. In the SOLIDWORKS® SIMULATION the option of automatic mesh creation is chosen in order to compare the mesh quality created in the NX™12 by the user. When the same boundary constraints and load are applied to the same topology optimized model in two different simulation software packages, a correlation in the results can be observed. It is clear from Figure 89 and Figure 91 that in both cases, the maximum stress is at the same location. From Figure 88 and Figure 90 it becomes clear that the same stress distribution is obtained. The resultant maximum stress only differs from one another by 7.1 percent. The conclusion can thus be made that the FEA analysis performed in NX™12-Pre/Post-application results in trustworthy results.

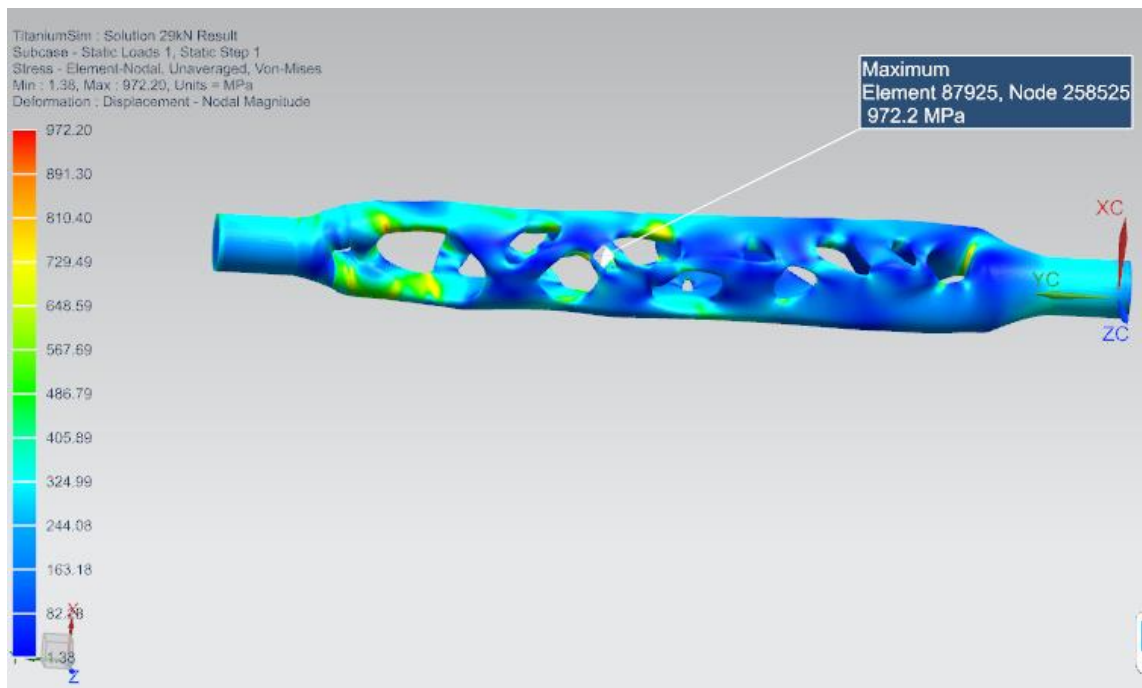


Figure 88: FEA results of FEA 7 as obtained from NX™12-Pre/Post-application

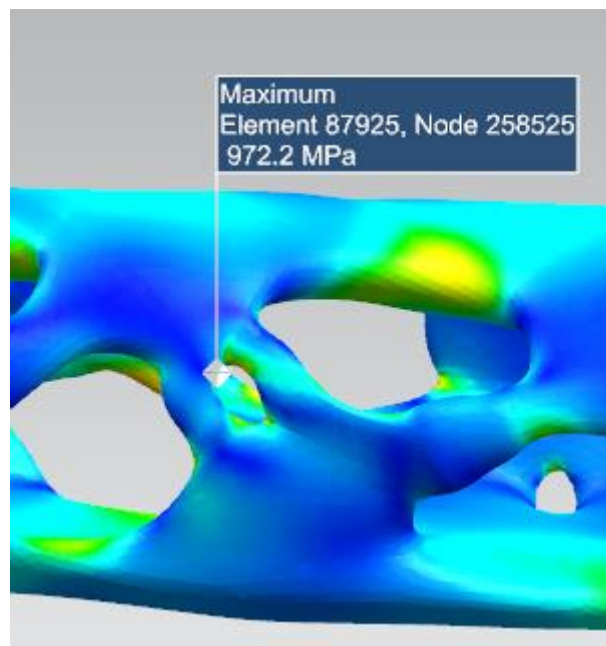


Figure 89: Position of maximum stress as obtained from NX™12-Pre/Post-application

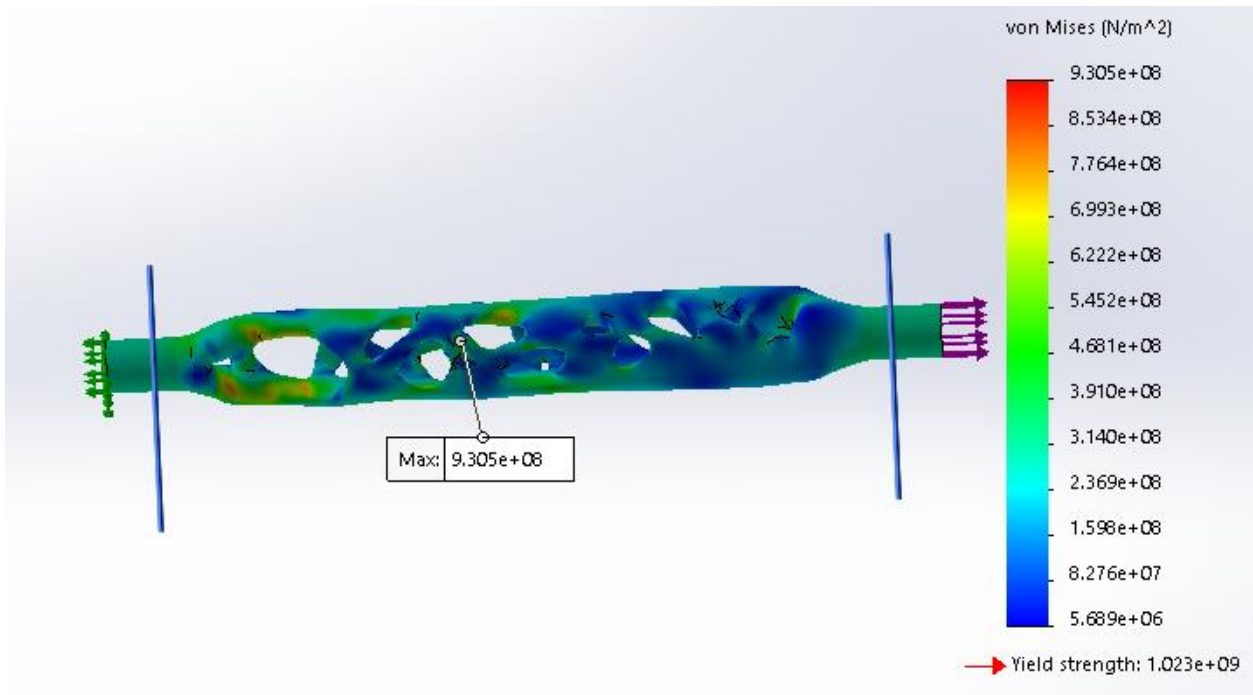


Figure 90: FEA results for FEA 7 as performed in SOLIDWORKS® SIMULATION

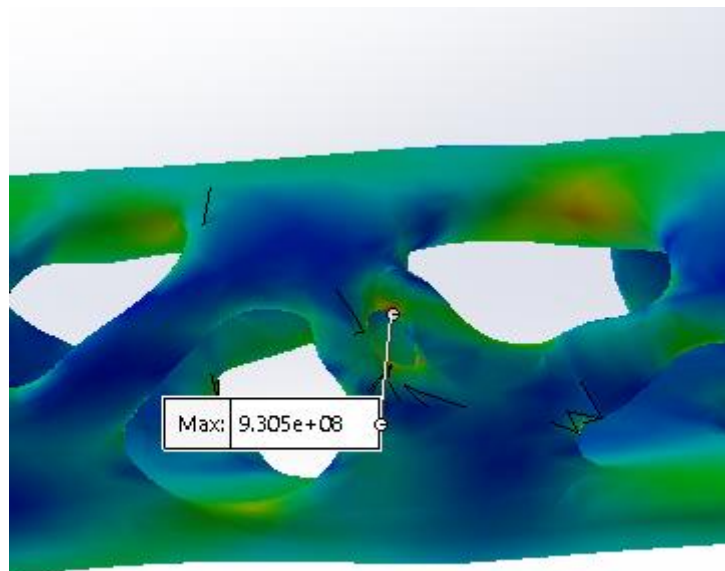


Figure 91: Position of maximum stress as obtained from SOLIDWORKS® SIMULATION

5.5 Selecting the virtual strain rosette positions

Virtual Strain rosette are used to compare the simulated results and the practically obtained result. The strain rosette must be positioned in areas where the stress is constant, as these areas are a true representation of the actual stress the component experiences. It is thus decided to position the strain rosette in two different constant stress areas, as displayed in Figure 92.

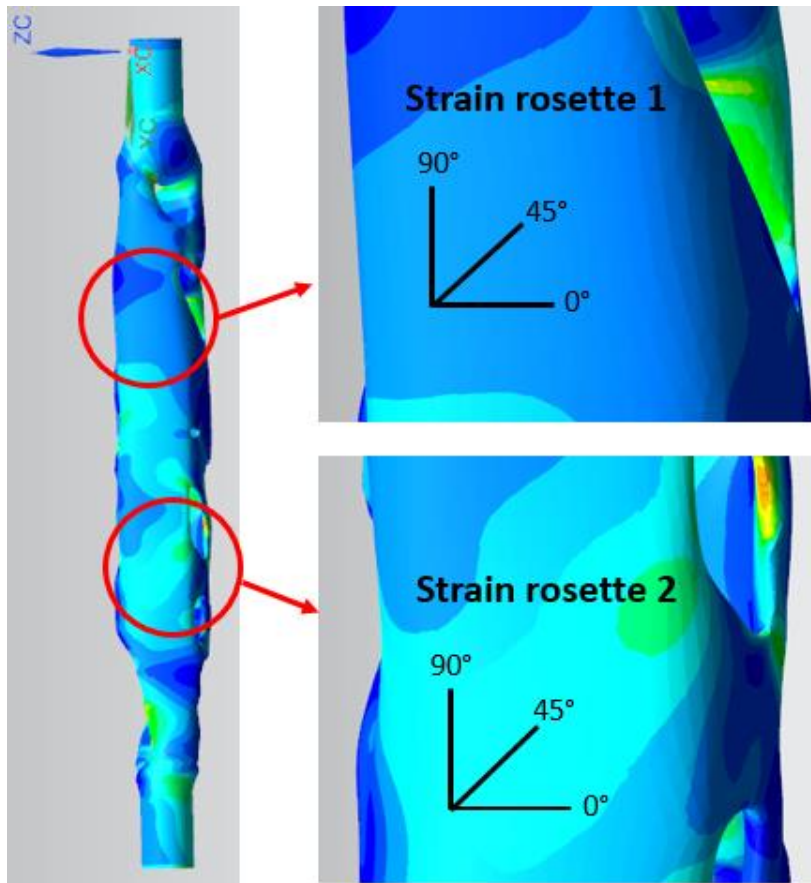


Figure 92: Strain rosette positions

5.6 Validating the Topology optimized model

Validating the topology optimized model would require it to be able to withstand the same loads as those applied in the initial model without a noteworthy stress increase. When the same boundary conditions and loads are applied to the topology optimized model (Figure 93) and initial model displayed in Figure 79, and a new FEA analysis is performed in NX™12-Pre/Post-application, such that the maximum von Mises stress is 943.28 MPa (Figure 94).

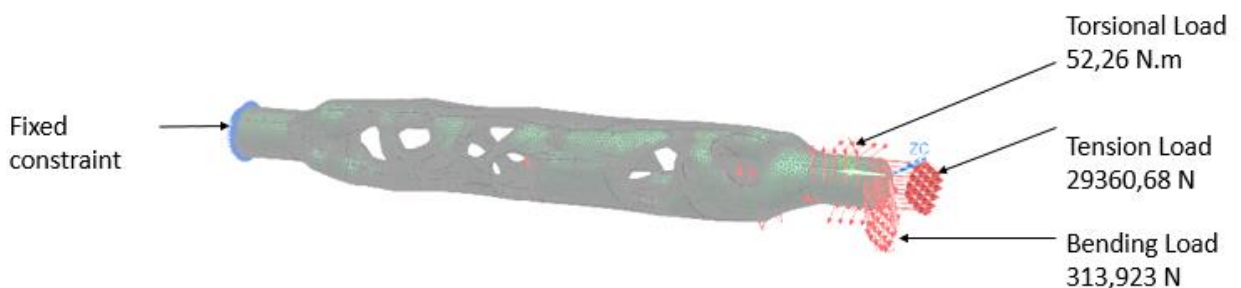


Figure 93:FEA setup of Topology optimized model subjected to initial conditions

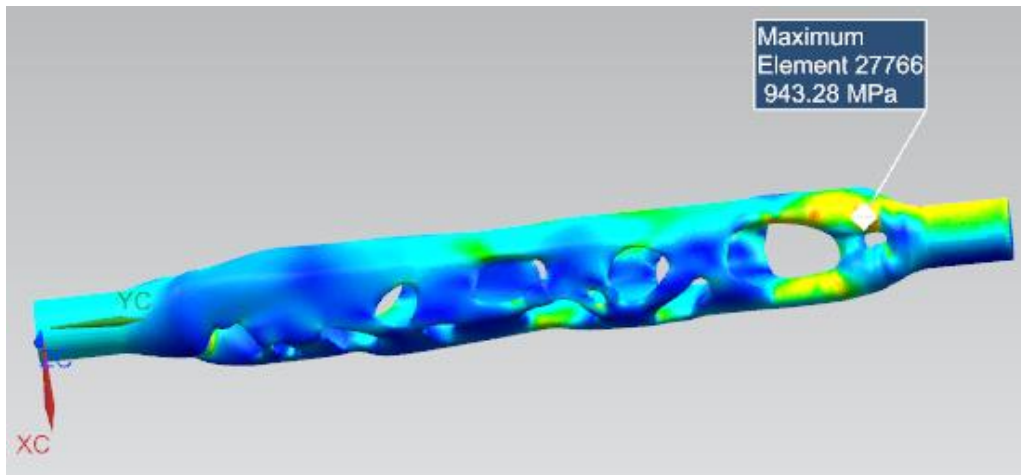


Figure 94: Simulation results of Topology optimized model subjected to initial conditions

The maximum stress when the topology optimized model is simulated under practical test conditions (Figure 87) with the tension load being the load at which the model is topology optimized is 972.2 MPa. The maximum stress is located at the position identified in Figure 89. It is thus interesting to note that the simulation result indicates that the maximum stress with initial conditions (Figure 93) is lower than when it is exposed to the practical test conditions. The maximum stress is also detected at a different location because of the nature of the model's structure, given that the model is optimized to withstand a combination of loads and, by applying only a single load, the balance is disturbed and thus an increase in the stress is observed. This stress increase as observed for practical test conditions is less than 3 percent and therefore is not of concern.

However, the maximum stress when the initial conditions are applied to the topology optimized model is still below the yield strength of the material and only resulted in a 12-percent stress increase with 46.5-percent mass reduction. The topology optimized model is a good representation of the initial model in terms of maximum stress experienced and the structural integrity is thus maintained and therefore the topology optimized model is validated.

5.7 Conclusion

The FEM setup was conducted and explained in this chapter. The FEA of practical test conditions were displayed and the logical reasoning behind the FEA was explained. In this chapter, the FEA results as obtained from NX™12-Pre/Post-application and the SOLIDWORKS® SIMULATION were compared, and, since there is a strong correlation, the results were concluded to be trustworthy, thus verifying the FEA done in NX™12-Pre/Post-application. With the FEA results known the virtual strain rosette positioning was selected and positioning explained. The topology optimized model was validated by comparing the FEA of the initial model and the FEA of the

topology optimized model. The conclusion was made that the topology optimized model is a good representation of the initial model in terms of maximum stress experienced and was thus validated.

6.1 Introduction

This chapter describes the experimental procedure. The procedure begins with the preparation of the topology optimized model for practical testing. The model is then practically tested with the MTS Landmark 370.10.

6.2 Topology optimized model preparations.

The topology optimized model was printed at CRPM and the exact same printing process in section 4.2 is followed. In Figure 95 displays the DMLS topology optimized model as received from CRPM. The model preparation thus begun by cleaning the topology optimized model of excess support material. Care is taken when removing the support material to ensure that no visual damage is caused to the DMLS topology optimized model.



Figure 95: DMLS Topology optimized model

The DIC system is based on the principle of comparing digital photographs of a component at different stages of deformation by tracking blocks of speckles. The pixel blocks need to be random and unique with a range of contrast and intensity levels. A dishwashing sponge is used to apply black acrylic paint on the DMLS topology optimized model in order to create a speckled pattern as displayed in Figure 96. A visual test is performed to ensure the speckle pattern complies with the criteria as described. The speckled pattern is displayed in Figure 97.



Figure 96: Applying black acrylic paint on DMLS Topology optimized model

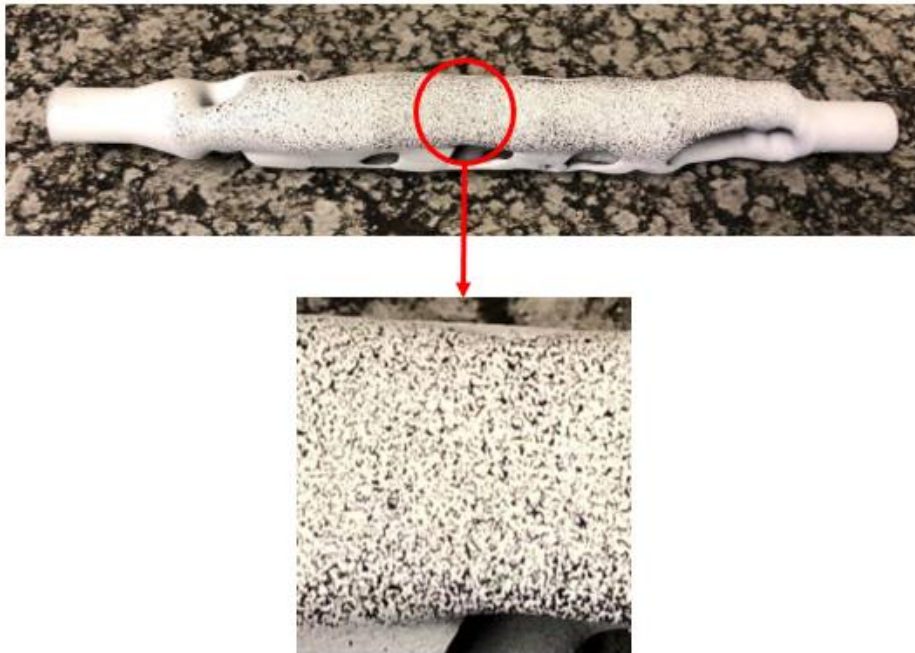


Figure 97: Speckled pattern

6.3 DIC system setup

The DIC system setup begins by physically assembling all the components as displayed in Figure 98. Care should be taken to ensure that the cameras are level. The system must be calibrated by taking images of a calibration panel in Istra4D from different perspectives. The camera aperture, angle, focus and exposure are then calibrated for the specific position of the model being tested.



Figure 98: Assembling the DIC system

6.4 Practical testing

The topology optimized model is tested practically using the MTS Landmark 370.10, and the practical test is a practical representation of the simulation conditions as presented in Figure 87. The topology optimized model is clamped in the MTS with a pressure of 8 MPa. Different tensional loads are applied to the topology optimized model at a strain rate of 0.025 mm/s. These loads are: Load 1: 20 kN; Load 2: 25 kN; Load 3: 29.36 kN. A reference image is taken with the DIC system before any load is applied to the topology optimized model after which an image is taken for each targeted load.



Figure 99: Practical test of Topology optimized model

6.5 Applying virtual strain gauges

Two practical tests are performed on the topology optimized model. The virtual strain rosette is applied to the areas as identified in Figure 92 and presented in Figure 100.

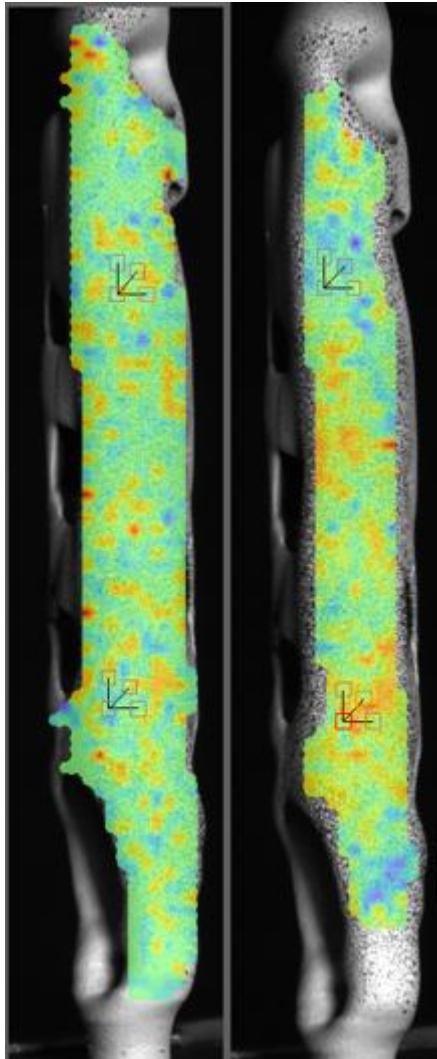


Figure 100: Applying virtual strain rosette

6.6 Conclusion

Chapter 6 focussed on providing the reader with the experimental procedure from model preparation to practical testing of the topology optimized model.

7.1 Introduction

During this chapter the simulated results are obtained together with the experimental results. The results are then compared and discussed.

7.2 Simulated results

The results of FEA 3 = 29.36 kN are presented in Figure 101. This is the load condition under which the model is topology optimized. The resultant maximum stress is 972.2 MPa, which is well below the material's Yield strength. The verified simulation thus proves that the model should be able to withstand the tensional load.

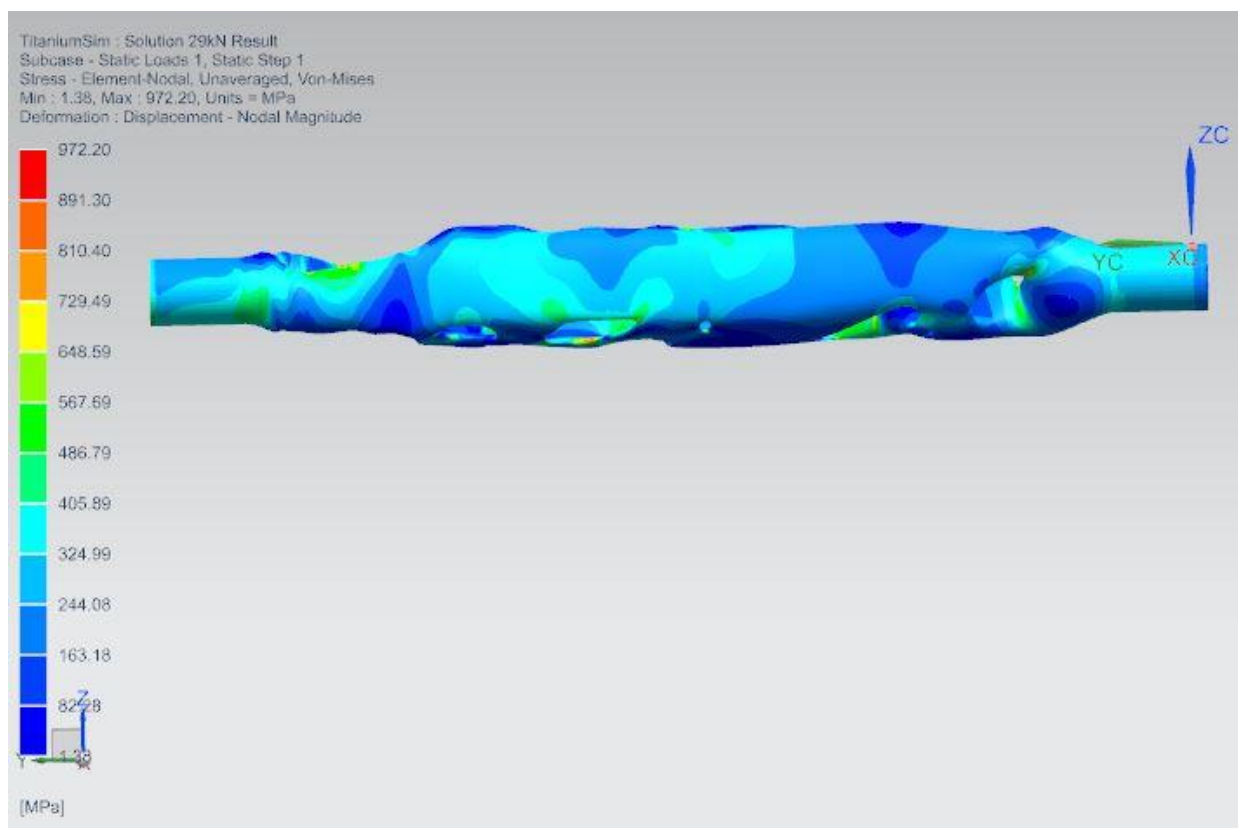


Figure 101: FEA 3: 29.36kN

In APPENDIX D the results for FEA 1 and FEA 2 are displayed. The resultant stress for the areas where the virtual strain rosette is positioned for each FEA is presented in Table 12.

Table 12: Resultant stress for each chosen position

FEA	Load	Position 1(MPa)	Position 2 (MPa)
1	20	165,62	275,41
2	25	207,03	344,27
3	29,36	244.08	405,89

7.3 Experimental results

The strain obtained from the practical tests is displayed in Table 13 and Table 14.

Table 13: Resultant strain from practical test 1

Practical test 1						
	Position 1 (mm/mm)			Position 2 (mm/mm)		
Load (kN)	90°	0°	45°	90°	0°	45°
20	1,20603	-0,466764	0,802279	2,204299	-0,845373	0,3233296
25	1,46678	-0,663695	1,0800336	2,666235	-1,2151	0,276208
29.36	1,70207	-0,766814	1,370907	3,318071	-1,153231	0,464559

Table 14: Resultant strain from practical test 2

Practical test 2						
	Position 1 (mm/mm)			Position 2 (mm/mm)		
Load (kN)	90°	0°	45°	90°	0°	45°
20	1,21128	-0,46545	0,815511	2,13515	-0,62466	0,22685
25	1,63900	-0,38004	1,234174	2,575994	-1,0379	0,208616
29.36	1,91748	-0,61882	1,283646	3,443956	-1,35893	0,280738

As discussed in section 3.5 the strain obtained from the strain rosette is used to determine the maximum in-plane shear strain and principal in-plane strains. These maximum in-plane shear strains and principal in-plane strains are used to determine maximum in-plane shear stress and principal in-plane stress. As mentioned in section 3.4, the von Mises stress is determined by using the maximum in-plane shear stress and principal in-plane stress. The resultant von Mises stresses as obtained from the virtual strain rosette at position 1 and 2 for practical test 1 and 2, respectively, are presented in Table 15.

Table 15: Resultant von Mises stress obtained from virtual strain rosette

	Practical test 1		Practical test 2	
Load (kN)	Position 1 (MPa)	Position 2 (MPa)	Position 1 (MPa)	Position 2 (MPa)
20	134,4	245,7	145	239,8
20	187	300,7	193,4	291,2
29,39	225,3	367,7	223,8	389,1

7.4 Results discussion

In Table 16 and Table 17 under APPENDIX E the resultant von Mises stresses as determined from the strain rosette for practical test 1 and 2 at position 1 and 2 are compared. For the different load cases, the average correlation percentage for position 1 is 96.2 percent and position 2 is 96.3 percent. The excellent correlation between the two practical test for both positions (as seen in Figure 102 and Figure 103) indicates that this procedure is highly repeatable with consistent results, which further confirms that the positioning of the virtual strain rosette is correct.

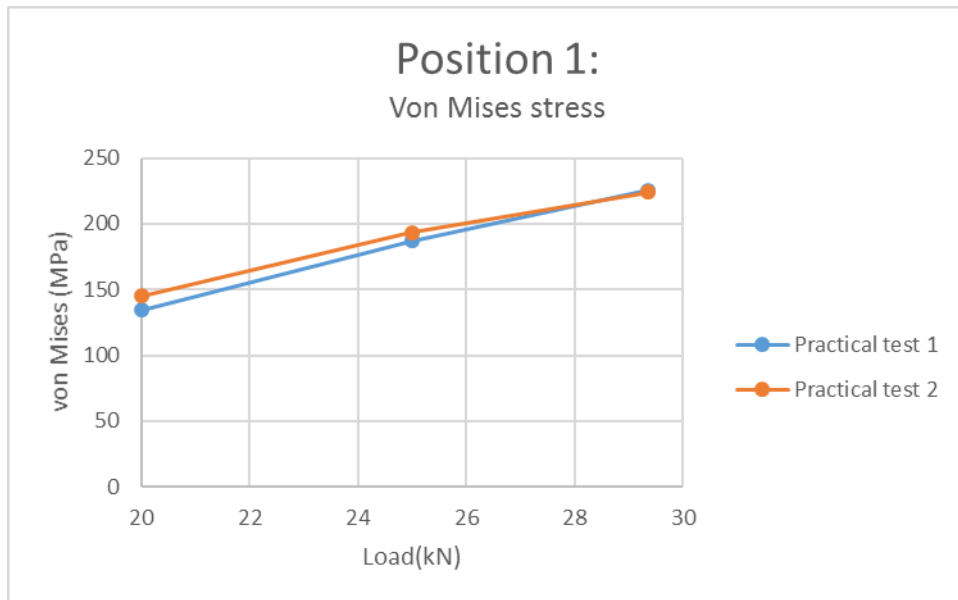


Figure 102: Comparison of the resultant von Mises stresses for position 1 as obtained from the two practical test

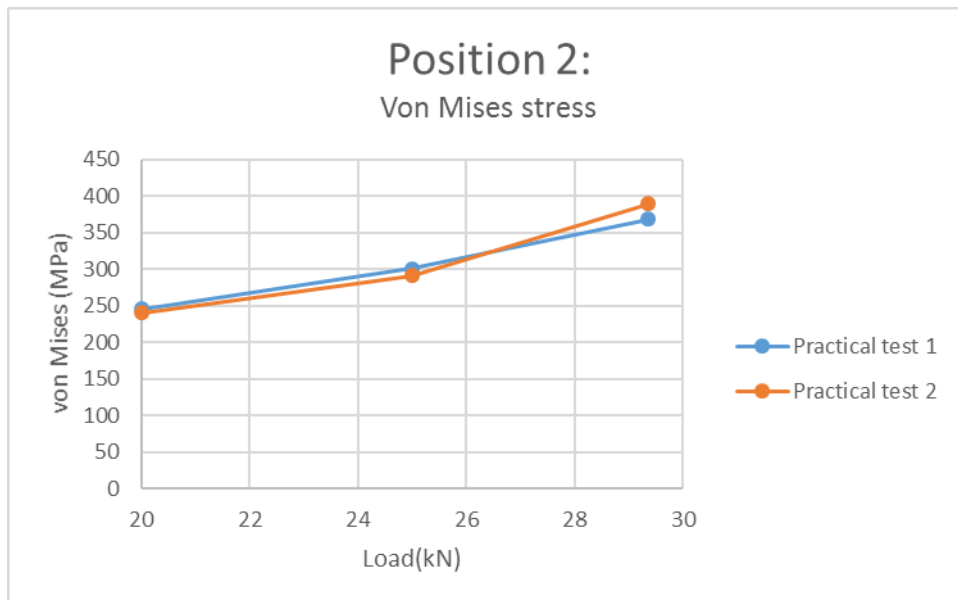


Figure 103: Comparison of the resultant von Mises stresses for position 2 as obtained from the two practical test

The correlation between the von Mises stress determined from the virtual strain rosettes and practical test 1 for position 1 and 2 is presented in Figure 104 and Figure 105. For both positions 1 and 2, a good linear correlation can be observed with the practically obtained von Mises stress consistently lower than simulated results (90% correlation APPENDIX E). This occurrence is ascribed to the fact that a conservative homogeneous constitution of material with average values of mechanical properties is used.

The FEA results display excellent linear relation since the FEA performed is a linear static analysis. It is important to note that the practically obtained von Mises stress follows the same linear relation. This is true for practical test 1 and 2, as displayed in Figure 104, Figure 105 and under APPENDIX E in Figure 115 and Figure 116. When the weakest material's properties are used in the FEA, a correlation between the FEA results and practically obtained results is observed, thus proving that the FEA is validated and therefore the finite element analyses are valid when applied to topology optimized DMLS structures manufactured from Ti6AL4V with the assumption that the weakest material properties are homogeneous.

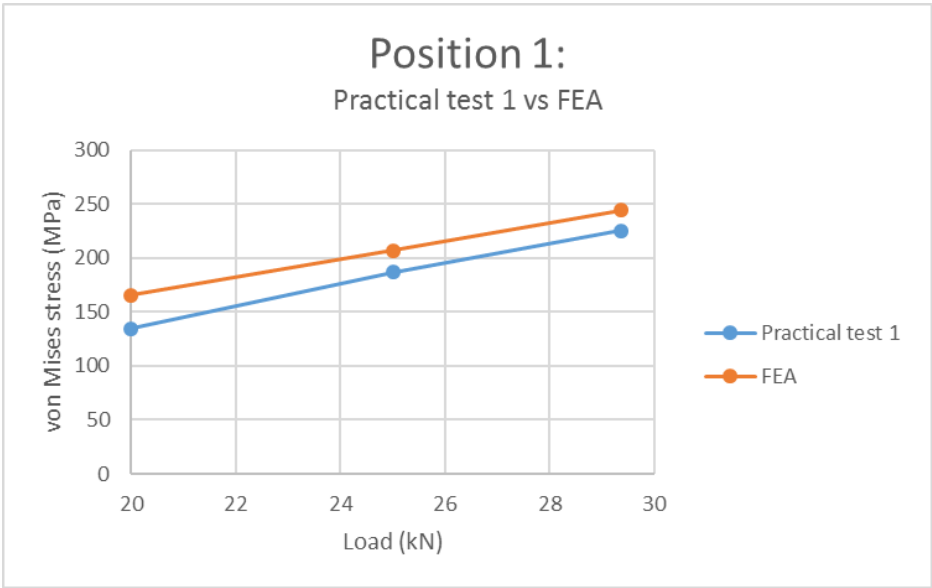


Figure 104: Comparison of von Mises stress as obtained from FEA and practical test 1 at position 1

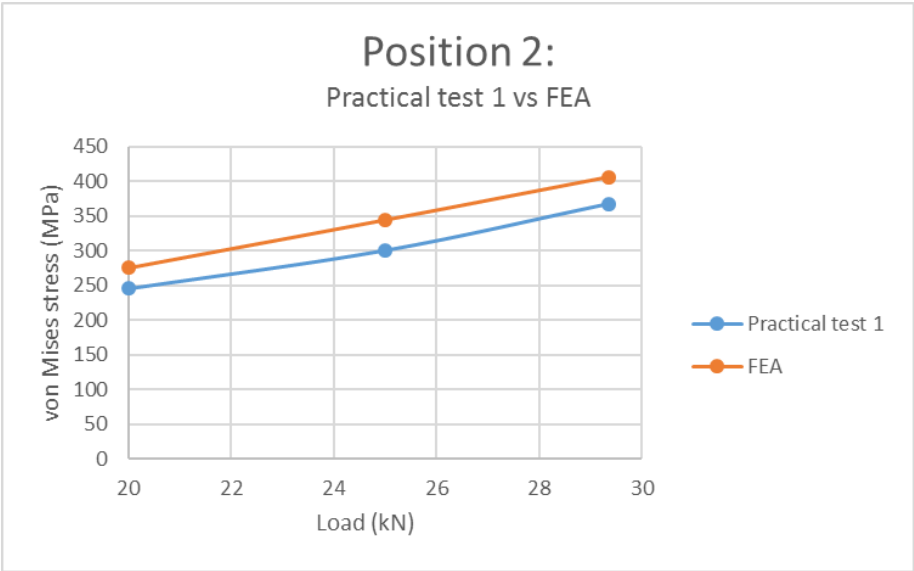


Figure 105: Comparison of von Mises stress as obtained from FEA and practical test 1 at position 2

7.5 Conclusion

This chapter aimed to provide the FEA results and the strain obtained from the virtual strain rosette. The strain obtained from the virtual strain rosette was then processed to resemble von Mises stress. Next, the von Mises stress is calculated for two different positions experiencing constant stress. The importance of the positioning of the strain gauges is explained elsewhere (see Selecting the virtual strain rosette positions). Two practical tests were performed on the topology optimized model. The von Mises stress for different loads was determined from the virtual strain rosette and obtained from the FEA. These simulated von Mises stress and practically obtained von Mises stress were compared in an attempt to validate the simulation. An excellent linear correlation between the practical results and simulated results were found, with the practically obtained results being consistently lower than the simulated results. The reason given for this phenomenon is the use of the weakest material properties as homogeneous. A verifiable conclusion is drawn and the problem under investigation is addressed.

8.1 Introduction

This chapter provides the conclusions of the results of the presented body of work. Recommendations for future work is also presented.

8.2 Conclusions

Various conclusions could be made from the presented research of which some are presented in this section. The conclusions can be categorised in four subsections, namely, conclusions about the material properties, conclusions about the developed topology optimized model, conclusions about the FEA and conclusions about the method of validation of the FEA.

The decision was made to determine the mechanical properties because of the wide range of mechanical properties presented in Table 6 and the controversial conclusions drawn from authors who have investigated the material properties in Table 7. An attempt was made to determine the anisotropy of the material. The manufacturing technique alters the microstructure and therefore the material should exhibit a form of anisotropy. But the conclusion was clearly reached that the samples fail due to all the parameters influencing the mechanical properties before the effects of the anisotropic microstructure is experienced. This does not disregard the effect of the microstructure on the mechanical properties, since it is clear that the mechanical properties of DMLS Ti6Al4V result in both higher yielding and UTS than wrought Ti6Al4V. As stated in the Problem statement, a conservative homogeneous constitution of weakest determined material properties was used for the topology optimized model.

A topology optimized model was developed with a complex load condition. The topology optimized model was validated by comparing the stress induced by the complex loads on the initial model and the topology optimized model as well as weight reduction of the model. With a mere 12-percent stress increase and 46.5-percent mass reduction, the topology optimized model is clearly validated.

An FEA analysis was performed on the validated topology optimized model. This FEA analysis strives to mimic the conditions of the practical test performed on the topology optimized model. The FEA was performed in more than one software package to compare the simulations and verify the FEA. The resultant maximum stress only differed from one another by 7.1 percent, and

the stress distribution correlates well between the two software packages. The conclusion can thus be made that the FEA analysis performed in NX™12-Pre/Post-application results in trustworthy results.

Two practical test were performed on the topology optimized model. The von Mises stress for different loads were determined from the virtual strain rosette and obtained from the FEA. These simulated von Mises stress and practically obtained von Mises stress were compared in an attempt to validate the simulation. A favourable linear correlation was found between the practical results and simulated results, with the practically obtained results being consistently lower than the simulated results. The reason given for this phenomenon is the use of the weakest material properties as homogeneous. A verifiable conclusion was drawn and the problem under investigation addressed.

8.3 Recommendations

A few observations were made throughout this study, and as such the following topics are recommended for future research:

- The validation of dynamic FEA applied to DMLS topology optimized structure
- Study the effects of topology optimization on the structure's stiffness
- The validity of FEA applied to nonlinear analyses.

8.4 Closure

The aim of this dissertation was to determine the validity of FEA when applied to topology optimized DMLS structures manufactured from Ti6Al4V with the assumption that the weakest material properties are homogeneous. The conclusion made was that the FEA proves to be valid when the weakest material properties are used for the FEA; therefore, the study's aim has been accomplished.

9 References

- [1] *Why is Weight So Important in Cycling? Part 1 | TrainingPeaks*. [Online]. Available: <https://www.trainingpeaks.com/blog/why-is-weight-so-important-in-cycling-part-1/###> (accessed: Oct. 18 2018).
- [2] M. P. Bendsøe and O. Sigmund, Eds., *Topology Optimization: Theory, Methods, and Applications*. Berlin, Heidelberg: Springer Berlin Heidelberg, 2004.
- [3] *Topology Optimization Software | Altair*. [Online]. Available: https://www.altair.com/topology-optimization/?_ga=2.206097428.662667943.1582094262-1986419746.1582094262&_gac=1.81211877.1582094263.Cj0KCQiAs67yBRC7ARIsAF49CdXTtMiOxCeKuX5h6uN8M6ACJrjef3IUJ7tRJLRVPo8Siv11re_HMSkaApsEALw_wcB## (accessed: Feb. 19 2020).
- [4] N. Guo and M. C. Leu, "Additive manufacturing: Technology, applications and research needs," *Front. Mech. Eng.*, vol. 8, no. 3, pp. 215–243, 2013, doi: 10.1007/s11465-013-0248-8.
- [5] W. E. Frazier, "Metal Additive Manufacturing: A Review," *J. of Materi Eng and Perform*, vol. 23, no. 6, pp. 1917–1928, 2014, doi: 10.1007/s11665-014-0958-z.
- [6] N. Gardan and A. Schneider, "Topological optimization of internal patterns and support in additive manufacturing," *Journal of Manufacturing Systems*, vol. 37, pp. 417–425, 2015, doi: 10.1016/j.jmsy.2014.07.003.
- [7] M. E. Orme, M. Gschweidl, M. Ferrari, I. Madera, and F. Mouriaux, "Designing for Additive Manufacturing: Lightweighting Through Topology Optimization Enables Lunar Spacecraft," *Journal of Mechanical Design*, vol. 139, no. 10, p. 100905, 2017.
- [8] N. A. Waterman and P. Dickens, "Rapid Product Development in the USA, Europe and Japan," *World Class Des to Man*, vol. 1, no. 3, pp. 27–36, 1994, doi: 10.1108/09642369210056629.
- [9] G. Kasperovich and J. Hausmann, "Improvement of fatigue resistance and ductility of TiAl6V4 processed by selective laser melting," *Journal of Materials Processing Technology*, vol. 220, pp. 202–214, 2015, doi: 10.1016/j.jmatprotec.2015.01.025.
- [10] *Terminology for Additive Manufacturing - General Principles - Terminology*, 2015.
- [11] Y.-C. Chang, "Design of desktop-scale metal wire-feed prototyping machine," 2016.
- [12] *The 3D Printing Handbook: Technologies, design and applications*: 3D Hubs B.V, 2017.

- [13] J.-P. Kruth, G. Levy, F. Klocke, and T.H.C. Childs, "Consolidation phenomena in laser and powder-bed based layered manufacturing," *CIRP Annals*, vol. 56, no. 2, pp. 730–759, 2007, doi: 10.1016/j.cirp.2007.10.004.
- [14] S. Das, "Producing metal parts with selective laser sintering/hot isostatic pressing," *JOM*, vol. 51, no. 4, p. 2, 1999, doi: 10.1007/s11837-999-0067-x.
- [15] B. AlMangour and J.-M. Yang, "Improving the surface quality and mechanical properties by shot-peening of 17-4 stainless steel fabricated by additive manufacturing," *Materials & Design*, vol. 110, pp. 914–924, 2016, doi: 10.1016/j.matdes.2016.08.037.
- [16] M. Frey, M. Shellabear, and L. Thorsson, "Mechanical testing of DMLS parts," *EOS whitepaper*, EOS GmbH, Munich, 2009.
- [17] *Laser Melting - Additively*. [Online]. Available: <https://www.additively.com/en/learn-about/laser-melting##> (accessed: Jan. 10 2019).
- [18] I. van Zyl, "Residual stress of Ti6Al4V (ELI) parts manufactured by direct metal laser sintering," Bloemfontein: Central University of Technology, Free State, 2016. [Online]. Available: <http://ir.cut.ac.za/bitstream/11462/1417/1/Van%20Zyl%2c%20lan.pdf>
- [19] F. Klocke, C. Wagner, and C. Ader, Eds., *Development of an integrated model for selective laser sintering*, 2003.
- [20] *How Fibre Lasers Work | Optoelectronics Research Centre | University of Southampton*. [Online]. Available: <https://www.orc.soton.ac.uk/how-fibre-lasers-work##> (accessed: Mar. 1 2019).
- [21] M. Lackner, *Lasers in chemistry*. Wiley-VCH Weinheim, Germany, 2008.
- [22] I. A. Roberts, "Investigation of residual stresses in the laser melting of metal powders in additive layer manufacturing," 2012.
- [23] D. R. Lide, *Handbook of chemistry and physics 2001-2002*: CRC Press.
- [24] M. S. Brown and C. B. Arnold, "Fundamentals of laser-material interaction and application to multiscale surface modification," in *Laser precision microfabrication*: Springer, 2010, pp. 91–120.
- [25] I. van Zyl, I. Yadroitsava, and I. Yadroitsev, "Residual stress in Ti6Al4V objects produced by direct metal laser sintering," *South African Journal of Industrial Engineering*, vol. 27, no. 4, pp. 134–141, 2016.
- [26] I. Yadroitsev, A. Gusarov, I. Yadroitsava, and I. Smurov, "Single track formation in selective laser melting of metal powders," *Journal of Materials Processing Technology*, vol. 210, no. 12, pp. 1624–1631, 2010.
- [27] I. Yadroitsev and I. Smurov, "Surface morphology in selective laser melting of metal powders," *Physics Procedia*, vol. 12, pp. 264–270, 2011.

- [28] L. Thijs, F. Verhaeghe, T. Craeghs, J. van Humbeeck, and J.-P. Kruth, "A study of the microstructural evolution during selective laser melting of Ti-6Al-4V," *Acta Materialia*, vol. 58, no. 9, pp. 3303–3312, 2010.
- [29] P. Hanzl, M. Zetek, T. Bakša, and T. Kroupa, "The influence of processing parameters on the mechanical properties of SLM parts," *Procedia Engineering*, vol. 100, pp. 1405–1413, 2015.
- [30] K. Guan, Z. Wang, M. Gao, X. Li, and X. Zeng, "Effects of processing parameters on tensile properties of selective laser melted 304 stainless steel," *Materials & Design*, vol. 50, pp. 581–586, 2013.
- [31] W. F. Smith and J. Hashemi, *Foundations of materials science and engineering*: McGraw-Hill, 2011.
- [32] M. Peters, G. Ziegler, and G. Lütjering, "Control of microstructures of(α + β)-titanium alloys," *Zeitschrift für Metallkunde*, vol. 74, pp. 274–282, 1983.
- [33] J. Albrecht and G. Lütjering, "Microstructure and mechanical properties of titanium alloys," *Titanium'99: Science and Technology*, pp. 363–374, 2000.
- [34] D. R. Askeland and W. J. Wright, *Science and Engineering of Materials, SI Edition*: Cengage Learning, 2015. [Online]. Available: <https://books.google.co.za/books?id=vTFBBAAAQBAJ>
- [35] G. Lütjering, J. Albrecht, and O. M. Ivasishin, "Influence of cooling rate and beta grain size on the tensile properties of(α + β) Ti-alloys," *Titanium'95*, vol. 2, pp. 1163–1170, 1995.
- [36] R. Pederson, *Microstructure and Phase transformation of Ti-6Al-4V*: Luleå tekniska universitet, 2002.
- [37] Le Murr *et al.*, "Microstructure and mechanical behavior of Ti-6Al-4V produced by rapid-layer manufacturing, for biomedical applications," *Journal of the mechanical behavior of biomedical materials*, vol. 2, no. 1, pp. 20–32, 2009.
- [38] R. R. Boyer and Wallem, "The effect of cooling rate on the properties of beta-annealed Ti-6 Al-4 V," 1994.
- [39] J. C. Chesnutt, C. G. Rhodes, and J. C. Williams, "Relationship between mechanical properties, microstructure, and fracture topography in α + β titanium alloys," in *Fractography—Microscopic Cracking Processes*: ASTM International, 1976.
- [40] G. Lütjering, "Influence of processing on microstructure and mechanical properties of (α + β) titanium alloys," *Materials Science and Engineering: A*, vol. 243, 1-2, pp. 32–45, 1998, doi: 10.1016/S0921-5093(97)00778-8.
- [41] N. Clinning, *Thermomechanical processing of blended elemental powder Ti-6Al-4V alloy*: University of Cape Town, 2012.

- [42] S. K. Kar, *Modeling of mechanical properties in alpha/beta-titanium alloys*: The Ohio State University, 2005.
- [43] J. Williams, R. Boyer, and M. Blackburn, "The Influence of Microstructure on the Fracture Topography of Titanium Alloys," in *Electron Microfractography*: ASTM International, 1969.
- [44] M. Peters, J. Hemptenmacher, J. Kumpfert, and C. Leyens, "Structure and properties of titanium and titanium alloys," *Titanium and titanium alloys: fundamentals and applications*, pp. 1–36, 2003.
- [45] A. Ambard, L. Guétaz, F. Louchet, and D. Guichard, "Role of interphases in the deformation mechanisms of an α/β titanium alloy at 20 K," *Materials Science and Engineering: A*, vol. 319, pp. 404–408, 2001.
- [46] E. Lee, *Microstructure evolution and microstructure/mechanical properties relationships in $\alpha + \beta$ titanium alloys*: The Ohio State University, 2004.
- [47] J. A. Hines and G. Lütjering, "Propagation of microcracks at stress amplitudes below the conventional fatigue limit in Ti–6Al–4V," *Fatigue & Fracture of Engineering Materials & Structures*, vol. 22, no. 8, pp. 657–665, 1999.
- [48] M. Shunmugavel, A. Polishetty, and G. Littlefair, "Microstructure and Mechanical Properties of Wrought and Additive Manufactured Ti-6Al-4 V Cylindrical Bars," *Procedia Technology*, vol. 20, pp. 231–236, 2015.
- [49] C. R. Knowles, T. H. Becker, and R. B. Tait, Eds., *The effect of heat treatment on the residual stress levels within direct metal laser sintered Ti-6Al-4V as measured using the hole-drilling strain gauge method*, 2012.
- [50] B. Vrancken, L. Thijs, J.-P. Kruth, and J. van Humbeeck, "Heat treatment of Ti6Al4V produced by Selective Laser Melting: Microstructure and mechanical properties," *Journal of Alloys and Compounds*, vol. 541, pp. 177–185, 2012, doi: 10.1016/j.jallcom.2012.07.022.
- [51] L. Facchini, E. Magalini, P. Robotti, A. Molinari, S. Höges, and K. Wissenbach, "Ductility of a Ti - 6Al - 4V alloy produced by selective laser melting of prealloyed powders," *Rapid Prototyping Journal*, vol. 16, no. 6, pp. 450–459, 2010, doi: 10.1108/13552541011083371.
- [52] K. Kubiak and J. Sieniawski, "Development of the microstructure and fatigue strength of two phase titanium alloys in the processes of forging and heat treatment," *Journal of Materials Processing Technology*, vol. 78, 1-3, pp. 117–121, 1998.
- [53] M. T. Jovanović, S. Tadić, S. Zec, Z. Mišković, and I. Bobić, "The effect of annealing temperatures and cooling rates on microstructure and mechanical properties of investment cast Ti–6Al–4V alloy," *Materials & Design*, vol. 27, no. 3, pp. 192–199, 2006, doi: 10.1016/j.matdes.2004.10.017.
- [54] T. H. Becker, M. Beck, and C. Scheffer, "MICROSTRUCTURE AND MECHANICAL PROPERTIES OF DIRECT METAL LASER SINTERED TI-6AL-4V," *The South African*

- Journal of Industrial Engineering*, vol. 26, no. 1, pp. 1–10, 2015. [Online]. Available: <http://sajie.journals.ac.za/pub/article/download/1022/579>
- [55] M. Simonelli, *Microstructure evolution and mechanical properties of selective laser melted Ti-6Al-4V*: © Marco Simonelli, 2014.
- [56] X. Y. Cheng *et al.*, “Compression deformation behavior of Ti–6Al–4V alloy with cellular structures fabricated by electron beam melting,” *Journal of the mechanical behavior of biomedical materials*, vol. 16, pp. 153–162, 2012.
- [57] M. J. Donachie, “Titanium,” *A Technical Guide, ASM International, Materials Park, OH*, 2000.
- [58] M. K. E. Ramosoou, “Characterisation and static behaviour of the DMLS Ti-6Al-4V for Bio-medical applications,” Bloemfontein: Central University of Technology, Free State, 2015. [Online]. Available: <http://ir.cut.ac.za/bitstream/11462/275/1/Ramosoou%2c%20Makhabo%20Khabiso%20Ellen.pdf>
- [59] A. Mertens *et al.*, “Mechanical properties of alloy Ti–6Al–4V and of stainless steel 316L processed by selective laser melting: Influence of out-of-equilibrium microstructures,” *Powder Metallurgy*, vol. 57, no. 3, pp. 184–189, 2014, doi: 10.1179/1743290114Y.0000000092.
- [60] M. G. Moletsane, P. Krakhmalev, N. Kazantseva, A. Du Plessis, I. Yadroitsava, and I. Yadroitsev, “Tensile properties and microstructure of direct metal laser-sintered Ti6Al4V (ELI) Alloy,” *South African Journal of Industrial Engineering*, vol. 27, no. 3, pp. 110–121, 2016.
- [61] A. A. Antonysamy, J. Meyer, and P. B. Prangnell, “Effect of build geometry on the β -grain structure and texture in additive manufacture of Ti6Al4V by selective electron beam melting,” *Materials Characterization*, vol. 84, pp. 153–168, 2013, doi: 10.1016/j.matchar.2013.07.012.
- [62] J. S. Keist and T. A. Palmer, “Role of geometry on properties of additively manufactured Ti-6Al-4V structures fabricated using laser based directed energy deposition,” *Materials & Design*, vol. 106, pp. 482–494, 2016, doi: 10.1016/j.matdes.2016.05.045.
- [63] F. H. Kim and S. P. Moylan, “Literature Review of Metal Additive Manufacturing Defects,” 2018.
- [64] H. K. Rafi, N. V. Karthik, H. Gong, T. L. Starr, and B. E. Stucker, “Microstructures and mechanical properties of Ti6Al4V parts fabricated by selective laser melting and electron beam melting,” *J. of Materi Eng and Perform*, vol. 22, no. 12, pp. 3872–3883, 2013.
- [65] S. Leuders *et al.*, “On the mechanical behaviour of titanium alloy TiAl6V4 manufactured by selective laser melting: Fatigue resistance and crack growth performance,” *International Journal of Fatigue*, vol. 48, pp. 300–307, 2013.

- [66] A. Leicht and E. O. Wennberg, *Analyzing the Mechanical Behavior of Additive Manufactured Ti-6Al-4V Using Digital Image Correlation*: Citeseer, 2015.
- [67] I. van Zyl, M. Moletsane, P. Krakhmalev, I. Yadroitsava, and I. Yadroitsev, "Validation of miniaturised tensile testing on DMLS Ti6Al4V (ELI) specimens," *South African Journal of Industrial Engineering*, vol. 27, no. 3, pp. 192–200, 2016.
- [68] M. Simonelli, Y. Y. Tse, and C. Tuck, "Effect of the build orientation on the mechanical properties and fracture modes of SLM Ti–6Al–4V," *Materials Science and Engineering: A*, vol. 616, pp. 1–11, 2014, doi: 10.1016/j.msea.2014.07.086.
- [69] D. Banerjee and J. C. Williams, "Perspectives on Titanium Science and Technology," *Acta Materialia*, vol. 61, no. 3, pp. 844–879, 2013, doi: 10.1016/j.actamat.2012.10.043.
- [70] A. Paranjpe, *Residual stresses in machined titanium (Ti-6Al-4V) alloys*: The University of Utah, 2014.
- [71] P. Krakhmalev, I. Yadroitsava, G. Fredriksson, and I. Yadroitsev, "In situ heat treatment in selective laser melted martensitic AISI 420 stainless steels," *Materials & Design*, vol. 87, pp. 380–385, 2015.
- [72] G. K.L. Ng, A. E.W. Jarfors, G. Bi, and H. Y. Zheng, "Porosity formation and gas bubble retention in laser metal deposition," *Applied Physics A*, vol. 97, no. 3, p. 641, 2009.
- [73] *Mechanical properties of additive manufactured Ti-6Al-4V using wire and powder based processes*: IOP Publishing, 2011.
- [74] L. Chauke, K. Mutombo, and C. Kgomo, *Characterization of the direct metal laser sintered Ti6Al4V Components*. [Online]. Available: https://researchspace.csir.co.za/dspace/bitstream/10204/7244/1/Chauke_2013.pdf
- [75] L. E. Murr *et al.*, "Microstructure and mechanical behavior of Ti-6Al-4V produced by rapid-layer manufacturing, for biomedical applications," *Journal of the mechanical behavior of biomedical materials*, vol. 2, no. 1, pp. 20–32, 2009, doi: 10.1016/j.jmbbm.2008.05.004.
- [76] T. Vilaro, C. Colin, and J. D. Bartout, "As-Fabricated and Heat-Treated Microstructures of the Ti-6Al-4V Alloy Processed by Selective Laser Melting," *Metall and Mat Trans A*, vol. 42, no. 10, pp. 3190–3199, 2011, doi: 10.1007/s11661-011-0731-y.
- [77] W. K. de Vree, "On the influence of build orientation on the mechanical properties of direct metal laser sintered (DMLS) Ti-6Al-4V flexures," 2016.
- [78] J. Alcisto *et al.*, "Tensile Properties and Microstructures of Laser-Formed Ti-6Al-4V," *J. of Materi Eng and Perform*, vol. 20, no. 2, pp. 203–212, 2011, doi: 10.1007/s11665-010-9670-9.
- [79] *Test Methods for Tension Testing of Metallic Materials*, 2016.
- [80] M. E. Mortenson, *Mathematics for computer graphics applications*: Industrial Press Inc, 1999.

- [81] C. C. Seepersad, *A robust topological preliminary design exploration method with materials design applications*: Georgia Institute of Technology, 2004.
- [82] P. W. Christensen and A. Klarbring, *An introduction to structural optimization*: Springer Science & Business Media, 2008.
- [83] M. P. Bendsøe and N. Kikuchi, "Generating optimal topologies in structural design using a homogenization method," *Computer Methods in Applied Mechanics and Engineering*, vol. 71, no. 2, pp. 197–224, 1988.
- [84] G. I. N. Rozvany, M. Zhou, and T. Birker, "Generalized shape optimization without homogenization," *Structural optimization*, vol. 4, 3-4, pp. 250–252, 1992.
- [85] H. Zhang and X. H. Ren, Eds., *Topology Optimization of Continuum Structures Based on SIMP*: Trans Tech Publ, 2011.
- [86] O. M. Querin, G. P. Steven, and Y. M. Xie, "Evolutionary structural optimisation (ESO) using a bidirectional algorithm," *Engineering computations*, vol. 15, no. 8, pp. 1031–1048, 1998.
- [87] K. Tai and S. Akhtar, "Structural topology optimization using a genetic algorithm with a morphological geometric representation scheme," *Struct Multidisc Optim*, vol. 30, no. 2, pp. 113–127, 2005.
- [88] M. P. Bendsøe and N. Kikuchi, "Generating optimal topologies in structural design using a homogenization method," *Computer Methods in Applied Mechanics and Engineering*, vol. 71, no. 2, pp. 197–224, 1988, doi: 10.1016/0045-7825(88)90086-2.
- [89] M. P. Bendsøe, "Optimal shape design as a material distribution problem," *Structural optimization*, vol. 1, no. 4, pp. 193–202, 1989, doi: 10.1007/BF01650949.
- [90] G. I. N. Rozvany, M. Zhou, and T. Birker, "Generalized shape optimization without homogenization," *Structural optimization*, vol. 4, 3-4, pp. 250–252, 1992, doi: 10.1007/BF01742754.
- [91] G.I.N. Rozvany, "Aims, scope, methods, history and unified terminology of computer-aided topology optimization in structural mechanics," *Struct Multidisc Optim*, vol. 21, no. 2, pp. 90–108, 2001, doi: 10.1007/s001580050174.
- [92] A. Aremu, I. Ashcroft, R. Hague, R. Wildman, and C. Tuck, "Suitability of SIMP and BESO topology optimization algorithms for additive manufacture," in *Twenty First Annual International Solid Freeform Fabrication Symposium, Austin*, 2010, pp. 679–692.
- [93] S. Anantharaman, "Topology Optimization For Thin Walled Structures Utilizing Simp Method By Additive Manufacturing Using Optimized Conditions," 2015.
- [94] M. Papadrakakis, V. Papadopoulos, G. Stefanou, and V. Plevris, "TOPOLOGY OPTIMIZATION FOR ADDITIVE MANUFACTURING WITH CONTROLLABLE SUPPORT STRUCTURE COSTS,"

- [95] Y. Saadlaoui, J.-L. Milan, J.-M. Rossi, and P. Chabrand, "Topology optimization and additive manufacturing: Comparison of conception methods using industrial codes," *Journal of Manufacturing Systems*, 43, Part 1, pp. 178–186, 2017, doi: 10.1016/j.jmsy.2017.03.006.
- [96] N. P. Fey, B. J. South, C. C. Seepersad, and R. R. Neptune, "Topology Optimization and Freeform Fabrication Framework for Developing Prosthetic Feet," in *Solid Freeform Fabrication Symposium*, 2009, pp. 607–619.
- [97] V. G. Sundararajan, "Topology optimization for additive manufacturing of customized meso-structures using homogenization and parametric smoothing functions," 2010.
- [98] M. Langelaar, "Topology optimization of 3D self-supporting structures for additive manufacturing," *Additive Manufacturing*, 12, Part A, pp. 60–70, 2016, doi: 10.1016/j.addma.2016.06.010.
- [99] *Topology Optimization (Introduction) Part 1 - YouTube*. [Online]. Available: https://www.youtube.com/watch?v=_erS8dRxILM## (accessed: Apr. 2 2019).
- [100] O. Sigmund, "A 99 line topology optimization code written in Matlab," *Struct Multidisc Optim*, vol. 21, no. 2, pp. 120–127, 2001, doi: 10.1007/s001580050176.
- [101] K. Liu and A. Tovar, "An efficient 3D topology optimization code written in Matlab," *Struct Multidisc Optim*, vol. 50, no. 6, pp. 1175–1196, 2014, doi: 10.1007/s00158-014-1107-x.
- [102] E. Andreassen, A. Clausen, M. Schevenels, B. S. Lazarov, and O. Sigmund, "Efficient topology optimization in MATLAB using 88 lines of code," *Struct Multidisc Optim*, vol. 43, no. 1, pp. 1–16, 2011, doi: 10.1007/s00158-010-0594-7.
- [103] A. Aremu, I. Ashcroft, R. Wildman, R. Hague, C. Tuck, and D. Brackett, "The effects of bidirectional evolutionary structural optimization parameters on an industrial designed component for additive manufacture," *Proceedings of the Institution of Mechanical Engineers, Part B: Journal of Engineering Manufacture*, vol. 227, no. 6, pp. 794–807, 2013, doi: 10.1177/0954405412463857.
- [104] Y. Chen, J. Lu, and Y. Wei, "Topology optimization for manufacturability based on the visibility map," *Computer-Aided Design and Applications*, vol. 13, no. 1, pp. 86–94, 2015, doi: 10.1080/16864360.2015.1059199.
- [105] Jiadong Deng, "Topology Optimization of Emerging Complex Structures," DOCTOR OF PHILOSOPHY Field of Mechanical Engineering, NORTHWESTERN UNIVERSITY, EVANSTON, ILLINOIS, 2016.
- [106] M. Langelaar, "An additive manufacturing filter for topology optimization of print-ready designs," *Struct Multidisc Optim*, vol. 55, no. 3, pp. 871–883, 2017, doi: 10.1007/s00158-016-1522-2.

- [107] J. Lu and Y. Chen, "Topology Optimization of a Prosthetic Knee Joint Component," in *2010 International Conference on Manufacturing Automation*, Hong Kong, China, 2010, pp. 94–98.
- [108] M. Okruta, "Three-dimensional topology optimization of statically loaded porous and multi-phase structures," 2014.
- [109] "Altair OptiStruct User Guide,"
- [110] *Siemens Documentation: Simcenter Pre/Post*. [Online]. Available: https://docs.plm.automation.siemens.com/tdoc/nx/12/nx_help### (accessed: May 17 2019).
- [111] *Topology optimization for additive manufacturing*: S, 2011.
- [112] S. Liu, Q. Li, J. Liu, W. Chen, and Y. Zhang, "A Realization Method for Transforming a Topology Optimization Design into Additive Manufacturing Structures," *Engineering*, vol. 4, no. 2, pp. 277–285, 2018, doi: 10.1016/j.eng.2017.09.002.
- [113] M. P. Bendsøe and O. Sigmund, "Topology optimization by distribution of isotropic material," in *Topology Optimization: Theory, Methods, and Applications*, M. P. Bendsøe and O. Sigmund, Eds., Berlin, Heidelberg: Springer Berlin Heidelberg, 2004, pp. 1–69. [Online]. Available: https://doi.org/10.1007/978-3-662-05086-6_1
- [114] A. Clausen, N. Aage, and O. Sigmund, "Topology optimization with flexible void area," *Struct Multidisc Optim*, vol. 50, no. 6, pp. 927–943, 2014, doi: 10.1007/s00158-014-1109-8.
- [115] *Topology Optimization and Casting Feasibility of a Robot Arm*. [Online]. Available: <https://www.altair.com/resource/topology-optimization-and-casting-feasibility-of-a-robot-arm###> (accessed: Feb. 19 2020).
- [116] *Design Optimization for Additive Manufacturing in OptiStruct with consideration of Overhang Angle in Topology Optimization*. [Online]. Available: <https://www.altair.com/resource/design-optimization-for-additive-manufacturing-in-optistruct-with-consideration-of-overhang-angle-in-topology-optimization###> (accessed: Feb. 19 2020).
- [117] *Application of Optimisation Tools to the Design of Advanced Carbon Fibre Bicycle: FACTOR 001 - Altair University*. [Online]. Available: <https://altairuniversity.com/2903-application-of-optimisation-tools-to-the-design-of-advanced-carbon-fibre-bicycle-factor-001/###> (accessed: Feb. 19 2020).
- [118] *Resources*. [Online]. Available: <https://www.altair.com/resources/customer-videos###> (accessed: May 17 2019).
- [119] D. Walton and H. Moztarzadeh, "Design and Development of an Additive Manufactured Component by Topology Optimisation," *Procedia CIRP*, vol. 60, pp. 205–210, 2017, doi: 10.1016/j.procir.2017.03.027.
- [120] P. Zeleny and M. Cadek, "TOPOLOGY OPTIMIZATION OF A BICYCLE PART," *MM SJ*, vol. 2015, no. 03, pp. 696–700, 2015, doi: 10.17973/MMSJ.2015_10_201538.

- [121] Altair, *A Design-Validation-Production Workflow for Aerospace Additive Manufacturing*. [Online]. Available: https://web.altair.com/altair_matereality_whitepaper_2016-11## (accessed: Feb. 19 2020).
- [122] L. Podshivalov, C. M. Gomes, A. Zocca, J. Guenster, P. Bar-Yoseph, and A. Fischer, "Design, analysis and additive manufacturing of porous structures for biocompatible micro-scale scaffolds," *Procedia CIRP*, vol. 5, pp. 247–252, 2013.
- [123] G. P. Nikishkov, "Introduction to the finite element method," *University of Aizu*, pp. 1–70, 2004.
- [124] E. Madenci and I. Guven, *The finite element method and applications in engineering using ANSYS®*: Springer, 2015.
- [125] B. Schoinochoritis, D. Chantzis, and K. Salonitis, "Simulation of metallic powder bed additive manufacturing processes with the finite element method: A critical review," *Proceedings of the Institution of Mechanical Engineers, Part B: Journal of Engineering Manufacture*, vol. 231, no. 1, pp. 96–117, 2015, doi: 10.1177/0954405414567522.
- [126] T. C. Dzogbewu, L. Monaheng, I. Yadroitsava, W. B. Du Preez, and I. Yadroitsev, "Finite element analysis in design of DMLS mandible implants," in *Challenges for Technology Innovation: ROUTLEDGE in association with GSE Research*, 2017, pp. 155–160.
- [127] A. Lundbäck and L.-E. Lindgren, "Finite Element Simulation to Support Sustainable Production by Additive Manufacturing," *Procedia Manufacturing*, vol. 7, pp. 127–130, 2017, doi: 10.1016/j.promfg.2016.12.033.
- [128] "Numerical modeling and testing of mechanical behavior of AM Titanium alloy bracket for aerospace applications," *Procedia Structural Integrity*, vol. 5, pp. 753–760, 2017, doi: 10.1016/j.prostr.2017.07.166.
- [129] L. F. MONAHENG, "FINITE ELEMENT ANALYSIS OF A Ti6Al4V (ELI) MEDICAL IMPLANT PRODUCED THROUGH ADDITIVE MANUFACTURING," Bloemfontein: Central University of Technology, Free State, 2017. [Online]. Available: <http://ir.cut.ac.za/bitstream/11462/1333/1/Monaheng%2c%20Lehlohonolo%20Francis.pdf>
- [130] M. Abdi, I. Ashcroft, and R. D. Wildman, "Design optimization for an additively manufactured automotive component," *International Journal of Powertrains*, 2017.
- [131] M. G. MOLETSANE, "Microstructure and mechanical properties of Ti6Al4V (ELI) parts produced by DMLS," Bloemfontein: Central University of Technology, Free State, 2016. [Online]. Available: <http://ir.cut.ac.za/bitstream/11462/1359/1/Moletsane%2c%20Morakane%20Gloria.pdf>
- [132] D. R. Askeland, P. P. Fulay, and W. J. Wright, *The Science and Engineering of Materials, SI Edition*: Cengage Learning, 2011. [Online]. Available: <https://books.google.co.za/books?id=UfclAAAAQBAJ>

- [133] S. S. Rao, *The finite element method in engineering*. Amsterdam: Butterworth-Heinemann, 2017.
- [134] Website designed and developed by Zarr - <https://www.zarr.com>, *Hand Calcs Vs Simulation - SOLIDWORKS Online Tutorial*. [Online]. Available: <https://www.solidsolutions.co.uk/solidworks/tutorial-videos/hand-calcs-vs-simulation.aspx##> (accessed: Aug. 2 2019).
- [135] R. C. Hibbeler and K. S. V. Sekar, *Mechanics of materials*. Jurong, Singapore: Pearson Education South Asia Pte Ltd, 2014.
- [136] E. N. ISO, "6892-1. Metallic materials-Tensile testing-Part 1: Method of test at room temperature," *International Organization for Standardization*, 2009.
- [137] "dev_004324," [Online]. Available: https://www.mts.com/cs/groups/public/documents/library/dev_004324.pdf
- [138] *Test Method for Strain-Controlled Fatigue Testing*, 2004.

APPENDIX A

The following is a description of AM processes as displayed in Figure 3. The images and definitions have been extracted from The 3D Printing Handbook written by Ben Redwood, Filemon Schöffner and Brian Garret: “

- Material extrusion



Figure 106: Material extrusion

Material extrusion is an AM process in which continuous filament of thermoplastics or composite material is selectively dispensed through a nozzle or orifice to defined locations in order to create target structures.

- Vat polymerisation

This AM process uses an ultraviolet light to selectively cure a liquid photopolymer in a vat by light-activated polymerisation.

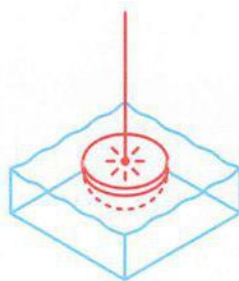


Figure 107: Vat polymerisation

- Powder bed fusion

Powder bed fusion is one of the seven AM techniques in which thermal energy selectively melts and fuses regions of material together on a bed of specific powder to form a 3D object.

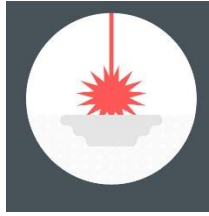


Figure 108: Powder bed fusion

- Material jetting

Material jetting is an AM process in which droplets of low-viscosity polymers like molten wax or thermoplastic material are selectively deposited and cured on a build plate.

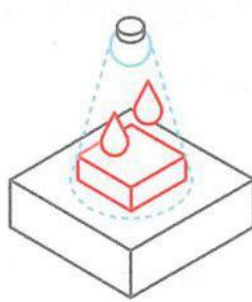


Figure 109: Material jetting

- Binder jetting

This AM process uses a liquid bonding agent to selectively bind layers of powder together to form a 3D part, either the final product or a green part which in turn is then cured at a later stage.



Figure 110: Binder jetting

- Direct energy deposition

Direct energy deposition is an AM technique which uses a focused thermal energy source to fuse material as it is being deposited to form a 3D object layer by layer [12].

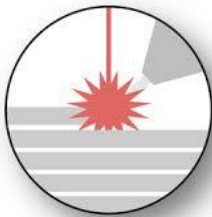


Figure 111: Direct energy deposition

- Sheet lamination

During sheet lamination, a 3D object is formed by stacking and laminating sheets of material.

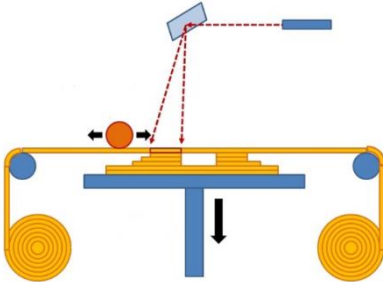


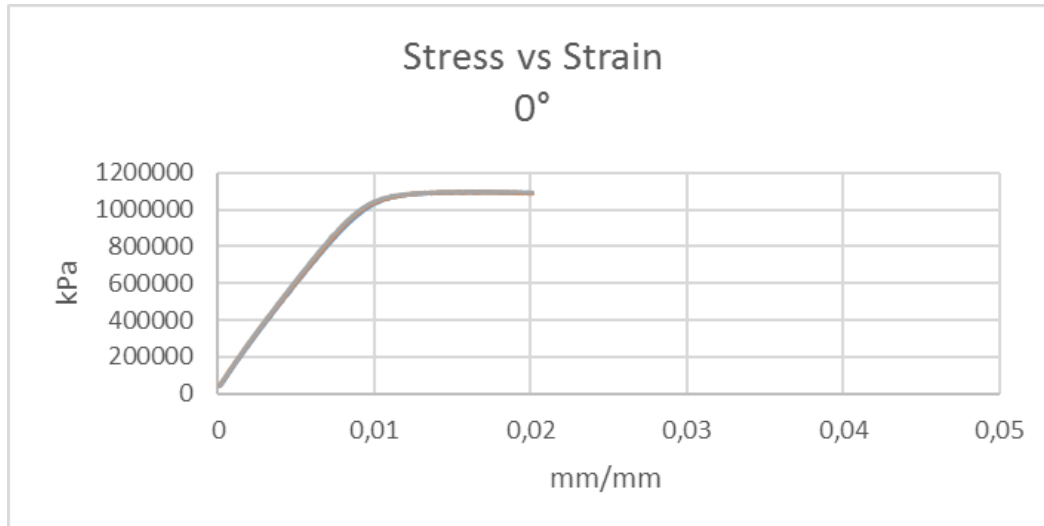
Figure 112: Sheet lamination

“

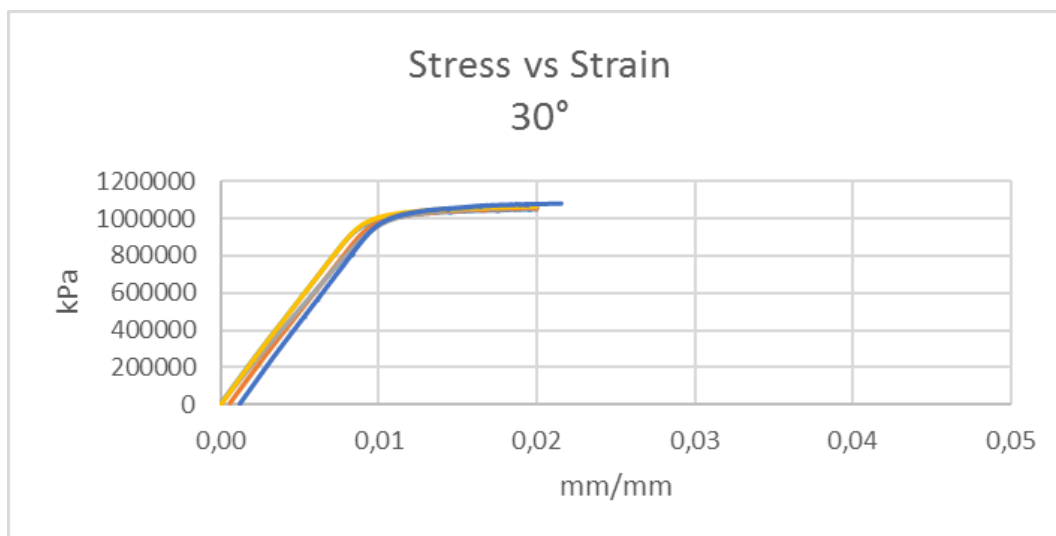
APPENDIX B

Appendix B presents the results of the tensile tests.

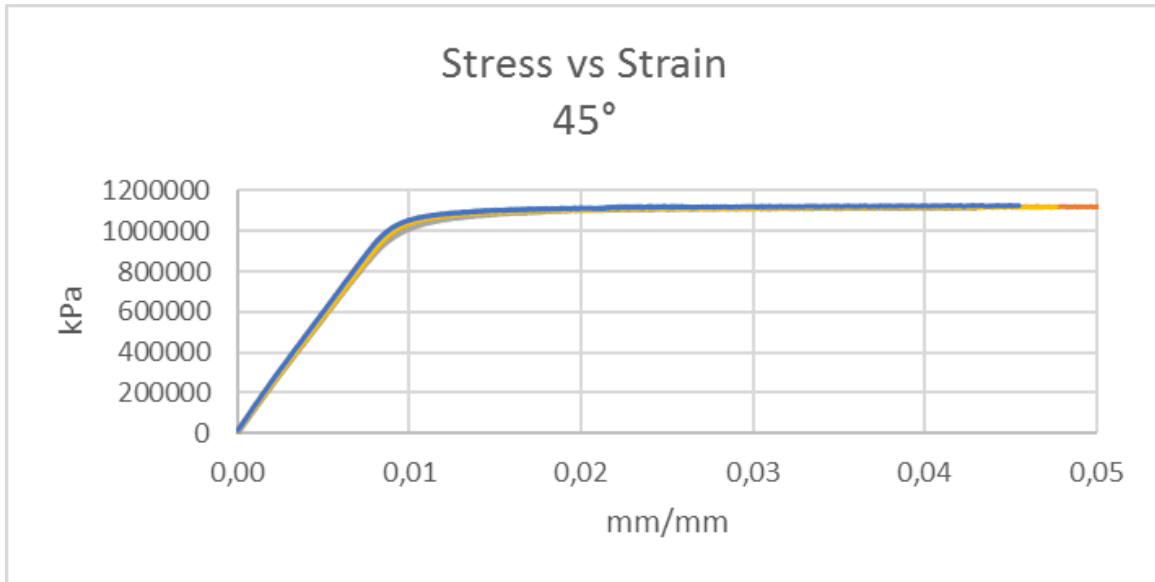
					Average	StDev	CV
0°	UTS	1092	1093	1098	1094,3	2,62	0,24
	E	105	108	110	107,7	2,05	1,91
	Offset Yield	1080	1078	1085	1081	2,94	0,27



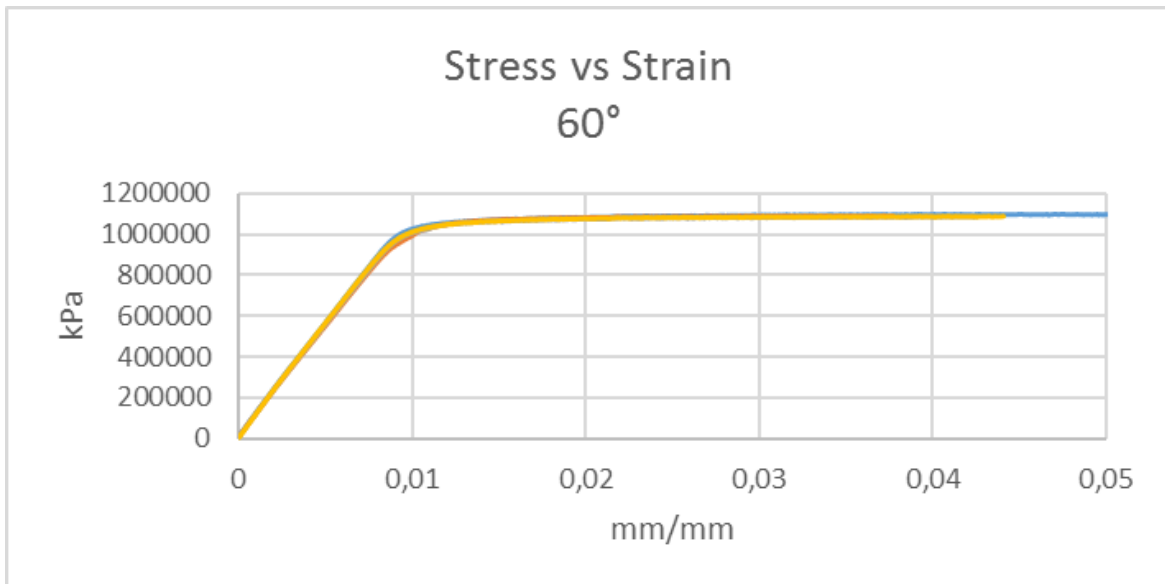
							AVG	StDev	CV
30°	UTS	1053	1059	1069	1067	1067	1063	6,07	0,57
	E	109	109	98,4	110	112	107,7	4,77	4,43
	Offset Yield	1017	1014	1031	1033	1019	1022,8	7,70	0,75



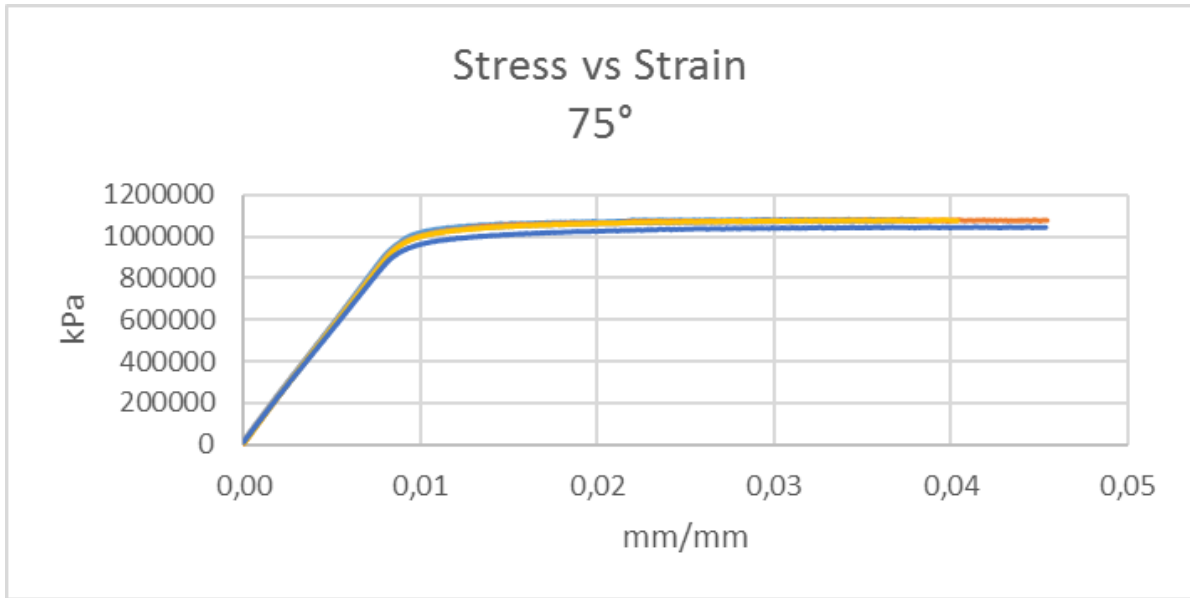
							AVG	StDev	CV
45°	UTS	1124	1122	1116	1121	1128	1122,2	3,92	0,35
	E	109	112	110	111	115	111,4	2,06	1,85
	Offset yield	1084	1069	1051	1072	1078	1070,8	11,16	1,04



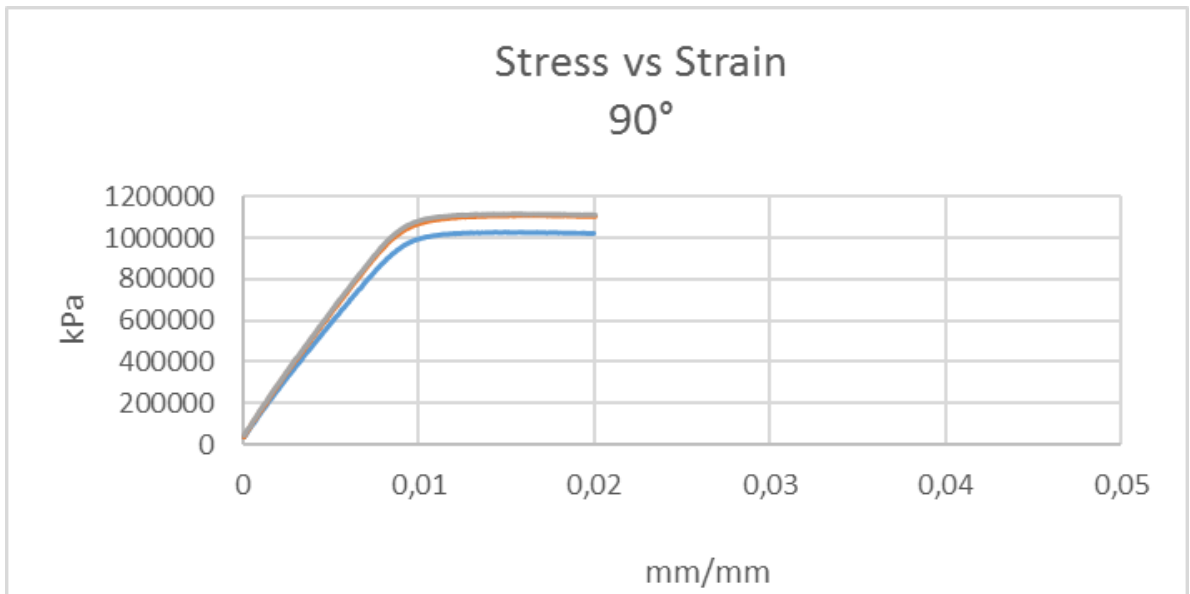
						AVG	StDev	CV
60	UTS	1100	1092	1090	1089	1092,75	4,32	0,40
	E	109	107	107	109	108,0	1	0,93
	Offset Yield	1055	1054	1048	1045	1050,5	4,15	0,40



							AVG	StDev	CV
75	UTS	1085	1080	1075	1081	1045	1073,2	14,46	1,35
	E	112	111	109	110	106	109,6	2,06	1,88
	Offset yield	1042	1030	1028	1023	1005	1025,6	12,04	1,17



					AVG	StDev	CV
90	UTS	1029	1111	1116	1085,3	39,89	3,675
	E	1057	1150	1148	1118,3	43,38	3,88
	Offset Yield	1020	1097	1105	1074	38,32	3,568



APPENDIX C

```
<RunInformation><BasicRunInfo><Client>Inspire 18.1 10130</Client><Name>Model Max Stiffness Mass 30%
(16)</Name><ModelName>Model</ModelName><stmodOffsetId>1</stmodOffsetId><RunType>2</RunType><GroupId>16</GroupId><Min
MemberSize>0.006007 m</MinMemberSize><VolumeFraction>3.000000E-001</VolumeFraction><StartTime>11/6/2018
13:18:46</StartTime><CompletionTime>11/6/2018 13:19:48</CompletionTime><ElapsedTime>00:01:02
</ElapsedTime><Status>9</Status><ErrorNumber>0</ErrorNumber><PercentComplete>100.000000</PercentComplete></BasicRunInfo><Ins
pireOccurrences><Occurrence><Name>Part
1</Name><OccId>42</OccId><DesignSpaceType>Required</DesignSpaceType><Mass>7.603451E-
003</Mass><FePropId>41</FePropId><FeId>41</FeId><FeBCs>yes</FeBCs><FeConnections>no</FeConnections></Occurrence><Occurenc
e><Name>Part 2</Name><OccId>44</OccId><DesignSpaceType>Required</DesignSpaceType><Mass>7.603451E-
003</Mass><FePropId>43</FePropId><FeId>43</FeId><FeBCs>yes</FeBCs><FeConnections>no</FeConnections></Occurrence><Occurenc
e><Name>Part 3</Name><OccId>46</OccId><DesignSpaceType>Design</DesignSpaceType><Mass>3.401555E-
001</Mass><FePropId>45</FePropId><FeId>45</FeId><FeBCs>no</FeBCs><FeConnections>no</FeConnections></Occurrence></InspireOc
currences><LoadCases><LoadCase><Name>Torsional
load</Name><Id>1</Id></LoadCase><LoadCase><Name>All</Name><Id>2</Id></LoadCase></LoadCases><Keywords><Kw><Name>DR
ESP1</Name><Attrib Value="" Name="ATTA_BLANK"/><Attrib Value="" Name="ATTB_BLANK"/><Attrib Value=""
Name="ATTi_BLANK"/><Attrib Value="1" Name="ID"/><Attrib Value="wcomp" Name="LABEL"/><Attrib Value=""
Name="PTYPE_BLANK"/><Attrib Value="0" Name="REGION"/><Attrib Value="WCOMP"
Name="RTYPE"/></Kw><Kw><Name>DRESP1</Name><Attrib Value="" Name="ATTA_BLANK"/><Attrib Value=""
Name="ATTB_BLANK"/><Attrib Value="2" Name="ID"/><Attrib Value="volfrac" Name="LABEL"/><Attrib Value=""
Name="PTYPE_PMB"/><Attrib Value="0" Name="REGION"/><Attrib Value="VOLFRAC"
Name="RTYPE"/></Kw><Kw><Name>PSOLID</Name><Attrib Value="0" Name="CORDM"/><Attrib Value="SMECH"
Name="FCTN"/><Attrib Value="BUBBLE" Name="IN"/><Attrib Value="REDUCED" Name="ISOP"/><Attrib Value="43"
Name="MID"/><Attrib Value="43.0" Name="PID"/><Attrib Value="NODE"
Name="STRESS"/></Kw><Kw><Name>PSOLID</Name><Attrib Value="0" Name="CORDM"/><Attrib Value="SMECH"
Name="FCTN"/><Attrib Value="BUBBLE" Name="IN"/><Attrib Value="REDUCED" Name="ISOP"/><Attrib Value="45"
Name="MID"/><Attrib Value="45.0" Name="PID"/><Attrib Value="NODE"
Name="STRESS"/></Kw><Kw><Name>PSOLID</Name><Attrib Value="0" Name="CORDM"/><Attrib Value="SMECH"
Name="FCTN"/><Attrib Value="BUBBLE" Name="IN"/><Attrib Value="REDUCED" Name="ISOP"/><Attrib Value="41"
Name="MID"/><Attrib Value="41.0" Name="PID"/><Attrib Value="NODE"
Name="STRESS"/></Kw></Keywords><LastIterationResponse>ITERATION 44 Subcase: 1 -----
----- Label x-force y-force z-force x-moment y-moment z-moment ----- Sum-App.
0.000E+00 0.000E+00 0.000E+00 0.000E+00 3.927E+01 0.000E+00 Sum-SPCF 1.192E-08 -1.014E-08 2.878E-08 8.085E-10 -3.927E+01 -
1.248E-09 ----- Subcase: 2 -----
Label x-force y-force z-force x-moment y-moment z-moment ----- Sum-App. 0.000E+00
-3.142E+04 2.454E+02 -1.717E+02 3.927E+01 -2.121E-03 Sum-SPCF 4.574E-09 3.142E+04 -2.454E+02 1.717E+02 -3.927E+01 2.121E-03 ----
----- the 2nd satisfied convergence ratio = 1.3115E-03 Objective Function (Minimize
WCOMP) = 7.23234E+00 % change = -0.13 Maximum Constraint Violation % = 0.25233E-06 Design Volume Fraction = 3.00000E-001 Mass =
1.16250E-001 Subcase Weight Compliance Epsilon Weight*Comp. 1 1.000E+00 7.773619E-01 -1.717008E-04 7.773619E-01 2 1.000E+00
6.454974E+00 -3.728567E-05 6.454974E+00 ----- Sum of Weight*Compliance 7.232336E+00 Note : Epsilon = Residual Strain Energy
Ratio. RETAINED RESPONSES TABLE ----- Response Type Response
Subcase Grid/ DOF/ Response Objective Viol. User-ID Label /RANDPS Element/ Comp Value Reference/ % /Model MID/PID/ /Reg Constraint
+Frqncy Mode No. Bound /Times ----- 1 WCOMP wcomp -- -- 7.232E+00
MIN 2 VOLFR volfrac -- -- TOTL 3.000E-01 < 3.000E-01 0.0 A -----
***** OPTIMIZATION HAS CONVERGED. FEASIBLE
DESIGN (ALL CONSTRAINTS SATISFIED). </LastIterationResponse></RunInformation>
```

APPENDIX D

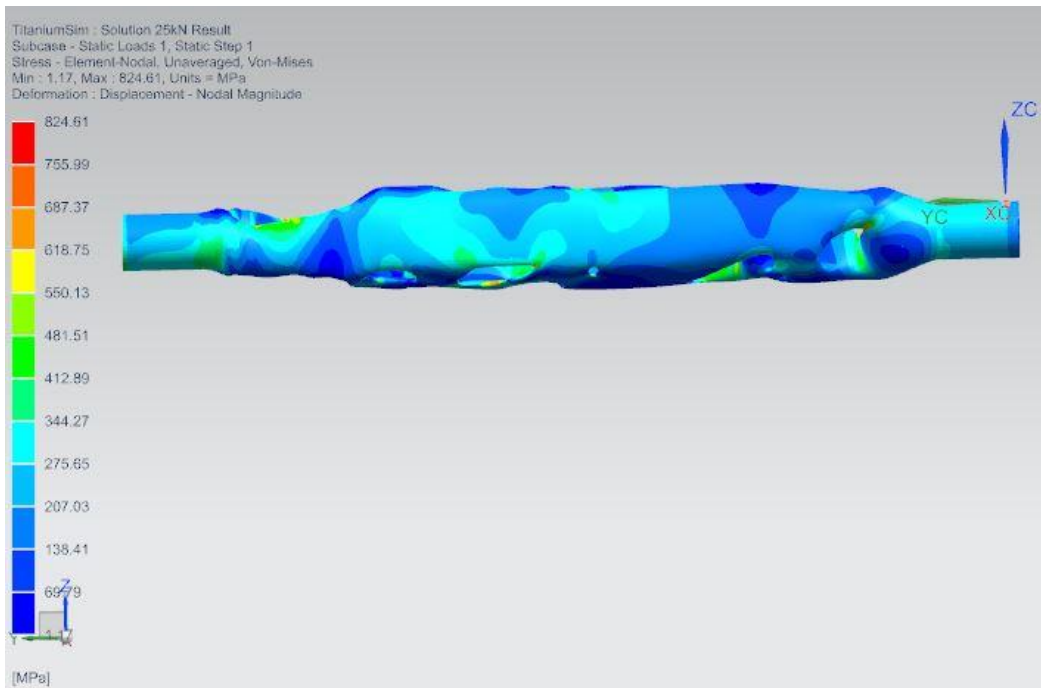


Figure 113:FEA 2: 25 kN

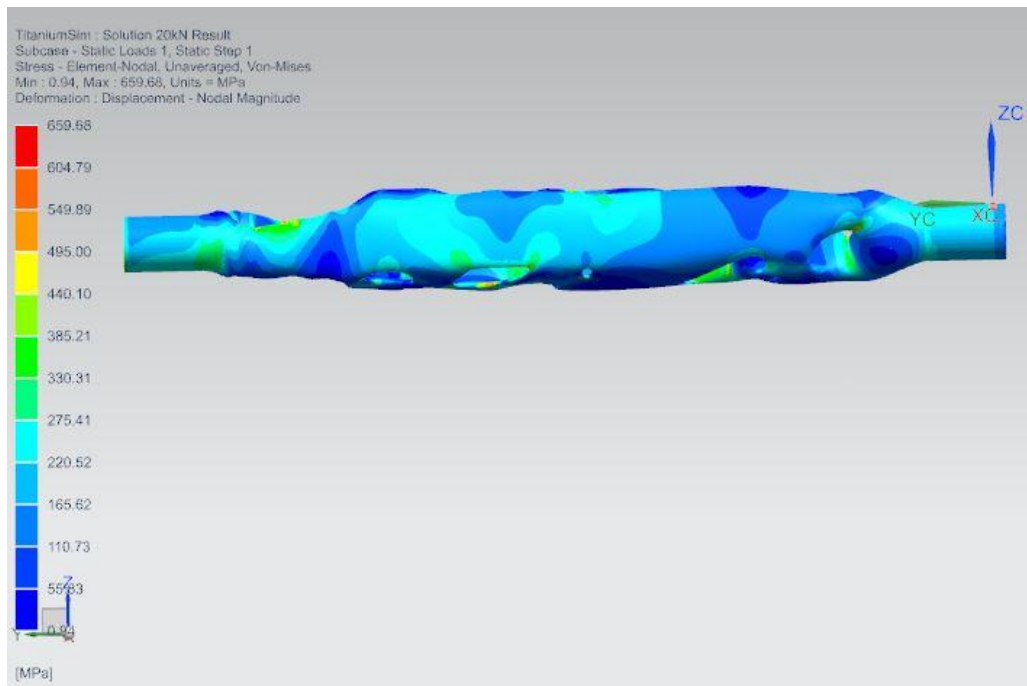


Figure 114:FEA 1: 20 kN

APPENDIX E

Table 16: Comparison of the resultant von Mises stresses for position 1 as obtained from the two practical test

Position 1			
Load (kN)	Practical test 1 (MPa)	Practical test 2 (MPa)	Correlation (%)
20	134,4	145	92,7
25	187	193,4	96,7
29,36	225,3	223,8	99,3

Table 17: Comparison of the resultant von Mises stresses for position 2 as obtained from the two practical test

Position 2			
Load (kN)	Practical test 1 (MPa)	Practical test 2 (MPa)	Correlation (%)
20	245,7	239,8	97,5
25	300,7	291,2	96,7
29,36	367,7	389,1	94,5

Table 18: Comparison of von Mises stress as obtained from FEA and practical test 1 at position 1

Position 1			
Load (kN)	Practical test 1 (MPa)	FEA (MPa)	Correlation (%)
20	144,7	165,62	87,4
25	184,9	207,03	89,3
29,36	221	244,08	90,5

Table 19: Comparison of von Mises stress as obtained from FEA and practical test 1 at position 2

Position 2			
Load (kN)	Practical test 1 (MPa)	FEA (MPa)	Correlation (%)
20	245,7	275,41	89,2
25	300,7	344,27	87,3
29,36	367,7	405,89	90,6

Table 20: Comparison of von Mises stress as obtained from FEA and practical test 2 at position 1

Position 1			
Load (kN)	Practical test 2 (MPa)	FEA (MPa)	Correlation (%)
20	145	165,62	87,5
25	193,4	207,03	93,4
29,36	223,8	244,08	91,7

Table 21: Comparison of von Mises stress as obtained from FEA and practical test 2 at position 2

Position 2			
Load (kN)	Practical test 2 (MPa)	FEA (MPa)	Correlation (%)
20	239,8	275,41	87,1
25	291,2	344,27	84,6
29,36	389,1	405,89	95,9

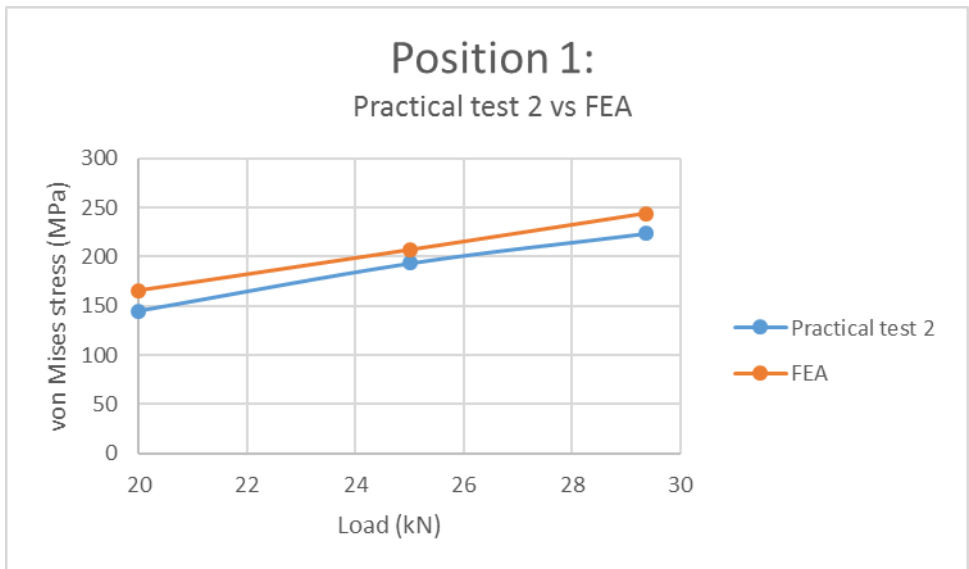


Figure 115: Comparison of von Mises stress as obtained from FEA and practical test 2 at position 1

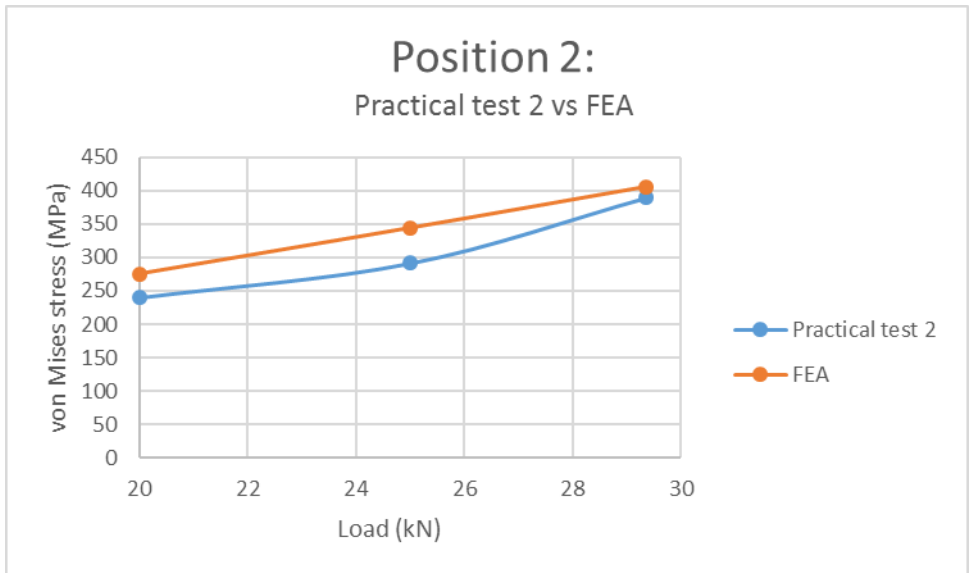


Figure 116: Comparison of von Mises stress as obtained from FEA and practical test 2 at position 2